This is to certify that the
dissertation entitled

LOCAL TOOL WEAR PROFILES PREDICTION USING
PHYSICS-BASED MODELS

presented by

Jorge A. Olortegui-Yume

has been accepted towards fulfillment
of the requirements for the

Ph.D. degree in Mechanical Engineering

Major Professor's Signature

May 8, 2009.

Date

LOCAL TOOL WEAR PROFILES PREDICTION USING PHYSICS-BASED MODELS

By

Jorge A. Olortegui-Yume

A DISSERTATION

Submitted to
Michigan State University
in partial fulfillment of the requirements
for the degree of

DOCTOR OF PHILOSOPHY

Mechanical Engineering

2009

ABSTRACT

LOCAL TOOL WEAR PROFILES PREDICTION USING PHYSICS-BASED MODELS

By

Jorge A. Olortegui-Yume

A semi-empirical model based on the physics of the wear mechanisms is developed to predict crater profiles of multilayer coated tools after turning. The averaged dissolution and abrasion relationships are recast into local versions to predict directly based on the temperature and pressure profiles from Finite Element (FE) simulations. The approach is reasonable to explain the crater profiles observed in multilayer coated carbides. However, the model deviates from the real profiles due to the κ-to-α-Al_2O_3 phase transformation in the middle layer, the change in interfacial conditions with the exposure of subsequent layers, the combined wear resistance of multi-layers of the cutting tool, and the deformation of the cutting tool.

In addition to the modeling effort, AISI 1045 steel bars were dry-turned with multilayer coated carbide tools. The worn cutting tool tips were analyzed by means of Secondary Electrons (SE) imaging, Back-scattered Electrons(BSE) imaging, Energy Dispersive x-ray Spectroscopy (EDS), X-ray Diffractometry (XRD), Profilometry, and Confocal Laser Scanning Microscopy (CSLM). The existence of two layers made of different Al_2O_3 polymorphs (κ and α) in the fresh inserts was demonstrated with XRD analysis and SE imaging. SP and CSLM

were extensively used to characterize the surface topography of the worn rake faces. In doing so, the tool tip deformation was observed taking place and influencing the crater patterns measurements. On the other hand, the work material microstructure showed a clear influence in the amount of wear obtained. Two nominally equal AISI1045 steels with normalized and grain-refined microstructures gave very different wear losses under the same machining conditions.

The multi-resolution wavelet analysis was successfully tailored to post-process the surface data. Very clear wear trends, not available with traditional Fourier-based filters, were identified. The latter aided in the determination of wear coefficients and in the unambiguous detection of the maximum crater depth location. Additionally, the feasibility of roughness separation from waviness and form in the crater zone was proven, which opens a promising path for future micro-mechanisms analysis.

DEDICATION

To the ONE whose fear brings knowledge

ACKNOWLEDGEMENTS

Dr. Patrick Kwon's patience, guidance and support magnified by his upbeat personality are more than enough to grant him my sincere gratitude.

My appreciation to Dr. Thomas Schuelke, Mr. Michael Becker, and Mr. Sebastian Wicklein at Franhoufer CCL USA for the financial support and the availability of their equipment and their kindness during the hardest moments of this investigation.

My thanks to Dr. Stanley Flegler and all his staff at the MSU Center for Advanced Microscopy: where kindheartedness and professionalism live in harmony. Thanks also to Dr. Feeny and and Dr. Liu for their availability.

A special acknowledgement is due to Dr. Thomas Bieler at the MSU Materials Science Department for his suggestions and time.

Mere thanks would not be sufficient for my wife as she did "half the PhD", while staying at home with my three blessings: Josue, Daniel, and Abigail. I am deeply thankful also to my mother Rosina, my brother, Pablo, and aunt Martha whose examples have shaped my character making up for great part of my life accomplishments. Most of all, thanks to Jesus Christ, my Lord, for fulfilling His promises in my life in spite of my shortcomings.

My appreciation to my co-workers Kyunghee Park and Li Sun for enriching my professional scope with their practicality and well-done job. A special mention to Dr. Moon-Chul Yoon for his help during the "decoding" of the wavelet analysis "mystery".

TABLE OF CONTENTS

LIST OF TABLES

LIST OF FIGURES

Images in this dissertation are presented in color.

KEY TO ABBREVIATIONS

ALE: Arbitrary Lagrangian Eulerian

AFM: Atomic Force Microscopy

BSE: Backscattered Electrons

CLSM: Confocal Laser Scanning Microscopy

CWT: Continuous Wavelet Transform

DOF: Depth of Field

DWT: Discrete Wavelet Transform

EDS: Energy Dispersive X-ray Spectroscopy

EFI: Extended Focal Images

FEM: Finite Element Method

FOV: Field of View

$(FWHM_{theory})_{LAT}$: Lateral theoretical resolution

$(FWHM_{theory})_{AX}$: Axial theoretical resolution

FWT: Fast Wavelet Transform

HEI: Height Encoded Image

HiD: High-pass decomposition filter

HiR: High-pass reconstruction filter

HRP: Hot-rolled pearlitic

LoD: Low-pass decomposition filter

LoR: Low-pass Reconstruction filter

IMI: Intensity Maxima Images

IWT: Inverse Wavelet Transform

MACE: Major Cutting Edge

MICE: Minor Cutting Edge

MRA: Multi-Resolution Analysis

MCD: Maximum Crater Depth

MCDL: Maximum Crater Depth Location

MLCCT: Multilayer Coated Carbide Tool

MTL: Maximum Temperature Location

NA: Numerical Aperture

RFP: Refined pearlitic

RLIM: Reflected Light Interference Microscopy

SP: Stylus Profilometry

SM: Stereo Microscopy

SS: Step Size

SN: Optical Section Number

SEM: Scanning Electron Microscopy

SE: Secondary Electrons

XRD: X-ray Diffractometry

Chapter 1

INTRODUCTION

Tool wear is of foremost importance in metal cutting. Owing to its direct impact on the surface quality and machining economics, tool wear is commonly used to evaluate the performance of a cutting tool. Many research studies to understand and predict tool wear have been carried out. However, most of these studies are considered to be an empirical approach to tool wear. Consequently, many fundamental issues have not been resolved mainly due to the complex physics behind tool wear. The complexity delineated tool wear stems from many factors including work material, machine tool, cutting tool, coolants and cutting conditions. Because of the coupled effects of these factors, the tool-chip and tool-work interfaces have almost unidentifiable contact conditions with highly localized interfacial temperatures and tractions. In addition, the highly non-linear thermo-mechanical behaviors of a work material are heavily coupled during machining. Even if these two issues had been resolved, the exact wear mechanisms would not have been identified and described quantitatively.

During machining, the cutting tool directly interacts with a work material. A chip is generated by shearing the work material while the generated heat from plastic deformation of the work material and the interfacial friction between work material and cutting tool transfers into a cutting tool. The temperature in both work material and cutting tool increases substantially as the cutting condition becomes more severe. The cutting tool must withstand more stringent thermal loading and thus eventually will wear down. Even though the work material

experiences only transient thermal loading, the material at the newly generated surface undergoes phase transformation (Kim and Kwon, 2002). The abrasive second phase in the work material dissociates and diffuses into the work material because the solubility limit typically increases at higher temperatures. This convolutes the phenomenon that is already very complex.

Because of such complex phenomenon, many researchers took empirical approaches such as Taylor's equation. The reliance on an empirical approach to understand and predict tool wear stems from the inability to observe the physics and to identify the exact mechanisms behind tool wear. Typically multiple wear mechanisms may be present in metal cutting in most cases simultaneously (Shaw, 2005) which makes a systematic study of tool wear difficult to achieve (Rabinowicz, 1995). The responsible wear mechanisms changes depending on cutting conditions and tool-work materials combination (Opitz, 1963). Tool wear mechanisms that have been identified and are commonly accepted include adhesion (Burwell, 1955; Wright and Bagchi, 1981), abrasion (Ramalingam and Wright, 1981; Takeyama and Murata, 1963; Wright and Bagchi, 1981), diffusion (Cook and Nayak, 1969; Trent, 1963) and dissolution (Kramer and Kwon, 1985; Kramer and Suh, 1980), chemical reaction (Hartung and Kramer, 1982; Kramer, 1987) and oxidation (Wright and Bagchi, 1981). At low cutting speeds, adhesive and abrasive wear tend to be dominant, whereas diffusion, dissolution, chemical reaction and oxidation are more relevant at high cutting speeds (Stephenson and Agapiou, 2006; Takeyama and Murata, 1963; Wright and Bagchi, 1981). Cemented carbide (carbide) tools wear easily by dissolution when machining

steels (Kramer and Suh, 1980). However, when machining titanium alloys, the same carbide tools resist tool wear because of the formation of a reaction layer between carbon from carbides and titanium (Hartung and Kramer, 1982; Kramer 1987). Flank wear is originated by the abrasive action of the hard second phase in the work material (Byrd and Ferguson, 1978; Kwon, 2000; Ramalingam and Wright, 1981) while crater wear is known as a complex combination of many wear mechanisms such as adhesion (Akasawa and Hishiguti, 1980; Dixon et al., 1985), abrasion (Kramer and Kwon, 1985; Kwon, 2000), dissolution (Kramer and Kwon, 1985) and diffusion (Cook and Nayak, 1969; Trent, 1963).

Cutting temperatures, contact conditions and stresses at the tool-chip and tool-work interfaces affect tool wear and corresponding wear mechanisms (Gekonde and Subramanian, 2002; Shaw, 2005). Aggressive cutting conditions, especially high cutting speed, result in higher cutting temperatures. High cutting temperatures produce transitions from sliding to seizure contact conditions at the tool-chip interface provoking high temperatures favoring thermally activated mechanisms (Gekonde and Subramanian, 2002). The tool material softens as the cutting conditions become severe, which makes the tool susceptible to abrasion. As other mechanisms become more intense, abrasion loses the dominance on the resulting tool wear and other mechanisms become more prominent.

1.1 TYPES OF CUTTING TOOL WEAR

In a broader sense, wear is the surface damage or material removal from one or both surfaces due to the relative sliding, rolling or impact motion (Bhushan, 2002). Nevertheless, when the term is applied to tool wear, it needs to be put into perspective with the concepts of tool life and tool failure. While tool life is the time during which a tool remains usable in a metal cutting operation, tool failure represents the event that defines the end of tool life. A tool fails in three different ways: gross fracture, plastic deformation or gradual wear (Kramer, 1993). The first two represents premature failure of the tool. Gradual wear is unavoidable and is naturally expected in a typical metal cutting scenario. Tool wear is used instead of gradual tool wear in the present work and is its main focus.

A common way to categorize tool wear is focusing on the regions of the cutting tool where it can be observed (Stephenson and Agapiou, 2006). Accordingly, the following types of wear in a single-point cutting tool are identified in Figure 1: (A) flank wear, (B) crater wear, (C) notch wear, (D) nose radius wear, (E) thermal cracking, (F) parallel cracking, (G) Built-Up Edge (BUE), (H) gross plastic deformation, (I) edge chipping, (J) chip hammering and (K) gross fracture. The exact form and location of wear will somewhat vary depending on the machining operation.

The focus on this review is on (A) flank wear and (B) crater wear because they are developed in all conventional cutting operations. The rest of the cases are specific to either a particular tool-work material combination or some

machining operation. Others do not fit into the definition of gradual tool wear. Chip hammering (Figure 1-(G)) can only be seen when ceramic tools machine work materials that form a tough, abrasive chip such as stainless steel. Thermal (Figure 1-(E)) and mechanical (Figure 1-(F)) cracking are mostly observed in interrupted cutting; If present they lead to tool chipping or tool breakage. Even though the BUE formation is not a tool wear process, it can promote adhesive and abrasive wear. Gross plastic deformation cannot be categorized as gradual tool wear but can alter the wear process by changing the shape of a tool, the cutting forces and the cutting temperatures.

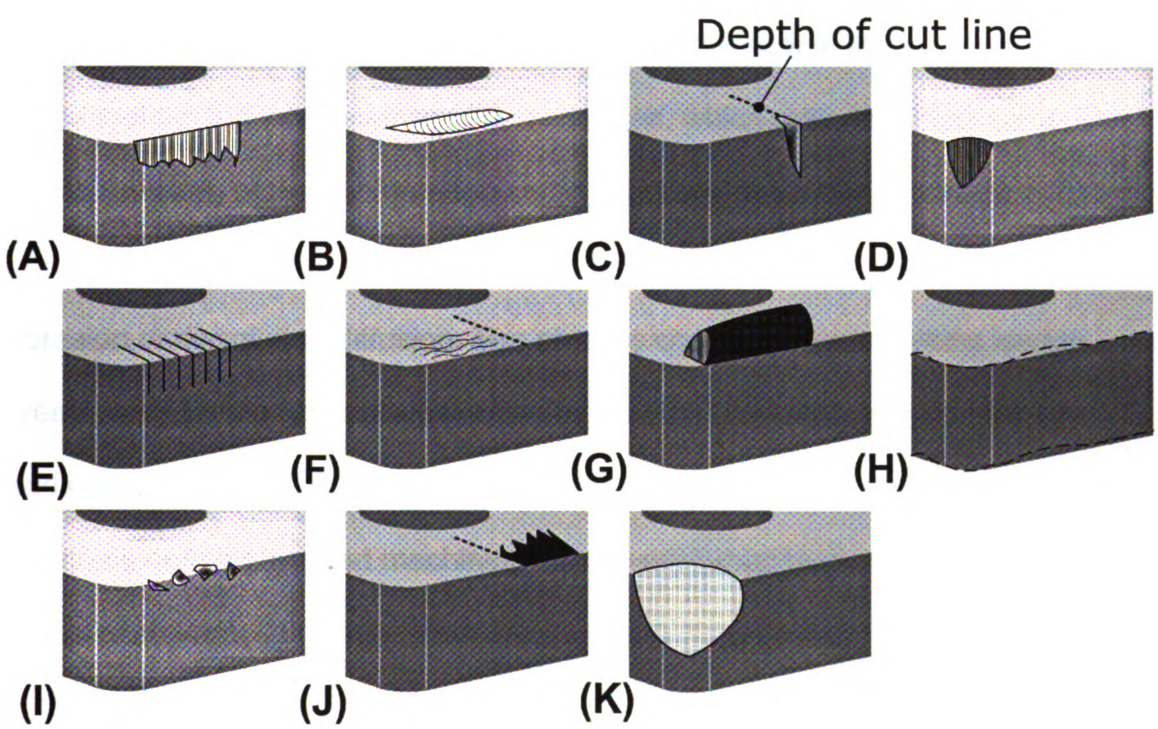

Figure 1 Tool wear types – Adapted from Stephenson and Agapiou (2006)

In a recent assessment of tool wear (Astakhov, 2006), the plastic lowering of the cutting edge is presented as a fundamental gradual process that will lead

to eventual tool failure. Finally, gross fracture is a type of failure that can happen either catastrophically at the beginning of machining process or after accumulating some gradual tool wear. The plastic lowering of the cutting edge mechanism focuses on the high-temperature bulk creep of the cutting wedge (Astakhov, 2006). According to this view, the cutting wedge is divided into three zones of different thermal-stress induced plastic deformation (see Figure 2). Zone 2 is subjected to creep due to the presence of the highest temperatures in this region. Corresponding to the actuation of the highest normal stresses on the rake and flank face besides lower temperatures, Zones 1 and 3 are not subjected to creep because of the hydrostatic state of stress, the lower temperatures, and the larger cross sectional areas, respectively. In the light of this plastic lowering of the tool tip, the interfacial condition changes, which may affect tool wear. The plastic lowering of the cutting edge could affect tool wear due to its bulk nature as opposed to the interfacial nature of more fundamental wear mechanisms such as abrasion or dissolution/diffusion. The obvious consequence of cutting wedge creep could be the gradual weakening of the cutting wedge, which ultimately ends up in fracture. The premature tool failure of difficult-to-machine work materials or in high speed machining can be explained by the plastic lowering model (Astakhov, 2004).

1.2 FUNDAMENTAL TOOL WEAR MECHANISMS

1.2.1 Adhesion

Adhesive wear occurs when one surface is sliding against another and fragments of one surface adhere to the other and then are pulled out of the original surface. The origin of adhesive wear is the strong adhesive forces that arise whenever atoms come into intimate contact (Rabinowicz, 1995). After much experimentation, the laws of adhesive wear were outlined by Rabinowicz (1995):

1. wear is directly proportional to the load between interacting surfaces
2. wear is directly proportional to the distance slid
3. wear is inversely proportional to the hardness of the material being worn away.

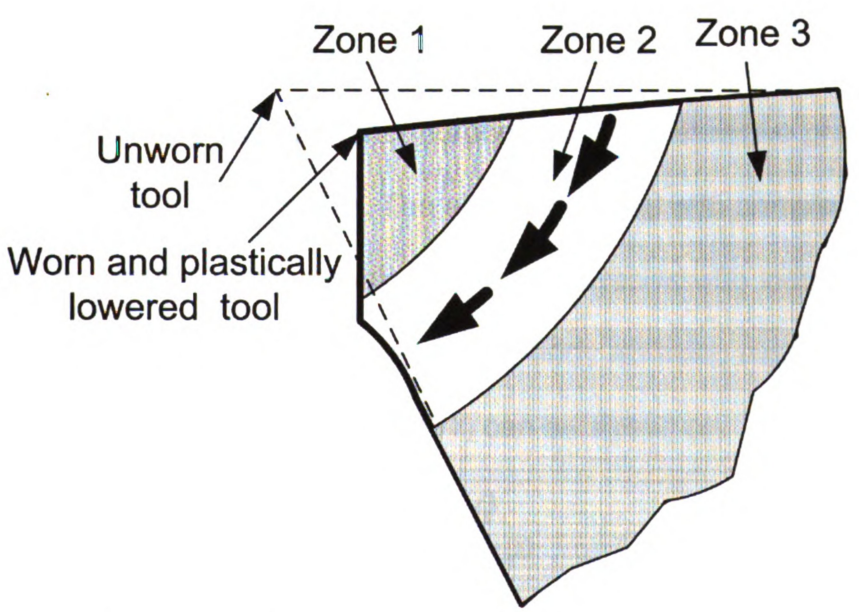

Figure 2 Plastic lowering model – Adapted from Astakhov (2006)

The most up-to-date quantitative law for adhesive wear (Rabinowicz, 1995) is the so-called modified Holm-Archard law given by

$$V = \frac{kLx}{P} \quad \ldots(1)$$

where V is the volume of wear per sliding distance, k is a probability constant, L is the load between surfaces, x is the distance slid and P is the hardness of the surface being worn. The probability constant denotes one-third of the probability of generating wear debris by the adhesion mechanism.

1.2.2 Abrasion

Abrasive wear occurs whenever a hard rough surface and/or a surface containing hard particles slides on top of a softer surface (Rabinowicz, 1995). In tool wear, abrasive wear is the removal of tool material by hard, abrasive phases in the work material. Depending on the morphology of the abrasive phases, both 2- and 3-body abrasion are possible. The abrasive phase with complex morphologies results in 2-body abrasion while the abrasive with simple morphologies results in 3-body abrasion. The 2-body abrasion model (Rabinowicz, 1977; Rabinowicz et al., 1961) can be stated as,

$$V_{2B} = \frac{L \tan\theta}{\pi P_t} x \quad \ldots(2)$$

where V_{2B} is the volume worn away, x is sliding length, L is the load between interacting surfaces, θ is the roughness angle of the abrasive and P_t is the hardness of the abraded surface. In 2-body abrasive wear, the hard particles are either hard asperities in one of the sliding surfaces or are hard second-phase particles constrained in this surface (e.g., low alloy steels contain hard cementite (Fe_3C) particles in a soft ferritic matrix). Thus, when relative sliding occurs the counter surface is abraded.

An empirical, quantitative model for 3-body abrasion which brings out parameter dependencies has been presented (Rabinowicz, 1977; Rabinowicz et al., 1961) as

$$V_{3B} = \frac{xL\tan\theta}{3P_t}, \qquad \frac{P_t}{P_a} < 0.8$$

$$V_{3B} = \frac{xL\tan\theta}{5.3P_t}\left(\frac{P_t}{P_a}\right)^{-2.5}, \qquad 1.25 > \frac{P_t}{P_a} > 0.8 \quad \text{...(3)}$$

$$V_{3B} = \frac{xL\tan\theta}{2.43P_t}\left(\frac{P_t}{P_a}\right)^{-6}, \qquad \frac{P_t}{P_a} > 1.25$$

where V_{3B} is the volume worn away and P_a is the hardness of the abrasives. The worn volume in 3-body abrasion depends on the hardness ratio between tool and abrasives. In 3-body abrasion, hard particles are either loose or free to roll in between the two sliding surfaces. In the case of metal cutting of ferrous

materials, these unconstrained hard particles can be spheroidised cementite and the debris detached from the stagnant zone. To use these models, hot hardness values for various coatings (TiN, Alumina (Al_2O_3) and TiCN) and cementite (Fe_3C) have been obtained (Kwon, 2000; Kwon and Kountanya, 1999; Wong et al., 2004) and presented in Table 1.

Table 1 Hot hardness data for various coating materials and cementite (Wong et al., 2004)

Material	P_o	$\alpha \times 10^{-3}$	Temperature Range (°C)
Cementite (Fe_3C)	1200	1.347	0-400
	3320	3.891	401-1400
TiN	2563	1.600	0-1300
Alumina	2468	1.616	0-500
	3671	2.180	501-1200
TiCN	2787	0.400	0-400
	5496	2.000	401-1200

Hot hardness data are needed to account for the thermal softening effect on the abrasive particles as well as the surface of the tool. The hot hardness data have been curve-fitted to the equation

$$P = P_o e^{-\alpha T} \quad \ldots(4)$$

where each material has characteristic values for P_o and α .

Also, the interfacial stresses on the flank face are assumed to be constant for the same cutting conditions independently of the coating; therefore, Equations (3) and (4) must be calibrated using actual experiments (Wong et al., 2004). The models represented by Equations (3) and (4) predict completely opposite trends in relation to cutting temperature as shown in Figure 3.

The relative abrasive wear rate is used to denote the dependence on the hardness ratio P_t/P_a where the tool material (TiN, Al_2O_3 and TiCN) is changed but the abrasives are always cementite particles (Fe_3C). Depending on the morphology of the abrasive phase, these distinct trends were observed in the turning experiment with low alloys steels (Kwon, 2000). These steels have been heat-treated to attain the morphology of cementite phase in either spheroids or pearlites. For spherodised steels, the observed flank wear rate had the same trend that the 3-body abrasive wear model predicted. For pearlitic steels, the observed flank wear rate had the same trend that the 2-body abrasive wear model predicts. The cementite phases in pearlitic steels are constrained due to their complex morphology and exhibited the 2-body wear condition while the spheroids are free to roll between two interacting surfaces (Kwon, 2000; Kwon and Kountanya, 1999).

When machining both pearlitic and spheroidised steels, tool wear is expected to increase with higher carbon contents in the steel. However, in machining pearlitic steels, this wear trend was not observed. Kim and Kwon (2002) have attributed this to the phase transformation of steels. As the cutting speed increases, the temperature reaches high enough to transform pearlites to

austenite. The cementite phase, which is the dominating abrasive in low alloy steels, no longer exists as the work material (steel) traverses across the flank surface. This has been experimentally verified by detecting retained austenite on the newly machined surfaces using X-ray diffraction.

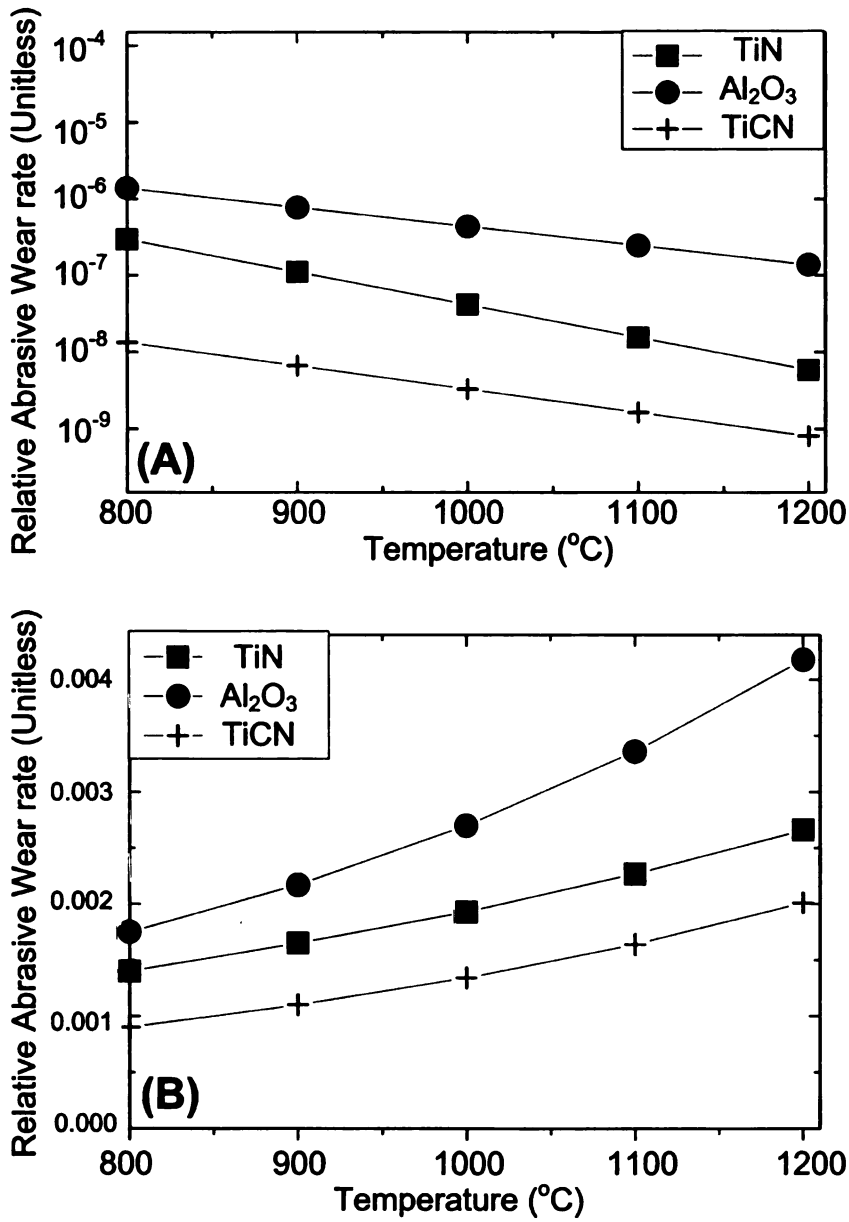

Figure 3 (A) 3-body wear model (B) 2-body wear model (Kwon, 2000)

The exact condition for phase transformation depends on the alloying ingredients which change the transformation temperature and composition. This may explain wide variations in tool wear data in the literature. The abrasive wear and phase transformation have been demonstrated with turning experiments using low alloys steels (Kim and Kwon, 2002; Kwon and Kountanya, 1999; Wong et al., 2004).

1.2.3 Diffusion

Solid-state diffusion takes place from regions of high atomic concentration to regions of low atomic concentration. The diffusion rate increases exponentially with temperature. Diffusion can occur in metal cutting due to the intimate contact at high temperatures in a very narrow reaction zone between the tool and the chip (Cook and Nayak, 1969; Naerheim and Trent, 1977). Diffusion wear mainly causes weakening of the surface structure of the tool (Boothroyd and Knight, 1989). According to Molinari and Nouari (2002), the diffusion mechanism is described by

$$\frac{\partial C_{i1}}{\partial t} = D_{i1}\frac{\partial^2 Ci1}{\partial y^2}$$

$$\frac{\partial C_{i2}}{\partial t} = D_{i2}\frac{\partial^2 Ci2}{\partial y^2} - V_c\frac{\partial C_{i2}}{\partial x} \quad \ldots(5)$$

where Vc is the chip bulk velocity, C_{i1} and C_{i2} are the concentrations of the species i in the tool and chip, respectively, D_{i1} and D_{i2} are the diffusion coefficients of species i in the tool and chip, respectively and t is time. Diffusion wear becomes a possibility when the interface temperatures of sliding surfaces are relatively high and velocities in the close neighborhood are low. This condition can be found exclusively in heavily loaded sliders along with subsurface flow. For this case, the high speeds above the layer can account for the high temperatures while the relative low speeds near the bottom of the layer can account for longer contact times needed for diffusion (Shaw, 2005). Experimental research in diffusion wear is difficult to perform because a real cutting experiment is the only way to mimic all conditions, which implies having multiple wear mechanisms in addition to diffusion (Shaw, 2005).

1.2.4 Dissolution

In dissolution wear, the tool dissociates into its elementary species which then are removed from the tool material to form a solid solution within the flowing chip. Because of the high temperature required for dissolution wear to occur the machining conditions must be severe. The rake face is the site where dissolution is most likely to occur. Dissolution wear depends on the chemical inertness of the tool material as well as on the chemical affinity of the tool components with the chip material. At relatively high cutting speeds, dissolution wear dominates the

wear process; a quantitative model has been developed by Kramer (1979) and presented in Kramer and Suh (1980). For example, for a given ternary tool material of composition, $A_xB_yC_z$, the chemical solubility may be determined with the thermodynamic equilibrium condition (Kramer and Suh, 1980),

$$\Delta G_{A_xB_yC_z} = x\Delta\overline{G}_A + y\Delta\overline{G}_B + z\Delta\overline{G}_C \quad ...(6)$$

Where $\Delta G_{A_xB_yC_z}$ is the free energy of formation of the tool material at the tool-chip interface, T is the solution temperature and $\Delta\overline{G}_i$ ($i = A$, B, or C) is the relative partial molar free energy of component i within the solution (measured relative to the pure state of i at the same pressure and temperature as the solution) which is

$$\Delta\overline{G}_i = \Delta\overline{G}_i^{xs} + RT\ln S_i \quad ...(7)$$

where $\Delta\overline{G}_i^{xs}$ is the molar excess free energy of component i in the solution, R is the universal gas constant, T is the temperature in Kelvin and S_i is the equilibrium concentration of species i in the solvent, i.e. the solubility of i in the solvent at equilibrium. From Equation (7) and data on S_i at a given T, the excess free energy of component i into the matrix of a work material can be

estimated. Further, $\Delta\overline{G}_i^{xs}$ is taken as a constant in the low limit of solubility (Henry's law).

$$\Delta G^{xs} = x\Delta\overline{G}_A^{xs} + y\Delta\overline{G}_B^{xs} + z\Delta\overline{G}_C^{xs} \quad ...(8)$$

If we take

$$M = x \cdot \ln x + y \cdot \ln y + z \cdot \ln z \quad ...(9)$$

$$N = x + y + z \quad ...(10)$$

Then, the chemical solubility, S_{AxByCz} of a tertiary coating material, AxByCz, in a work material (in mole fraction):

$$S_{A_xB_yC_z} = \exp\left(\frac{\Delta G_{A_xB_yC_z} - \Delta G^{xs} - RTM}{NRT}\right) \quad ...(11)$$

In the case of a binary compound, e.g. TiN, the evaluation of free energy of formation is given as

$$\Delta G_{A_xB_y} = x\Delta\overline{G}_A + y\Delta\overline{G}_B \quad ...(12)$$

where A = Ti, x = 1, B = N and y = 1. The solubility expression becomes

$$S_{A_xB_y} = \exp\left(\frac{\Delta G_{A_xB_y} - \Delta G^{xs} - RTM}{NRT}\right) \quad ...(13)$$

Dissolution together with abrasion has been used to predict crater wear in machining low alloy steels (Wong et al., 2004). The values of the free energy of formation are obtained from the thermodynamic literature (Kubaschewski et al., 1967), Kramer and Kwon, 1985 and Kim (2000). Thermodynamic properties for the three coating materials, TiN, TiCN and alumina and carbides are shown in Tables 2 and 3. The dissolution of a tool material is assumed to obey Henry's law because the amount of tool material dissolved into chip during the cutting process is small enough to be considered dilute.

Dissolution wear has been very successful to explain tool wear in carbide tools, coated carbide tools (Kramer, 1987; Wong et al., 2004) and ceramic tools (Vleugels and Van der Biest, 1999). Figure 4-(A) through 4-(C) shows the chemical solubility of WC, TiC, TiN, TiCN and Al_2O_3, on steel (α-iron) plotted against temperature and calculated with Equations (11) and (13). A clear ranking of tool materials based solely on their calculated dissolution wear resistance is observed. In one extreme there is WC with a relatively poor wear resistance against dissolution. Alumina (Al_2O_3), on the other extreme, is the most dissolution resistant material.

Alumina represents a good example of a highly diffusive oxide resisting wear due to its low dissolution tendency into the chip. Figures 5-(A) through (C) show the chemical solubility of WC, TiC, TiN, TiCN and Al_2O_3 on austenite (γ-iron). These plots follow the assumption that ferrite in pearlite transforms into austenite (γ-iron) at high cutting speeds (Wong et al., 2004).

Table 2 Free energy of formation for different tool materials (Kramer and Kwon, 1985; Kim, 2000)

Tool Material	$\Delta G_{AxBy} = K_1 + K_2 T \log T + K_3 T$ (Cal/mol)			Temperature Range (K)
	K_1(L)	K_2(M)	K_3(N)	
TiN	-80250	0	22.2	0-1155
	-80850	0	22.77	1155-1900
Al_2O_3	-400,810	-3.98	87.64	0 - 923
	-405,760	-3.75	92.22	923 - 1800
WC	-9000	0	0.4	298 - 2000
TiCN	-62725	0	11.81	1155-1900
TiC	-43750	0	2.41	298-1155
	-44600	0	3.61	1155-2000

Table 3 Excess free energy of solution of tool constituents in steel and titanium (after Kramer, 1979; Wong et al., 2004; Hartung, 1981)

Tool Constituent	Work Material		
	Fe-α	Fe-γ(*)	Ti
	$\Delta\overline{G}_i^{xs}$ at 1600K (Cal/mol)	$\Delta\overline{G}_i^{xs}$ (Cal/mol)	$\Delta\overline{G}_i^{xs}$ at 1200K (Cal/mol)
Ti	-6900	-1658	0
N	5700	-28, 537	-49,239
Al	-10700	-15739	-32,744
O	-12600	-12,127	-96,156
W	-7110	-7110(**)	-6214
C	7600	7504	-28,648

1.2.5 Chemical reaction

The dissolution theory breaks down when machining highly reactive materials such as titanium, in which case a chemical reaction followed by diffusion is more plausible (Hartung and Kramer, 1982). Strictly speaking, chemical reaction is not a wear mechanism. However, if chemical reaction occurs, it can affect tool wear tremendously when the tool material reacts with the work material or other chemicals to form compounds that are carried away in the chip stream or in the generated surface of the workpiece (Childs et al., 2000).

Chemical wear becomes predominant as cutting speed increases when machining highly reactive materials such as titanium alloys or when using sulphur or chlorine in the cutting fluid. Either coating tools or changing additives in the cutting fluid will improve wear resistance against chemical reaction (Stephenson and Agapiou, 2006).

1.3 GENERALIZED VIEW OF WEAR MECHANISMS

Among the five wear mechanisms mentioned in Section 3, three wear mechanisms have been identified for steady state wear:

- Abrasion
- Generalized Dissolution
- Adhesion.

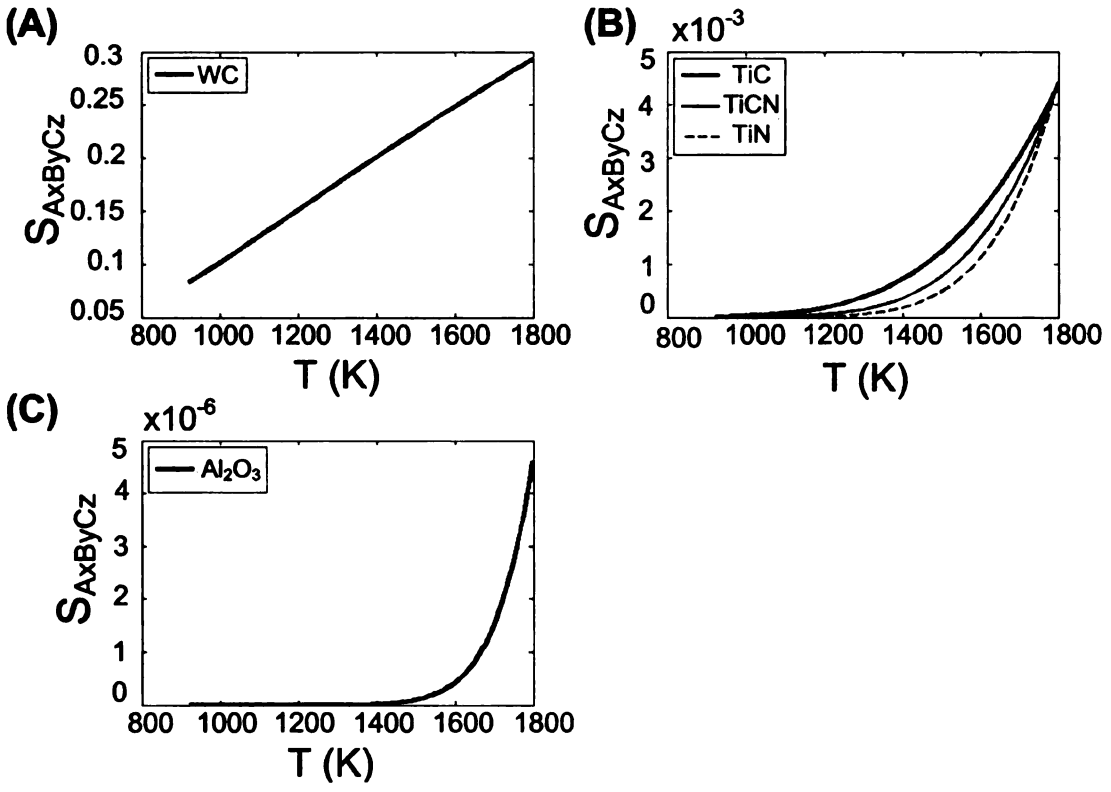

Figure 4 Solubility of various tool materials in ferrite (steel)

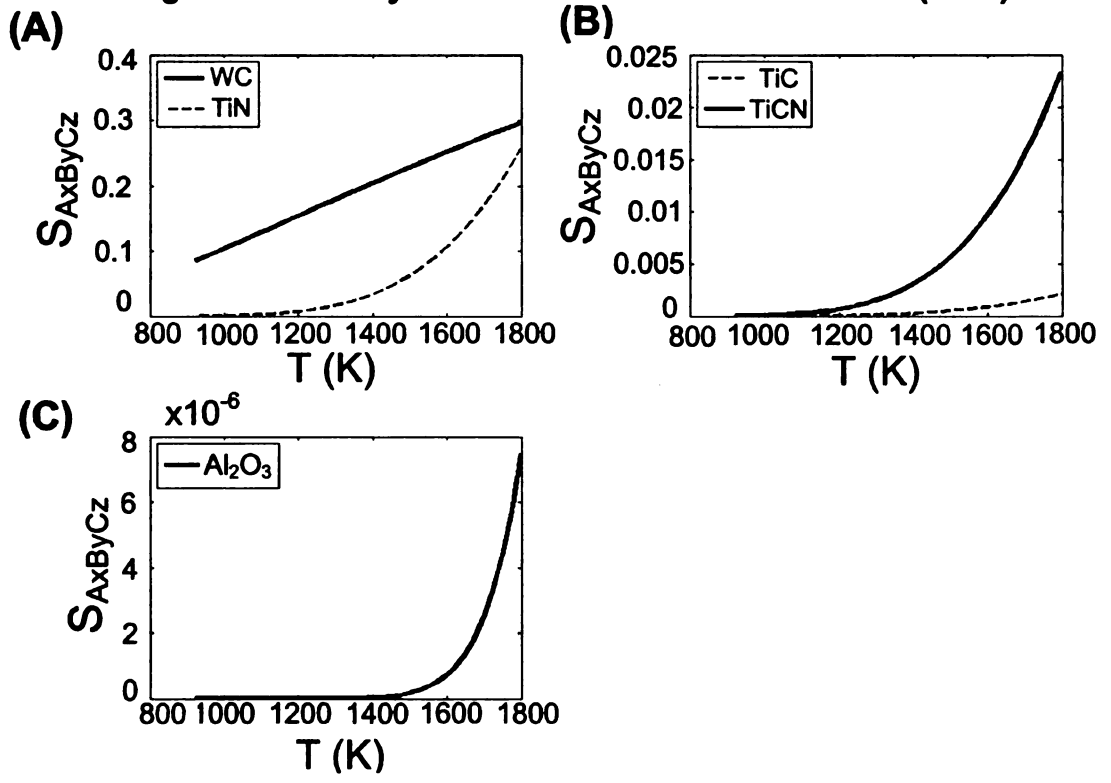

Figure 5 Solubility of various tool materials into austenite (steel)

The generalized dissolution consists of:

(i) Dissociation of tool material

(iia) Chemical reaction of dissociated species with work material if the reaction is feasible

(iib) Atomic transport across the tool-chip interface

(iii) Diffusion of the dissociated species that have not been consumed in the chemical reaction.

The ceramic coating material, symbolized by AxBy, must dissociate into species, xA and yB. One of the faster diffusing species can diffuse into the work material. Alternatively, the dissociated species can react with the work material to form a layer. Most likely the reaction layer will reduce the tool wear rate. For flank wear, abrasive wear convoluted by phase transformation seems to be the only wear mechanism. Because of the distinct scoring marks, the abrasive wear can be distinguished and the phase transformation can be identified by X-Ray Diffraction (XRD) techniques on the newly formed surface and the extent of abrasive wear (Kim and Kwon, 2002). The morphology of the second phase dictates the wear behaviour to be of either 2- or 3-body abrasion type. Then, the abrasive wear models (Rabinowicz et al., 1961) can be applied including with hot hardness ratios between second hard phase and coating to describe the wear process as seen in machining ferrous materials with cementite phase (Kwon and Kountanya, 1999; Kwon, 2000; Wong et al., 2004). It is quite possible that phase transformation occurs in allotropic work materials such as titanium alloys and ferrous materials and even solution-hardened alloys such as aluminum alloys. In

addition, new alloying ingredients and an optimum heat treatment schedule for the work material can be recommended to reduce abrasive wear.

In Figure 6, the three mechanisms are presented for crater wear. Abrasion indicated by the arrow #1 in Figure 6-(B) comes from the hard second phase in the work material (e.g. cementite in low alloy steels) abrading the coating material as in the flank wear. However, the distortion in the microstructure of the chip is so severe that it is most likely to be modelled by only 3-body abrasive wear.

Hitherto, it is not clear whether diffusion or dissolution is the more adequate wear mechanism to describe tool wear at high cutting speeds. In addition, machining of highly reactive materials such as titanium and its alloys open the possibility to chemical reaction at the tool-chip interface (Hartung and Kramer, 1982). The inadequacy of diffusion wear (Cook and Nayak, 1969; Trent, 1963) to explain the observed wear rates of carbides, the wear resistance of the highly diffusive oxides at high cutting speeds and the lack of experimental support were noted by Kramer (1979). On the other hand, supporters of the diffusion wear mechanism argue that wear by dissolution, being based on chemical equilibrium, does not correspond to the irreversibilities inherent to cutting operations (Wong and Kwon, 2006).

The generalized dissolution includes the dissociation of the coating material, interfacial atomic transport of dissociated species and/or the chemical reaction among dissociated species and work material and the subsequent diffusion (Hua and Shivpuri, 2005; Wong and Kwon, 2006) into the work material.

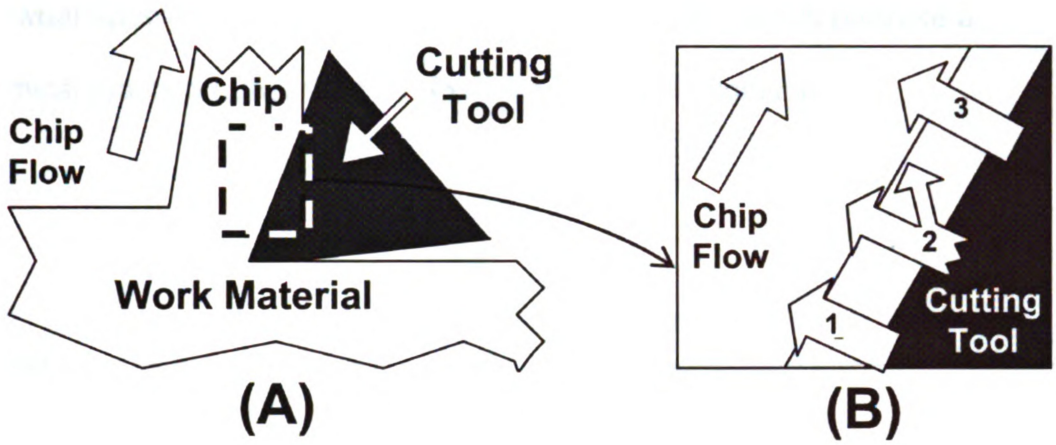

Figure 6 Wear Paths of Tool Material into Chip

In Wong and Kwon (2006), the dissolution hypothesis of tool wear is reformulated as a boundary condition for the transfer of tool species into the chip stream via diffusion. In other words, dissolution wear is defined more generally as the combined events of dissociation at the interface and the subsequent diffusion of decomposed elements into the chip region. Chemical equilibrium is invoked for the distribution of tool species at the tool-chip interface. In case of machining titanium alloy with uncoated carbide tools, a TiC layer from the carbon atoms (dissociated from tungsten carbide) and titanium in the work material was found at the interface (Hartung and Kramer, 1982). The diffusion rate of carbon through this reaction layer is much lower as compared to the case where a reaction layer is not present, thus reducing the wear rate. Consequently, many coated tools do not outperform uncoated carbide tool when machining titanium alloys. The solubility beyond 1.0 (100%) in titanium for every tool material as shown in Figure 7-(A) and (B) is meaningless. These results have been interpreted as a high chemical reaction potential available between dissociated

tool wear species and the tool material (Hartung, 1981) which promote a chemical reaction rather than the formation of a solid solution.

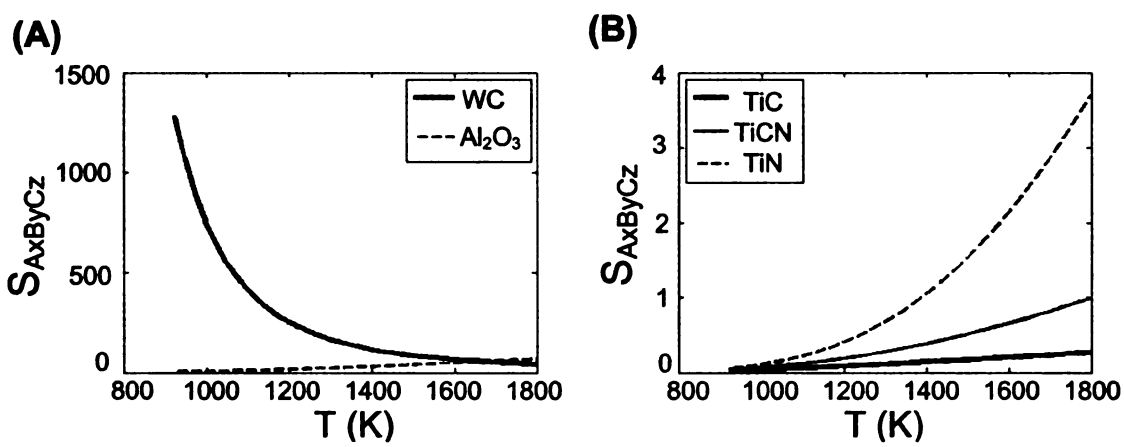

Figure 7 Solubility of various tool materials in titanium

The possibility of a chemical reaction can be verified using the concept of Gibb's free energy. Equations (14)–(17) which are presented on the next page and the thermo-chemical data shown in Appendix D were used to calculate the plot in Figure 8.

$$WC + Ti \rightarrow TiC + W \quad ...(14)$$

$$\Delta G_T = \Delta H_T - T\Delta S_T \quad ...(15)$$

$$\Delta H_T = -(H_f)^o_{WC} - \int_{298}^{T} \Delta Cp_{WC} dT + (H_f)^o_{TiC} - \int_{298}^{T} \Delta Cp_{TiC} dT + \sum H_t \quad ...(16)$$

$$T\Delta S_T = T\left[-(S_f)^o_{WC} + (S_f)^o_W + (S_f)^o_{TiC} - (S_f)^o_{Ti} - \int_{298}^{T} \frac{\Delta Cp_{WC}}{T} dT + \int_{298}^{T} \frac{\Delta Cp_{TiC}}{T} dT + \sum \left(\frac{H_t}{T_t} \right) \right] ...(17)$$

where

T : Absolute temperature at which the reaction occurs

ΔG_T : Gibb's free energy of reaction

ΔH_T : Enthalpy change

ΔS_T : Entropy change

$\sum H_t$: Summation of all the heats of transformation in the temperature range of interest

$\sum\left(\frac{H_t}{T_t}\right)$: Entropy change associated with phase transformations

$(H_f)^o_{WC}$ and $(H_f)^o_{TiC}$: Standard enthalpies of formation

$(S_f)^o_{WC}, (S_f)^o_W, (S_f)^o_{TiC}, (S_f)^o_{Ti}$: Standard entropies of formation

ΔCp_{WC} and ΔCp_{TiC} : Changes of specific heat at constant pressure for the dissociation reaction of WC and the formation reaction of TiC, respectively.

It should be noted that the integrals in Equations (16) and (17) will be broken into smaller temperature ranges due to the variation of the specific heat coefficients before and after a solid-solid phase transformation such as the one

happening for Titanium at 1155 K (Appendix D). By the same token, the Gibbs' free energy for the reaction, WC + Fe → Fe_3C + W, was calculated and the results are also plotted in Figure 8. The data for heat capacities, standard entropy of formation and standard enthalpy of formation are tabulated in Table 4. As it can be observed from Figure 8, the Gibb's free energy for the reaction WC + Ti → TiC + W possesses a value of almost an order of magnitude larger than that of the reaction WC + Fe → Fe_3C + W. Then a chemical reaction (forming TiC) is more likely to happen when machining titanium with carbide tools than in the case of machining steel with the same tools (forming Fe_3C).

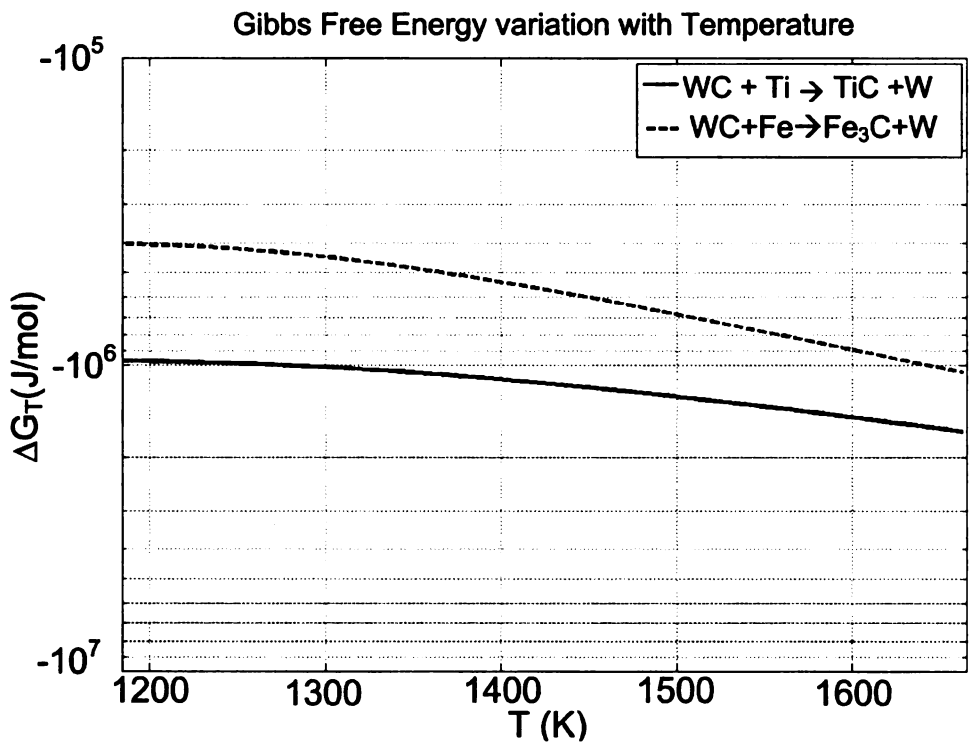

Figure 8 Gibbs free energy for the reactions: WC + Ti → TiC + W and WC +Fe → Fe3C+W

Considering the chemical reaction and the diffusion, the source of the species in cutting tool material is the same. If the chemical reaction does not

consume the species that has been dissociated or does not exist, these species will either diffuse into the chip to form a solid solution or will be carried out on the underside of the chip out of the crater zone. The split in the arrow #2 in Figure 6(b) represents the reaction route and the subsequent diffusion into the chip. The reaction is expected to be important with high dissociation and low diffusion as the element from the coating cannot be consumed in the process of diffusion.

Adhesion indicated by the arrow #3 in Figure 6-(B) represents the formation of strong bonds at the interface tool-work with the subsequent detachment of tool material. Rabinowicz (1995) developed the adhesive model using surface energy and hardness values. Prediction with Equation (1) is not necessarily accurate as the interface surfaces are under hydrostatic pressure which making the condition detachment hard to predict. In Al_2O_3 coated tools, sometimes grain pull-out has occurred as a result of adhesive wear (Kim, 2000). The delamination/thermal cracking and detachment of coating can occur; however, no model that describes this complex phenomenon exists in literature. This can happen due to the high cutting temperature as in machining titanium alloys due to their low thermal conductivity causing a high thermal gradient and/or thermal fatigue loading typical in milling operations. The mismatch in the coefficient of thermal expansion between substrate and coating or among multilayers contributes to this type of tool damage. The enhancement of the interfacial strength may help but the properties of coating materials have to be designed with those of the substrate or other coatings in mind.

1.4 TOOL WEAR MECHANISMS SUMMARY

In this chapter the possible wear mechanisms involved in single-point cutting tools used in machining have been reviewed. The conclusions have been justified logically using the experimental data as well as the thermo-chemistry analysis. The generalized dissolution for crater wear where the complex cutting tool material is dissociated before the interfacial atomic transport, chemical reaction and/or diffusion takes place was proposed. The dissociated species react with detached work material if such process is thermodynamically feasible. If not, the dissociated species from a tool diffuses into the chip. 3-body abrasive wear is found to be the more plausible model for crater wear. Whether abrasive wear is the only main wear mechanism for flank wear is not clear. However, the experimental studies (Kwon, 2000; Kwon and Kountanya, 1999; Wong et al., 2004) indicate that this assumption is not far fetched. The main obstacle to predict flank wear is the phase transformation. The 3-body model is quite good in predicting flank wear if phase transformation does not affect the abrasive phase. Even though this has only been shown for ferrous materials, it is quite possible that other materials such as solution harden Aluminum alloys and titanium alloys undergo phase transformation. The morphology and size of the abrasive phase affect tool wear; however, their contribution has not been clearly elucidated.

Chapter 2

EXPERIMENTAL FINDINGS ON THE TOOL WEAR IN MULTI-LAYER COATED CARBIDES

Several experimental works have been carried out to reveal tool wear mechanisms in single and multiple-layered coated carbides. Crater wear and flank wear of single-layer coated carbides have been observed to be produced mainly by the plastic deformation of the coating material followed by bulging (Srinivasan et al., 1977). A marked improvement on flank wear resistance in high-speed machining of stainless steels with coated tools has been reported (Chubb and Billingham, 1980). In another study using Auger electron microscopy (Chubb et al., 1980), it was found that the TiN outer layers reduced tool/chip adhesion and that its main wear mechanism was abrasion. Interestingly, it was observed that wear resistance is not drastically improved by coating thickness and that the wear mechanisms were similar to uncoated tools once the coatings were worn through. The crater wear rate in coated carbides was reduced according to the coating's chemical stability rather than by the decreased interfacial friction or cutting temperature (Dearnley and Trent, 1982). It has been also proposed that Multilayer Coated Carbide Tools (MLCCTs) provide an optimal combination of hardness/toughness ratio, fatigue resistance, stress resistance, and adherence (Holleck, 1986). The substrate-coating combination is also believed to play a role in the performance of coated tools. A marked difference in the cutting forces was observed when different substrate-coating combinations were used (Seah et al., 1995). The fraction of the external work

consumed in deforming the top layer was claimed to be a key factor in reducing crack-propagation rates, thus allowing a better wear resistance of three-layered coatings compared to two-layered ones (Cho and Komvopoulos, 1997). Another study by Cho and Komvopoulos (1998) proposed that the wear rate of MLCCTs near the final stage of tool life increases substantially because of the delamination of the coatings. At moderate-speed turning tests, tool wear was observed to predominantly wear by chipping/fracture and nose wear; however, at high cutting speed, attrition, local plastic flow, and dissolution-diffusion were reported to be dominant (Ezugwu et al., 2001). Alternating layers of Al_2O_3/TiC coatings on carbides were analyzed using transmission electron microscopy techniques (Larsson et al., 1999). The transformation of metastable k-Al_2O_3 into more stable α-Al_2O_3 was observed. According to this study, this transformation increases the possibility of wear due to local plastic deformation. The use of an intermediate layer of Al_2O_3 in three-layered coatings was observed to be detrimental for the wear resistance at low speeds (0.5 m/s) in a pin-on-disc test (Grzesik et al., 2002); however, as speed increases, the presence of the intermediate layer seems to increase the wear resistance beyond 0.5 m/s. Lately, it has been observed that a MLCCT with an intermediate layer of Al_2O_3 modifies the heat generated and increases in 30% the heat transferred to the chip stream compared to the uncoated case (Grzesik and Nieslony 2003). Mohan and Balaji (2002) investigated the effects of the multi-layers coatings and individual coating by observing the tool-chip contact length with respect to undeformed chip

thickness, varying cutting conditions and thermal conductivities based on Oxley's model.

In this chapter, results from Finite Element Method (FEM) simulations in Arbitrary Lagrangian Eulerian (ALE) formulation were applied to relate the observed tool wear with the interfacial conditions. The details on the ALE-FEM model developed by our Predictive Tool Wear research group at Michigan State University are outlined in Appendix A.

The characterization of the worn tools and work material was achieved by means of Confocal Laser Scanning Microscopy (CLSM), Stylus Profilometry (SP), Scanning Electron Microscopy (SEM), X-ray Diffractometry (XRD), Metallography, and hardness measurements. These experimental techniques used in combination with the results from the ALE-FEM aided in determining the rationale for the outstanding wear-resistant properties of multilayer coated-carbides. The details on the CSLM application to cutting tool wear analysis in multi-layer coating systems are presented in Appendix B.

2.1 EXPERIMENTAL SETUP AND PROCEDURE

2.1.1 Machining Experiments

A MAZAK, Super Quick Turn 200M CNC lathe was used to dry-turn two types of 1045 steel bars hot-rolled pearlitic (HRP); and refined pearlitic (RFP) with C6 inserts coated with the consecutive layers of TiCN (bottom), Al_2O_3, and TiN (top). Machining conditions were kept constant at 250 m/min, 0.3048

mm/rev, 1.905 mm for cutting speed, feed rate and depth of cut, respectively. Flat-faced inserts with designations ISO SNMA190612 (geometry) and KC9315 (grade) provided by Kennametal Inc. were used to avoid the influence of tool geometry in tool wear patterns. Two set of experiments were run starting always from fresh corners. The first set of experiments was run for 1, 3, 6, 8, 12, 16, 18, 20, 22, 23, 24, 26 min. with HRP 1045 bars. The second set of experiments with RFP 1045 bars was run including 3, 7, 8, 12, 20, and 23 min beyond which the carbide was exposed.

A grinder run with a WC sphere and diamond slurry was used to make calottes. The calottes are used to estimate the coating thickness based on the inner and outer diameters of the exposed coatings as well as the sphere diameter. Seven individual calottes were made in two different new inserts and the average thicknesses were found to be 2.14 μm for TiN, 9.16 μm for Al_2O_3, and 7.58 μm for TiCN with variances of 0.08, 0.07, and 0.36 μm^2, respectively. Figure 9-(A) shows an optical image of a calotte exposing the TiN, Al_2O_3 and TiCN coatings and the WC substrate.

2.1.2 SEM pictures and EDS analysis

The worn cutting tools were characterized using a JEOL JSM-6400 Scanning Electron Microscope in both Secondary Electrons (SE) mode and Backscattered Electrons (BSE) mode. In addition, Energy Dispersive X-ray Spectroscopy (EDS) was done along with BSE images. The accelerating voltage

and the working distance were set at 20 KV and 15 mm. In general, EDS and BSE micrographs were used to discriminate among coatings, substrate and work material while SE images were utilized for topographical visual inspection and later for the discrimination of Al_2O_3 polymorphs. Multiple magnifications were used to capture crater and flank wear patterns.

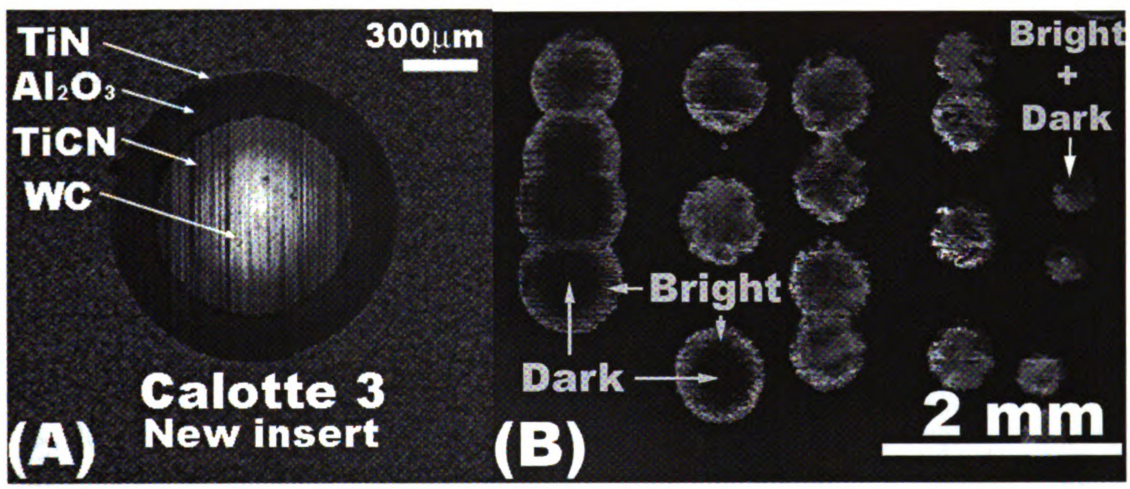

Figure 9 (A) Optical view of a calotte (B) SE image of the calotte array on a new insert.

2.1.3 X-Ray Diffraction (XRD) Analysis

An array of calottes was performed on the surface of a fresh insert as shown on Figure 9-(B) and the grinding times were carefully controlled to expose the Al_2O_3 coating at various depths. The SE micrographs show the presence of "bright" and "dark" phases in the Al_2O_3, indicating the presence of both α- and κ-Al_2O_3 (Larsson, 2000). The X-ray Diffraction (XRD) analysis shown in Figure 10 proves the existence of α-phase ("bright") and κ-phase ("dark") in the Al_2O_3

coating as Halvarsson et al. (1999) and Soderlund et al. (1994) also observed. The multiple XRD peaks in Figure 10 correspond to the various x-ray energy levels (compound "fingerprint") and different crystallographic planes exposed by the calottes. These XRD peaks were matched to the standardized XRD powder diffraction data for TiN, α-and κ-Al_2O_3 (Halvarsson et al., 1999).

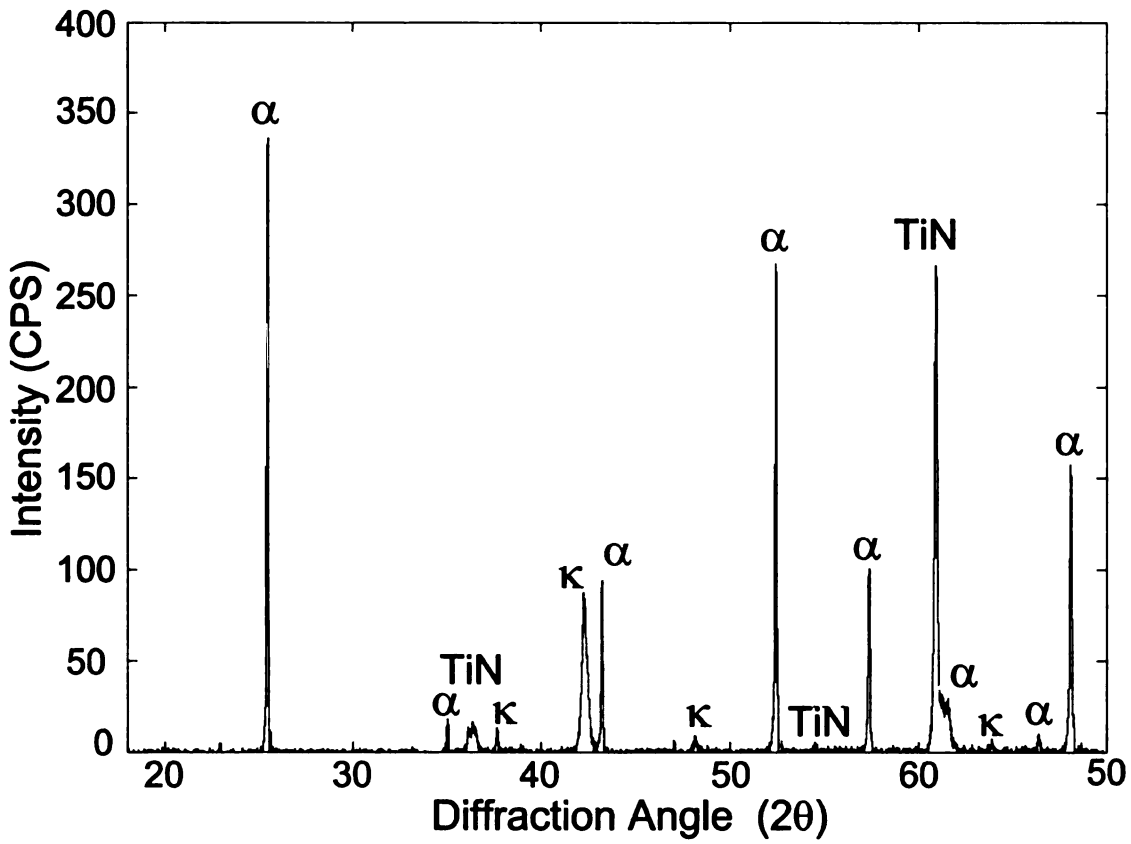

Figure 10 XRD pattern performed on the calotte array zone.

2.1.4 Profiler measurements

A Veeco Dektak-6M stylus profiler was use to obtain profiles of the crater regions containing the maximum crater depth. Profiles were obtained parallel to

the Minor Cutting Edge (MICE). The data sets were collected using a scan length of 4000 μm, a stylus diamond tip of 2.5 μm, stylus force of 3mg, a resolution of 0.444 μm/sample, and vertical range extensions at 65.5 μm and 262 μm.

2.1.5 CLSM topography

A Zeiss LSM210 Microscope was used to collect the crater CLSM topographies. 200 optical sections spaced 200-250 nm (axial accuracy) were captured for all cutting times using 10X/0.30 and 20X/0.50 objectives. A custom-developed MATLAB program was used to post-process the CLSM data.

2.2 RESULTS

Figure 11 shows the BSE images of the crater and flank wear after machining HRP 1045 steels for 3, 8, 16, 22 min and RFP 1045 steels for 23 min steels. In the rake face, Al_2O_3 was exposed at 3 min and its exposed area broadens towards the Major Cutting Edge (MACE) until 8 min. TiCN was seen for the first time at 16 min and then, the area expanded faster parallel to the MICE than towards the MACE. The carbide substrate was not exposed even after 22 min. However, after turning the RFP 1045 bars for 23 min., WC was finally exposed after 23 min. prior to catastrophic failure.

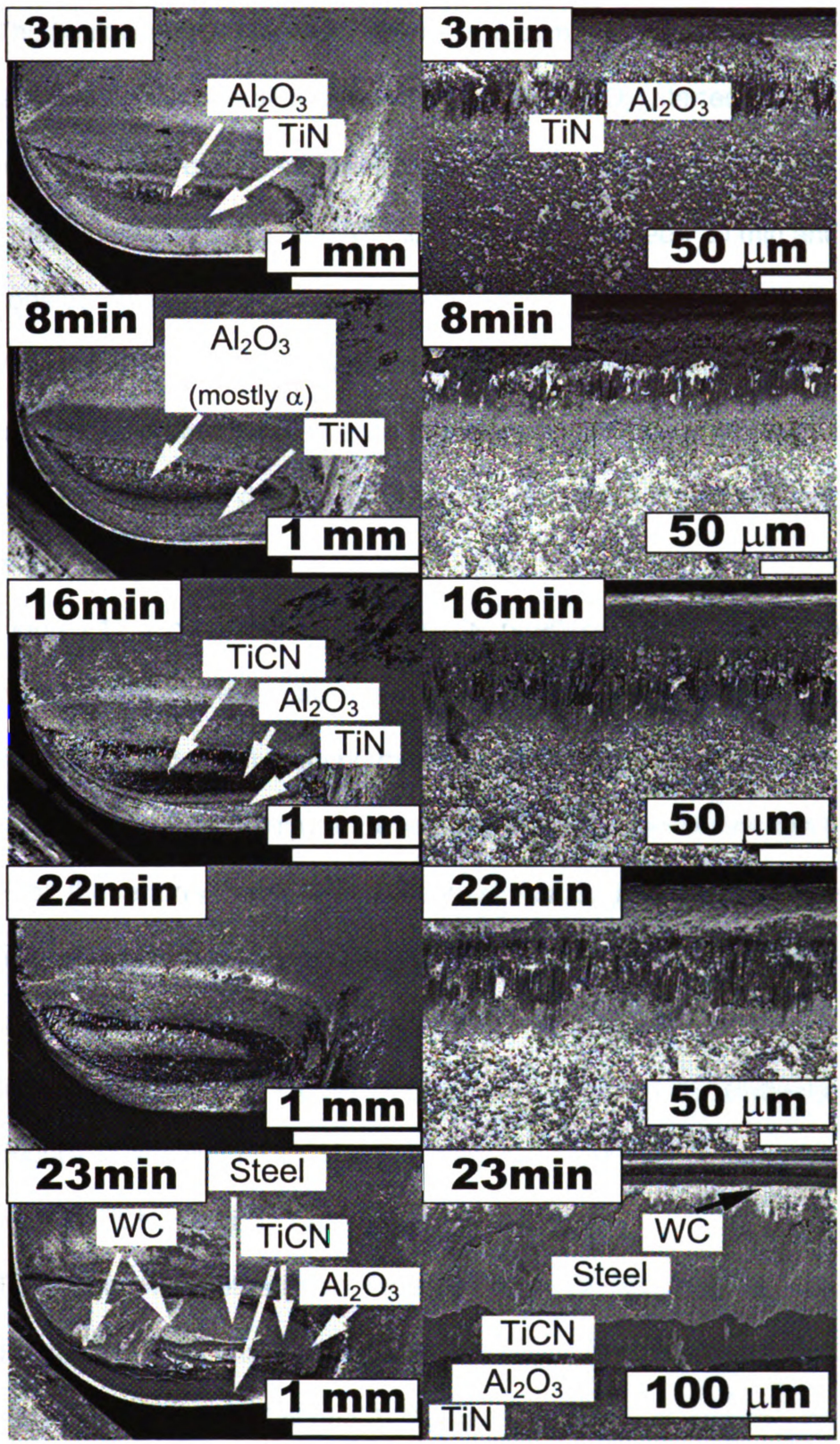

Figure 11 BSE images of crater and flank wear evolution

The flank wear land for the RFP steels is composed of TiN and Al_2O_3. It was observed that the overall wear-land width (TiN+Al_2O_3) started always below a distance of 40 μm from the top of the rake face and its value (~70 μm) did not change much between 6 min. and 18 min.. However, between 20 min and 22 min, a considerable increase was observed.

With the RFP steels, flank wear rate increased astonishingly exposing the WC substrate. An enormous difference in crater and flank wear after machining both steels was observed despite the negligible difference in their chemical composition.

Figures 12 and 13 show the Dektak-6M profiles obtained parallel to the MICE overlaid to render the crater wear evolution obtained from turning both types of steels. A mask representing the coatings thicknesses obtained with the calottes was drawn on each figure. Several interesting observations can be made. First, the retarded wear rates were observed in machining both steels as the wear front moved through the Al_2O_3 layer. Second, the original cracks in the Al_2O_3 layer were broadened without any sign of delamination. Third, a contradiction exists between Figure 11 (BSE) and Figure 12 (profilometry and mask). Figure 11 shows that TiCN is first seen at 16 min while the mask in Figure 12 shows that TiCN is initially exposed at 22 min..

To explain this contradiction, Extended Focal Images (EFI) in SE mode showed that, after TiCN was exposed (16 min.), the maximum crater depth lies close to the limit between TiCN and Al_2O_3, and that the TiCN exposed area is slanted. Figure 14 delineates this point on the cutting tool at 22 min. In both

Figures 12 and 13, the regions beyond the trailing edges were protruded while the cutting edges appeared to have been lowered, pointing to coating deformation and creep deformation of the carbide substrate, respectively.

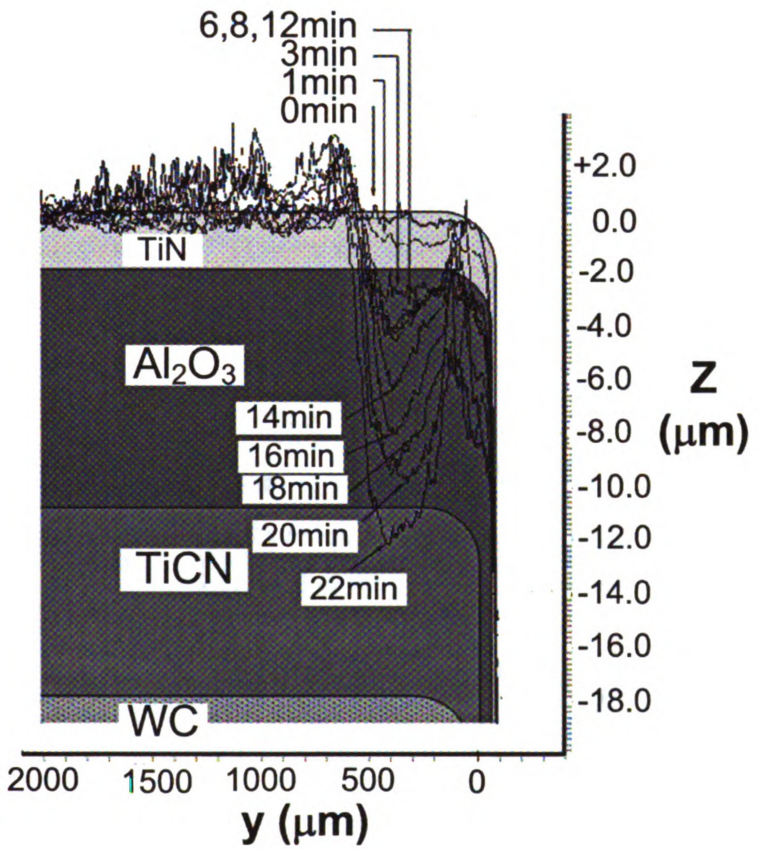

Figure 12 DEKTAK 6M crater profiles evolution 0-22min parallel to MICE while machining HRP AISI1045 steel (mask not scaled in the horizontal direction)

2.3 DISCUSSION

In Appendix B, the crater wear retardation with multilayer-coated carbides was shown to be caused by the low solubility of Al_2O_3 into steel in a first batch of

tools tried. This trend was again observed on the tools cut between 1 to 8 min in the second batch of tools tried in this chapter. In Figure 12, the "dissolution-barrier" effect of Al_2O_3 is clearly observed in the "stagnant" profiles at 6 and 8 min. A high wear rate was expected between 16 min to 22 min. after TiCN is exposed at 16 min due to the drastic increase in the solubility into steel compared Al_2O_3 (Wong et al., 2004). However, the small TiCN-exposed area is surrounded by Al_2O_3, which still provided the resistance to dissolution wear.

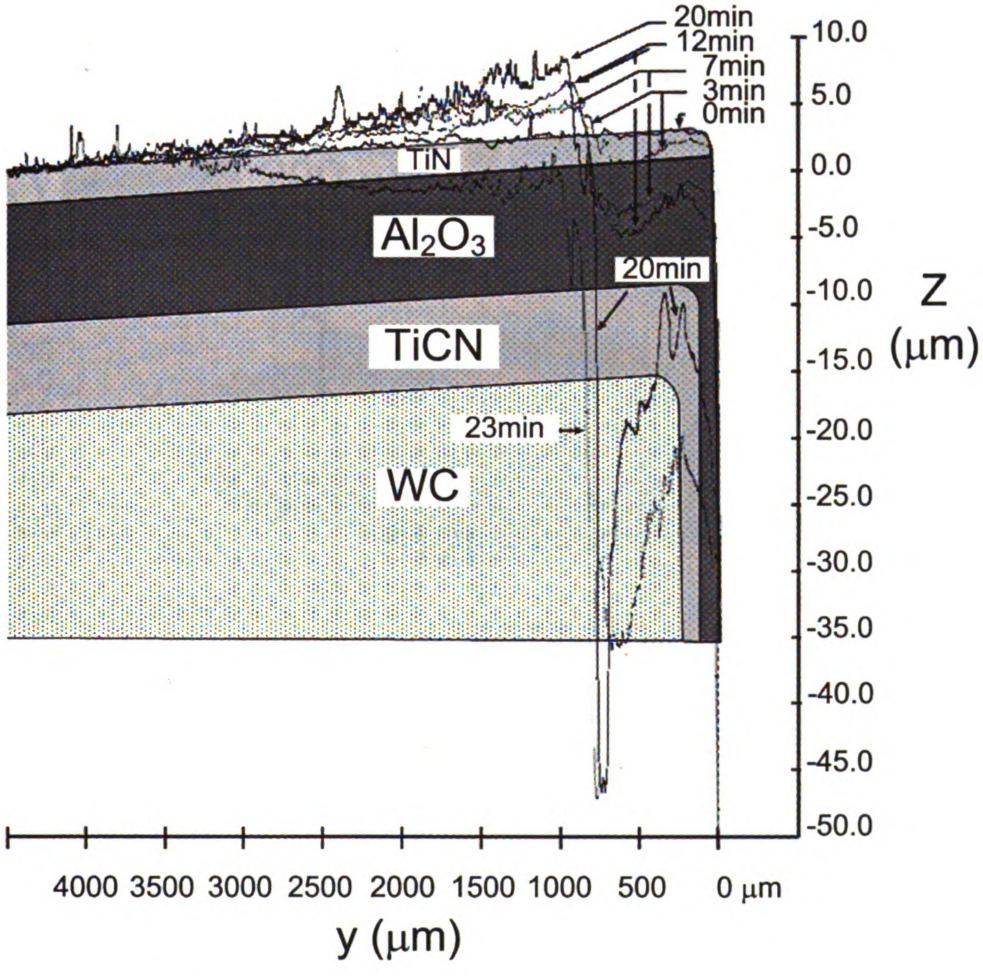

Figure 13 DEKTAK6M profiles for 0, 3, 7, 12, 20, and 23 min cutting time while machining RFP AISI1045 steel (mask not scaled in the horizontal direction).

Additionally, the smaller friction coefficient of TiCN compared to Al_2O_3 can increasingly contribute to reduce the maximum temperature. This trend was observed on both HRP and RFP steels (Figures 12 and 13).

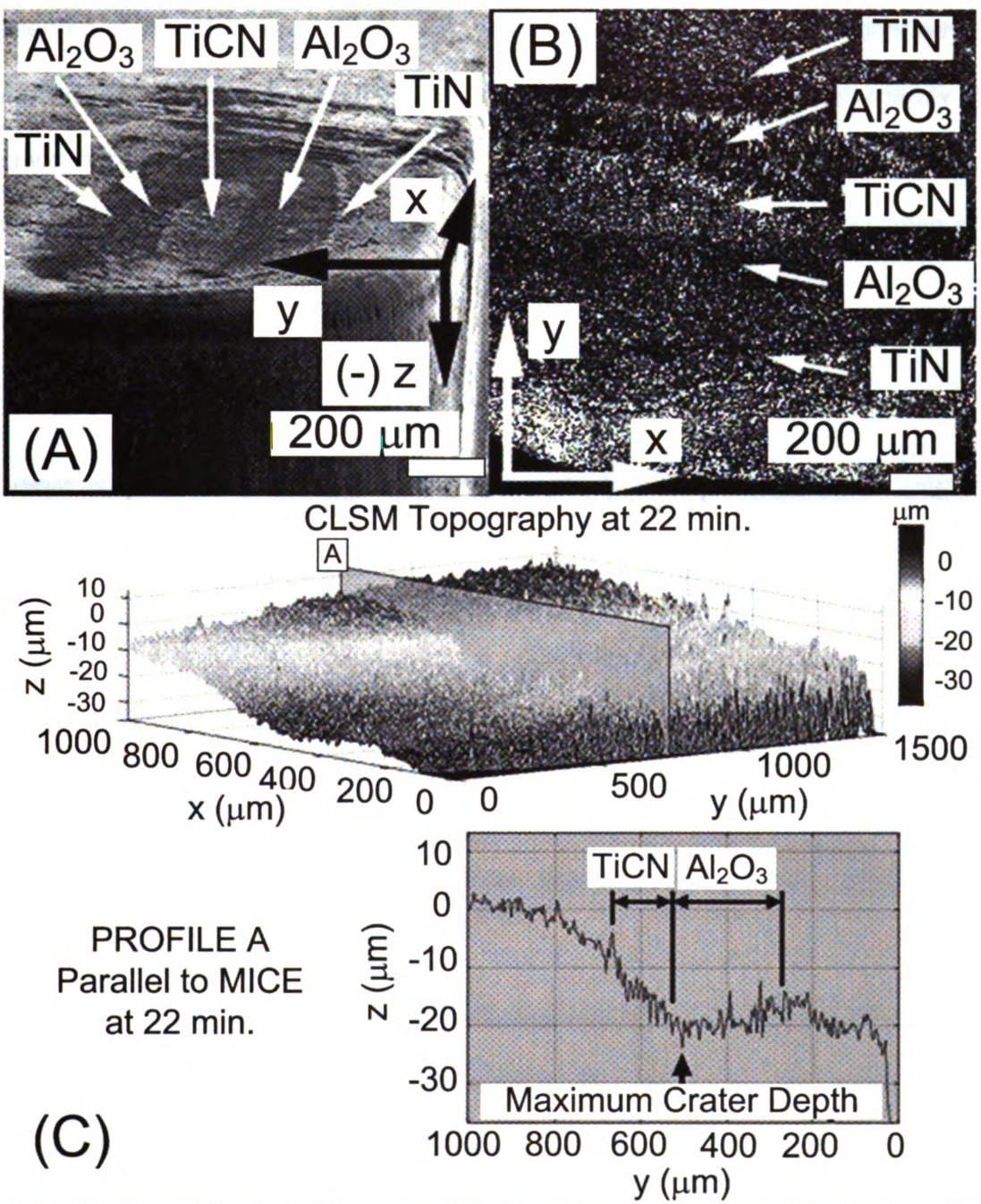

Figure 14 (A) SEM view of corner with 22 min. cutting time (B) Optical view for the 22 min. corner (C) CLSM topography of (B).

After 22 min, when the exposed area of TiCN becomes substantially larger, crater wear accelerated. This was expected as TiCN is known to fulfill the role of diffusion barrier for Co into Al_2O_3 (Su et al., 2002). Finally, when WC is exposed, the solubility of WC is even higher than TiCN. This trend was clearly observed in the RFP steel (Figure 13), which represents more aggressive wear rates compare to Figure 12 (HRP). Microstructures by themselves are clearly the reason behind; therefore, the microstructures of both steels were obtained along with their Vickers hardness. Figures 15-(A) and (B) show the microstructures of both HRP and RFP steels.

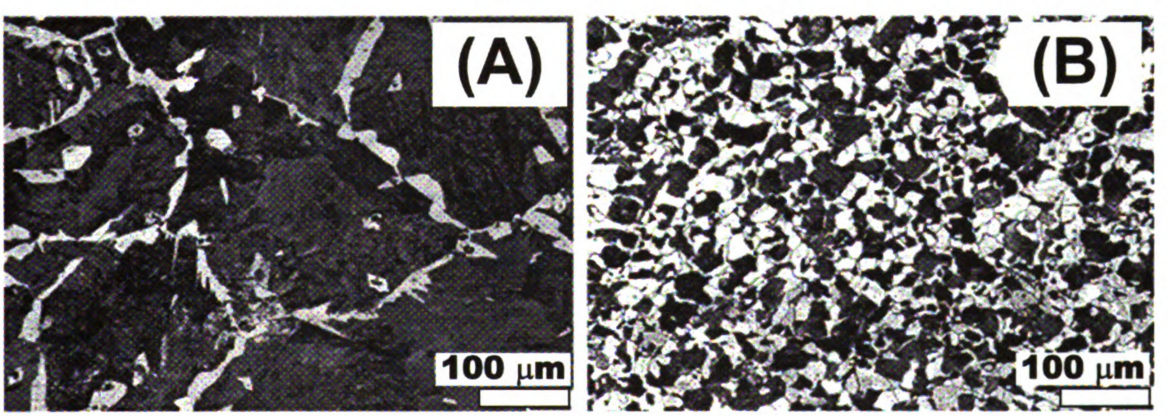

Figure 15 Microstructures of (A) HRP AISI 1045 and (B) RFP AISI 1045 steels

To bring more light into the role of microstructures during machining micro-photographs near the newly -machined surface of the workpiece were obtained and are shown in Figures 16 and 17. These figures present the deformation angle of the grains near the machined surface. It is observed that the

level of deformation is considerably higher (low angles) and uniform in the case of the RFP microstructure due to the greater presence of ferrite (white phase) compared to the hot-rolled case. This could explain the difference in flank wear behavior in the sense that larger deformation leads to higher temperatures which in turn enhance high-temperature wear mechanisms. Although this deformation behavior can directly explain the differences in tool flank wear, the same idea can be used for crater wear due to the plastic deformation nature in the shear zone and chip-tool interface.

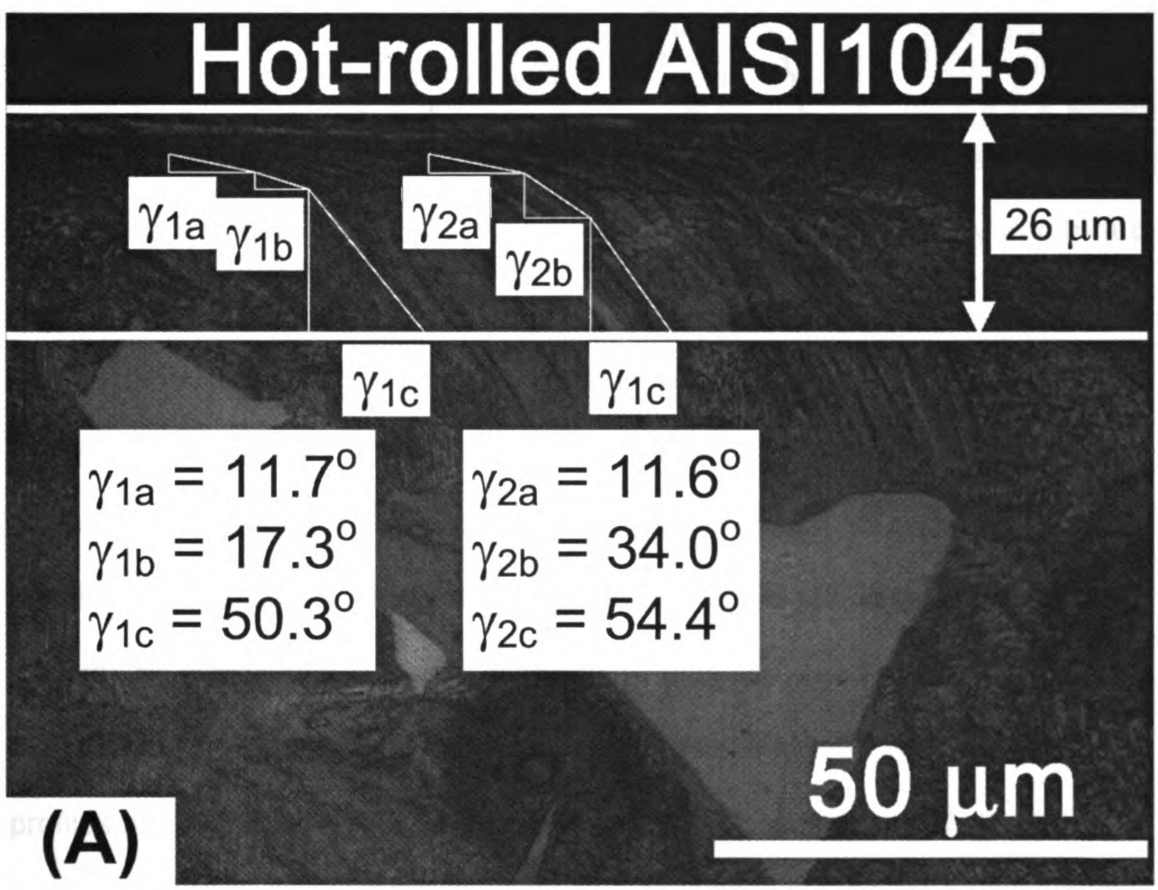

Figure 16 Microstructure of the HRP AISI 1045 steel at the newly machined surface showing the deformation of the grains.

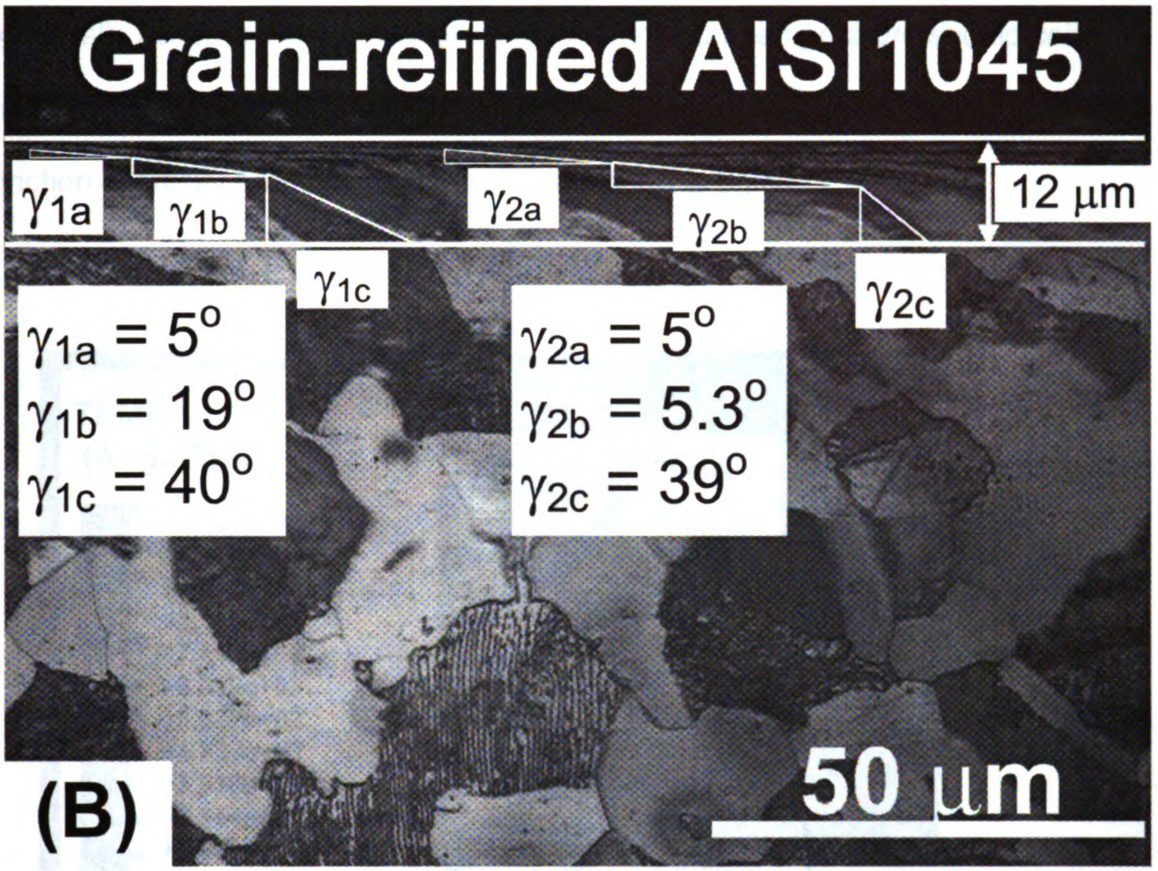

Figure 17 Microstructure of the RFP AISI 1045 steel at the newly machined surface showing the deformation of the grains.

The normal stress and the interfacial temperature were obtained from the ALE-FEM simulations (Figure 18). Figures 19 and 20 show the interfacial temperature and normal stress profiles on the rake face as a function of friction coefficient. Interestingly, the contact lengths (which are not predefined) extracted from the FEM simulations shown in Figure 10 matched closely their counterparts in Figure 12 for μ = 0.25 and μ =0.4, and in Figure 13 for μ =0.5 and μ =0.75. The profiles at 1 and 3 min on Figure 12 represent the wear of TiN. The location of maximum crater wear is y = 412 μ m for 3 min. The latter matched closely the FEM maximum temperature location for μ =0.25 (y = 405 μ m) (Figure 19). It is

generally accepted that the location of the maximum temperature should coincide with the location of maximum crater depth; therefore, a reasonable average friction coefficient between chip and TiN coating is 0.25.

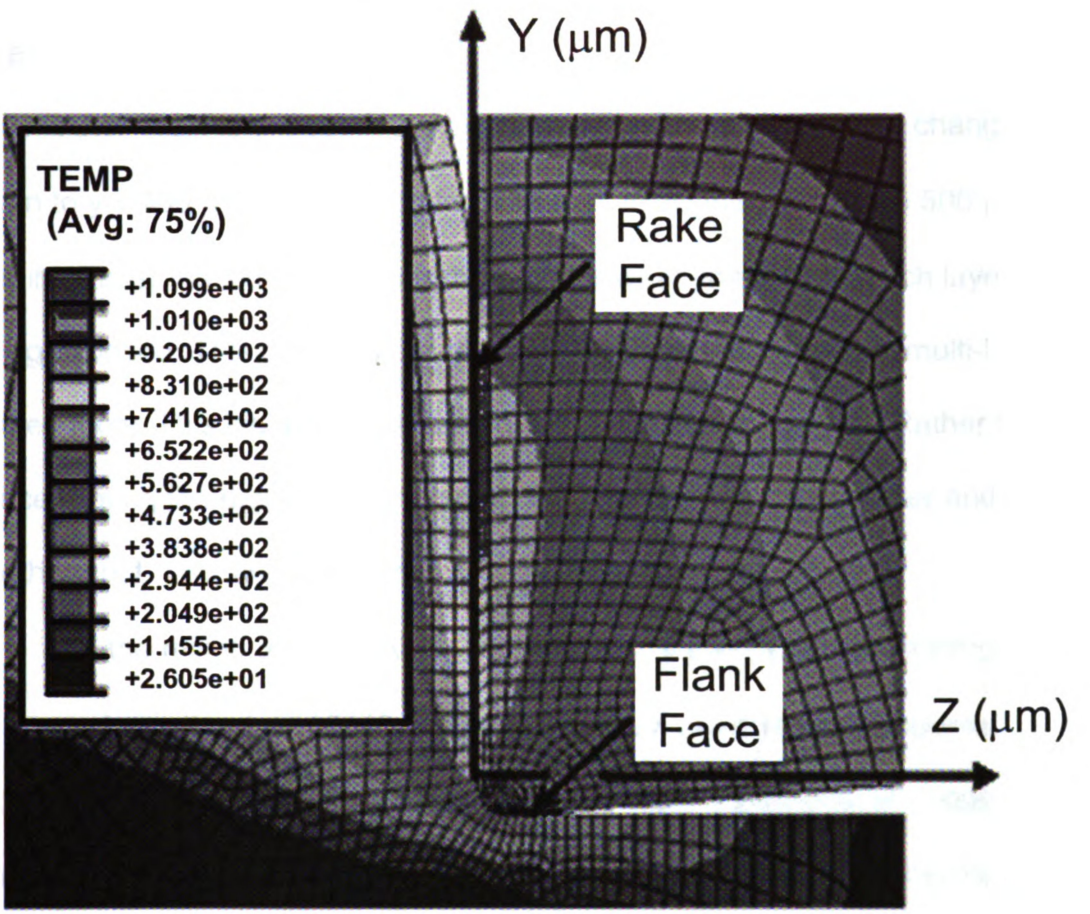

Figure 18 Temperature field at the interfacial region.

The changes in the tool geometry due to wear were not considered in the FEM simulations. In Figures 12 and 13, the origin (y = 0) was chosen to coincide with the tangent point at the cutting edge of the new (unworn) insert. Because of wear, this tangent point moves about 100μm to the right in the profiles beyond 6 min. as shown Figures 12 and 13. Taking this into account, i.e. considering the rake face to start 100 μ m to the right of the y=0, the maximum crater depth is

~500 μ m, which is close to the maximum temperature location provided by the FEM simulation (530 μ m) using μ =0.4 (T_{max}=1043°C). Thus, μ =0.4 is a reasonable estimate for the friction coefficient between the chip and the rake face.

After TiCN is exposed, the location of maximum crater wear changes again to y ≈ 400 μ m when going from 18 min. to 20 min; and to y ≈ 500 μ m for 22min.. Thus, the location of maximum crater wear changes as each layer is being exposed. This provides the rationale for the effectiveness of multi-layer coated tools. This wear trend is analogous to digging the ground. Rather than concentrating the digging on one spot, one digs one spot, move over and digs another spot. This would take much longer and more effort.

As the mixed α-and-κ-Al_2O_3 coatings are heated during machining, the α-to-κ transformation (at 1090°C in 1 atm) has been observed accompanied by an 8% volume decrease (Vuorinen and Karlsson, 1992; Larsson et al., 1999). However, this transformation can also take place below 1090°C under high interfacial pressures (Larsson, 2000 and Ruppi, 2005). With μ =0.4, the interfacial temperature and the contact pressure reached 1043°C and 1GPa, respectively (Figures 19 and 20). Thus, the α-to-κ transformation can occur between 12 to 16 min. deteriorating the wear resistance of Al_2O_3 compared to that between 6 to 8 min. Stuber et al. (1999) claimed that the effectiveness of multi-layer coated tools is due to the improvement in fracture toughness presented by multiple interfaces.

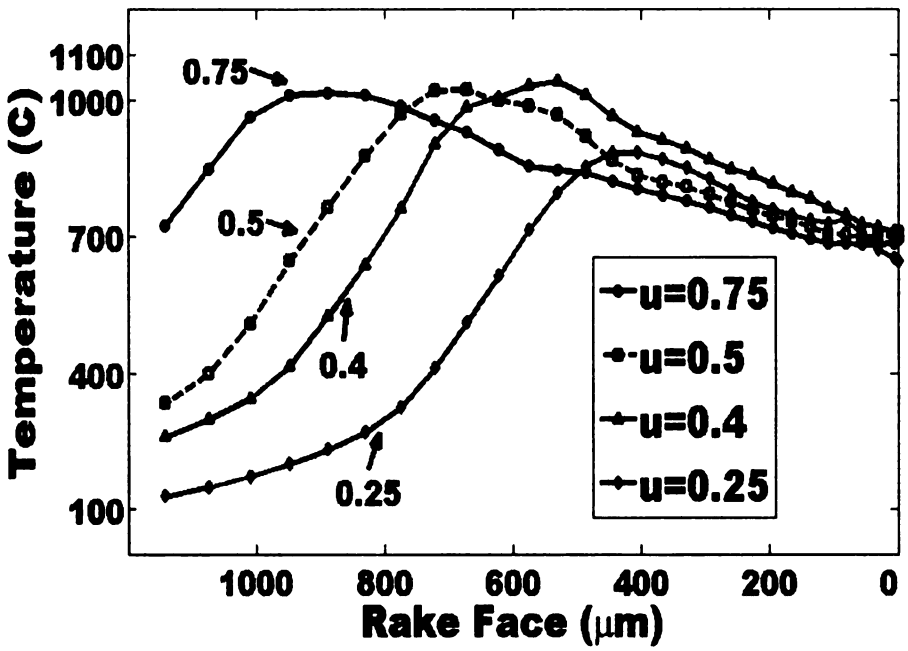

Figure 19 Rake face temperature profiles based on the ALE-FEM simulation.

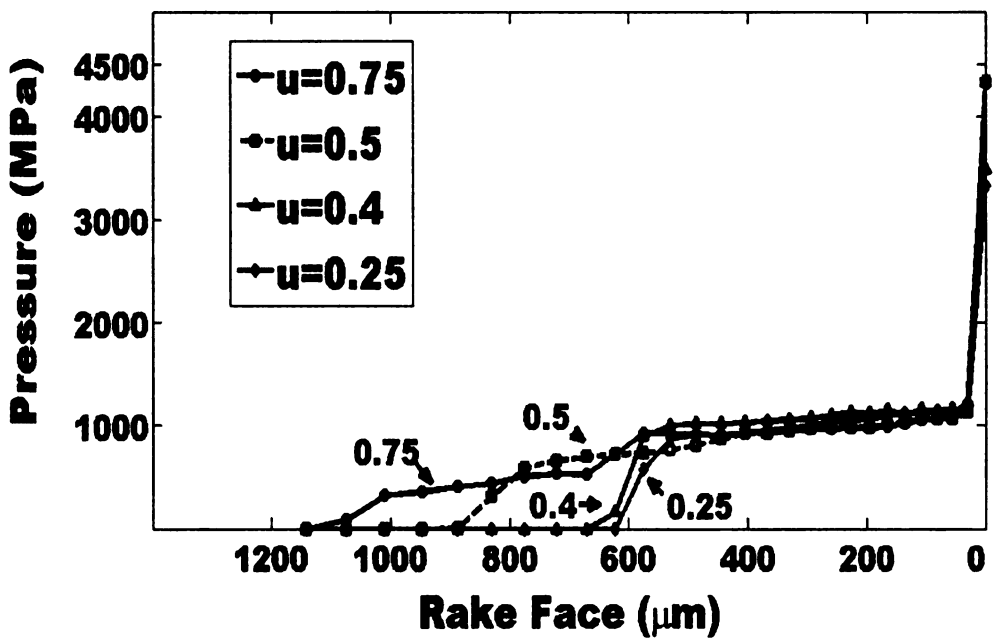

Figure 20 Rake face normal stress distribution based on ALE-FEM simulation.

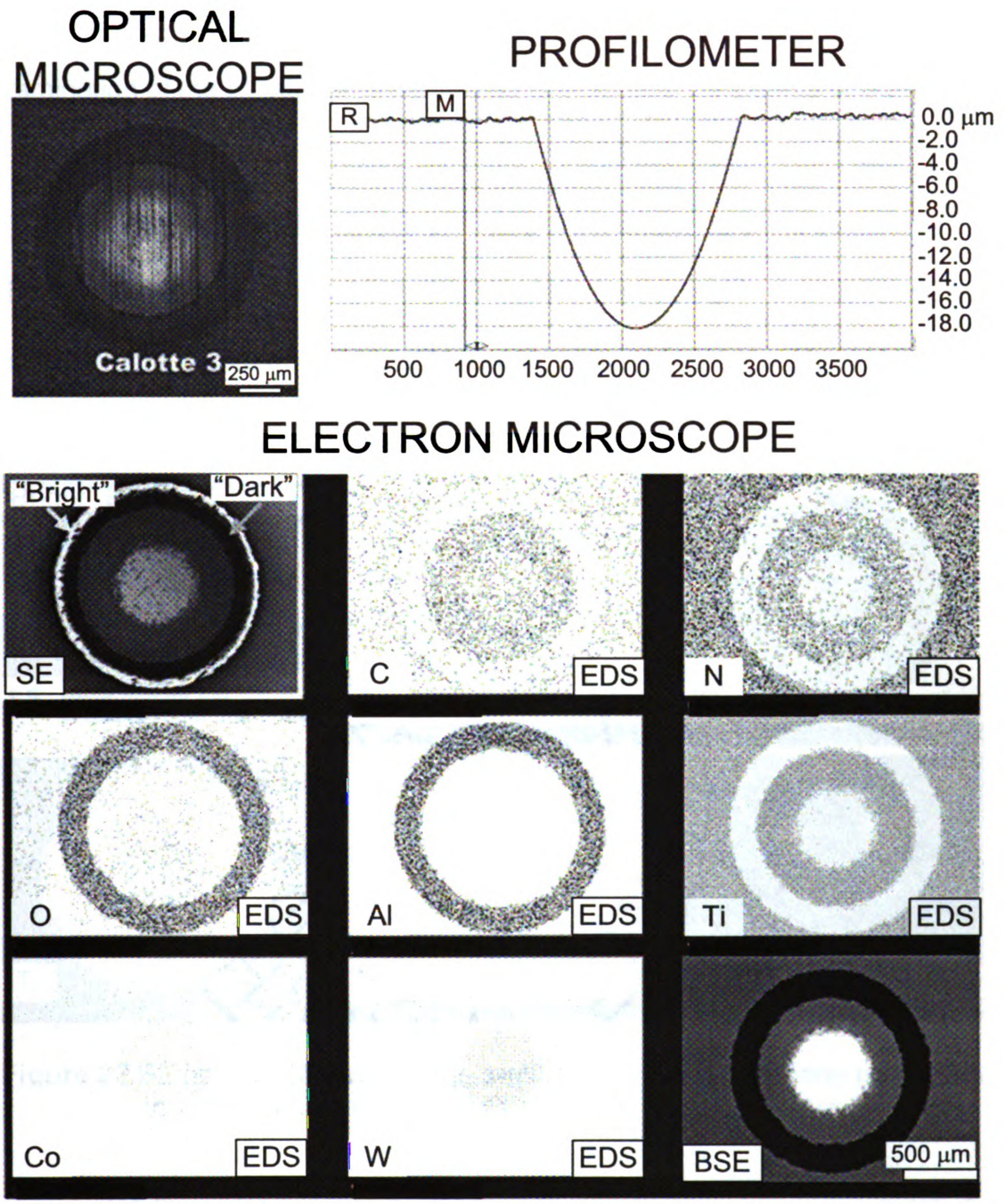

Figure 21 Optical view, profiler reading, SE image, EDS mapping, and BSE, images of calotte 3 in Figure 9-(A).

Even though the original cracks in the Al_2O_3 coating widened due to the volume contraction during the α- to κ- transformation, no delamination or fracture

of the coatings was observed in the present turning experiments. A more detailed examination of the calottes was performed to elucidate the extents of α and κ–Al_2O_3 polymorphs.

Figure 21 shows the calotte in Figure 9-(A) analyzed using the DEKTAK6M profiler, SE electrons, BSE and EDS mapping. In the SE image two distinguishable layers of α ("bright") and κ ("dark") Al_2O_3 can be observed.

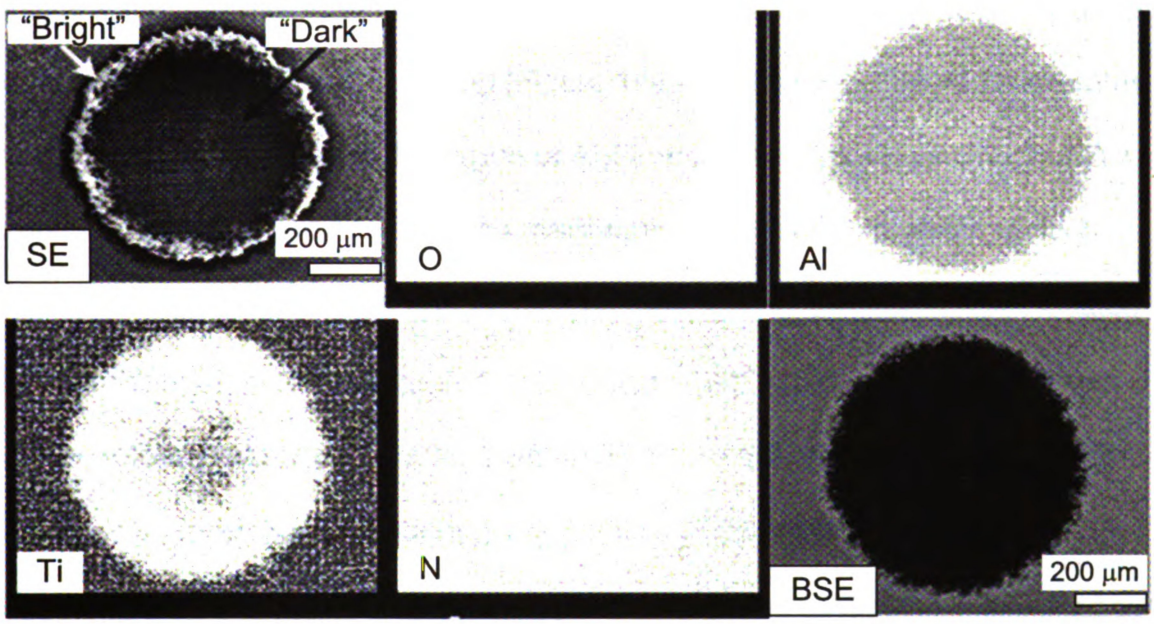

Figure 22 SE image, EDS mapping, and BSE image of a calotte performed in a new insert in old batch of experiments (see Appendix B)

Using the same scheme posed by the calotte method the thicknesses of these layers were calculated to be 3.34 μm and 5.82 μm, respectively. This confirms that the trend observed in the calottes with different grinding times in Figure 9-(B) does not happen by chance. To verify further the presence of these two different layers of α ("bright")and κ ("dark") Al_2O_3 a fresh insert from the batch

in Appendix B was observed using SE, BSE imaging and EDS mapping. The results showed that indeed these two layers exist in this insert coming from a different batch; however, the thicknesses by the calotte methods turned out to be 1.40 μm and 3.61 μm, respectively.

As mentioned earlier, the profiles in Figures 12 and 13 infer creep plastic deformation of the carbide substrate. The BSE pictures shown in Figure 11 indicate that the region within the 400 μm from the MACE consists of TiN. This is evident even until 22 min of cutting (Figure 14-(A)). However, Figure 12 indicates that this zone should be in the region of Al_2O_3 at 22 min. It is concluded that this zone is plastically displaced and the maximum deformation can reach up to 4 μm. In addition, between 16 and 22 min the maximum crater depth is not located in the middle of the TiCN-exposed zone (Figure 14-(C)) as it could be expected if a non-deforming tool is assumed. Neither Fe nor W peaks were detected by EDS between the positions y= 600μm and y=700μm (Figure 12) but debris were observed after y=950μm. Thus, it is inferred that surface bulging had occurred in the surface coatings (up to 3μm) at the trailing edge as evident in Figure 12. The amount of deformation of the cutting (4 μm) trailing (3 μm) edge could be easily neglected if not for the fact that we are dealing with very thin wear resistant coatings. The cutting edge lowering and the surface bulging at the trailing edge explain the slanted location of the exposed TiCN area in Figure 14.

2.4 SUMMARY OF EXPERIMENTAL WORK

The following conclusions can be drawn based on the experimental evidence:

- The Al_2O_3 coating is the main contributor to the crater wear resistance of TiN-Al_2O_3-TiCN coated carbide.
- The effectiveness of multi-layer coated tools comes from the fact that the location of maximum crater wear progresses into multiple locations as each layer is being exposed.
- The microstructures of HRP and RFP AISI 1045 steels play an important role in crater and flank wear evolution. With smaller grain size and the higher ferrite content (RFP) more grain plastic deformation was observed at the machined surface, which ultimately can be related to more severe tool wear effects via larger amounts of heat generation.
- The Al_2O_3 coating was conclusively found to be composed by the metastable κ-Al_2O_3 and the stable α-Al_2O_3 polymorphs.
- Due to the high temperatures and pressures at the rake face verified with ALE-FEM simulations, the κ- Al_2O_3 to α-Al_2O_3 transformation is believed to occur at the Al_2O_3 coating during machining.
- Creep plastic deformation at the cutting and trailing edge makes gradual tool wear analysis much more complex as relative positions can change with cutting time.

Chapter 3

CRATER WEAR PATTERNS USING THE WAVELET TRANSFORM

Several works have been performed to obtain crater wear patterns using 3D measurement equipment. 3D Stereo Microscopy (Karthik et al., 1997) has been applied to measure crater wear volumes; however, due to its inherent coarse resolution (~100μm transversal and ~125μm axial), surface micro-features were impossible to capture. To obtain the evolution of crater wear volume in single-layer coated carbides, curve-fitting rendering of data coming from 3D stylus profilers (Francoso de Avila et al., 2006) has been also used. Nevertheless a coarse mesh is inevitably observed in a meso-scale frame (1.6mm x 1.6mm) and any filtering details are not provided. A recent assessment of crater topography (Wang et al., 2006) utilized phase-shift profilometry to obtain full-field 3D data sets of the crater on coated tools. The topographic data was filtered but the achievable vertical accuracy (5-18μm) impairs the analysis of micro-mechanisms on the surface. The crater wear of uncoated carbides has been also observed using interferometry (Devillez et al., 2004) and analyzed by z-thresholding algorithms to identify meso-scale crater patterns. In spite of its outstanding vertical resolution (0.1nm), no information was reported regarding to short-wavelength features (roughness) which can be used for the analysis of micro-mechanisms of wear. In other work (Dawson and Kurfess, 2005), interferometry 3D data sets were compared with 3D CAD models of new tools to determine the wear of uncoated and ceramic-coated polycrystalline cubic boron nitride. However, as surface-fitting was used, the details on surface roughness

were not captured. In Appendix B the successful CLSM application in tool wear analysis to obtain the crater wear evolution in multilayer-coated carbides is shown in detail. A transversal resolution of 5 μm and a 50 nm vertical accuracy was achieved without any sample preparation. Yet, the topographic data was only filtered by truncating unusual spikes and pits using a custom-built running average filter.

The advent of wavelets provided a breakthrough in the field of signal analysis in the 1990's. In several applications, wavelets analysis has proven more powerful than traditional filtering techniques such as those based on Fourier analysis (Maksumov et al., 2004; Yoon and Chin, 2005; Zeng et al., 2005). A key feature of wavelets resides in their ability to decompose a signal into an effective frequency-time space representation which allows us to localize events in time. In the case of surface analysis, the final product of a wavelet transform is the representation of a surface in a scale-position space which provides a mean to identify the surface changes locally, i.e., the surface is broken-down into its large-scale and small-scale components at a local level. If the wavelet transform is subsequently applied to the surface topography data for an arbitrary number of times, a multi-scale representation of the surface is obtained, i.e., the surface is broken into a spectrum of scales on every location. Similar to Fourier analysis, the wavelet transform represents the original surface in terms of coefficients. With the coefficients in hand and based on what is known about the surface, it is possible to separate different characteristics of the surface and filter noise and artifacts.

3.1 BACKGROUND

3.1.1 Wavelets theory overview

The heart of the wavelets method is to analyze the data according to scale (Hubbard, 1998). To do so, an analyzing function or mother wavelet is used. A mother wavelet can be seen as function capable of stretching or shrinking in amplitude, as well as shifting in position. When the mother wavelet is convoluted with the surface information from measurement instruments, details at different scales are decoupled. In order to record the surface gross features, the scaling function derived from the wavelet function is used. When the convolution is applied for all possible scales and positions, it is named a Continuous Wavelet Transform (CWT). The CWT becomes a Discrete Wavelet Transform (DWT) if the scales and positions used are dictated by dyadic scaling. The efficient implementation of the DWT is generally achieved by the Fast Wavelet Transform (FWT) based on Mallat's algorithm (Mallat, 1989). Contrary to the CWT and DWT, where the wavelet or its discretized version are used explicitly, in Mallat's approach filters derived from the wavelet function are utilized. Finally, the FWT is applied iteratively, i.e. apply the transform to the original data and re-apply the transform to the filtered data and so on. This is known as the multi-resolution analysis which provides a multi-scale representation of the original surface useful to analyze the surface features. In Appendix C, a more in depth review of wavelets theory is provided.

3.1.2 Stylus Profilometry (SP)

Stylus Profilometry (SP) is one of the most widely used techniques to evaluate crater tool wear. In fact, the standards for tool wear characterization are based on its usage. In SP, a diamond stylus in contact with the surface of interest is moved laterally for a specified distance and with a specified contact force while the detection system registers vertical displacements. The vertical accuracies can reach the nanometer range. One main advantage of SP is that it is not prone to optical artifacts as the stylus directly touches the surface. Some disadvantages include the slow scanning rate, the fragility of the tip, and the dependence of horizontal resolution in the stylus tip and wear state.

3.2 WAVELET ANALYSIS PROCEDURE

The general approach in this work was to apply the wavelets Multi-Resolution Analysis (MRA) approach to investigate at which level of decomposition the decoupling of large-scale (form) features from the small-scale ones (roughness) occurs without compromising the crater patterns. Both 1-D and 2-D MRA wavelet analysis were used to decouple large-scale from small-scale surface features. 1-D wavelet analysis was applied to the crater profiles from the DEKTAK6M while 2-D wavelet analysis was used in the case of data coming from the LSM210.

Once this has been achieved, the approximation coefficients (cAj) of the optimal level are used to reconstruct the approximation surface (A_N) via Inverse

Wavelet Transform (IWT). Similarly, the detail coefficients in the horizontal (cHj), vertical (cVj), and diagonal directions (cDj) can be used to reconstruct the details (Hj, Vj,Dj) decoupled at every level of decomposition. For the 1-D wavelet case, de-noising was not needed as the DEKTAK6M software setup takes care of it to a large extent. A 1-D wavelet processing program was written in MATLAB for 9 levels of decomposition. Another key issue in the MRA approach is the selection of the appropriate mother wavelet for the particular application (Bruzzone et al., 2004). The two most common guidelines are that the mother wavelet can generate an orthogonal basis and that the shape of the mother wavelet should resemble as closely as possible to the features on the surface (Bruzzone et al., 2004). This, of course, is difficult to implement and the trial-and-error method is acceptable in the absence of other criteria for mother wavelet selection (Bruzzone et al., 2004). After several trials with SymletN, BiorthogonalN, DaubechiesN mother wavelets, it was found that Daubechies20 ('db20') was the best for de-noising and small-large feature separation which is in agreement with previous works (Yuan et al., 2005; Josso et al., 2002)

3.2.1 Wavelet Analysis Implementation

To keep clear the implementation of wavelets analysis to crater wear patterns, the following profiles and surface data correspond solely to the tip of a multilayer-coated carbide (SNMA 190612-ISO / KC9315) used to cut AISI1045 steel for 8 minutes in Appendix B.

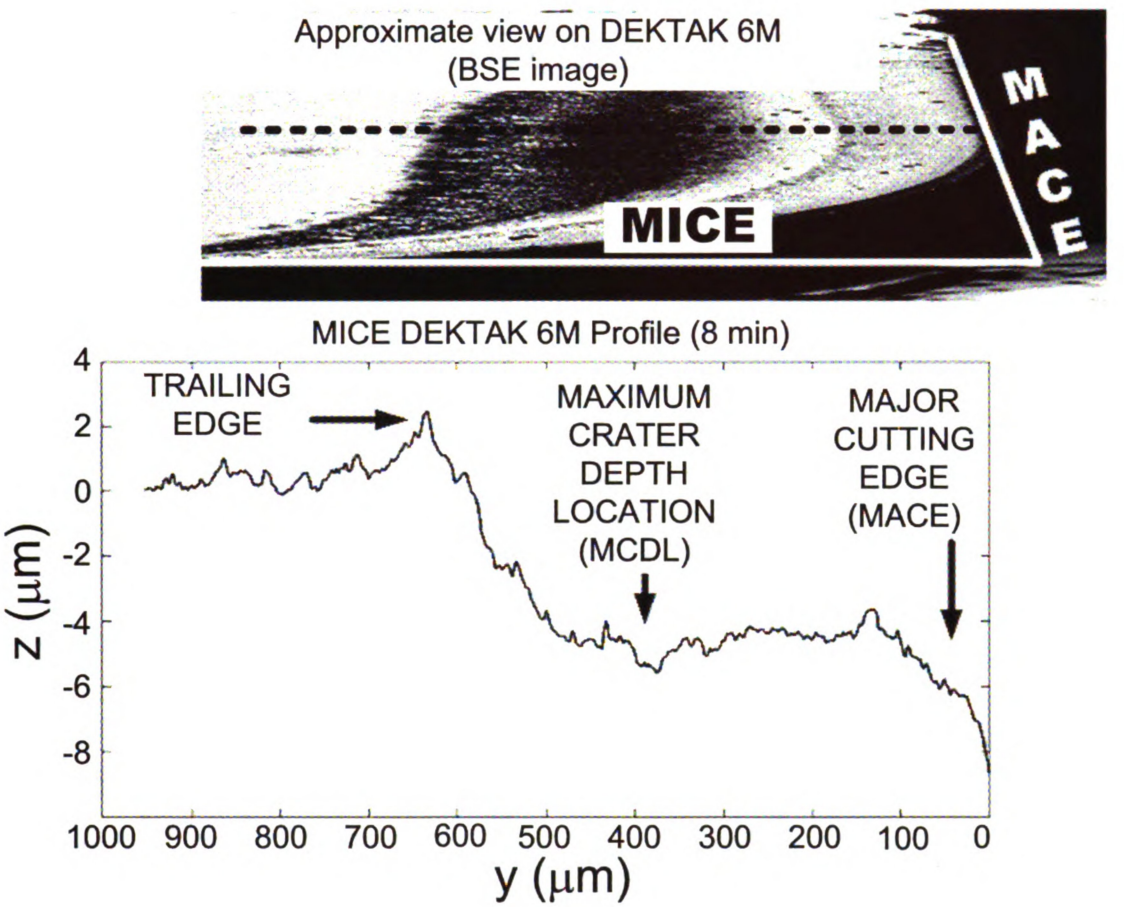

Figure 23 DEKTAK6M crater profile at 8 min. cutting time parallel to MICE

In Figure 23, the crater profile data acquired using a Veeco DEKTAK6M profiler parallel to the Minor Cutting Edge (MICE) at 8 min is shown. The acquisition parameters the scan length, scan duration, contact force, short-pass filter, and long-pass filter were 4800μm, 200s, 3mg, 800μm, and 800μm, respectively. The stylus profiler had a tip radius of 12.5μm. A Backscattered electrons (BSE) image of the rake face is also provided for labeling and clarification purposes.

The topography data of the worn craters was acquired using a Zeiss LSM210 Laser Scanning Microscope. The step size, the total number of optical slices, and the objective used during acquisition were 250nm, 200, and Zeiss10X/0.30, respectively.

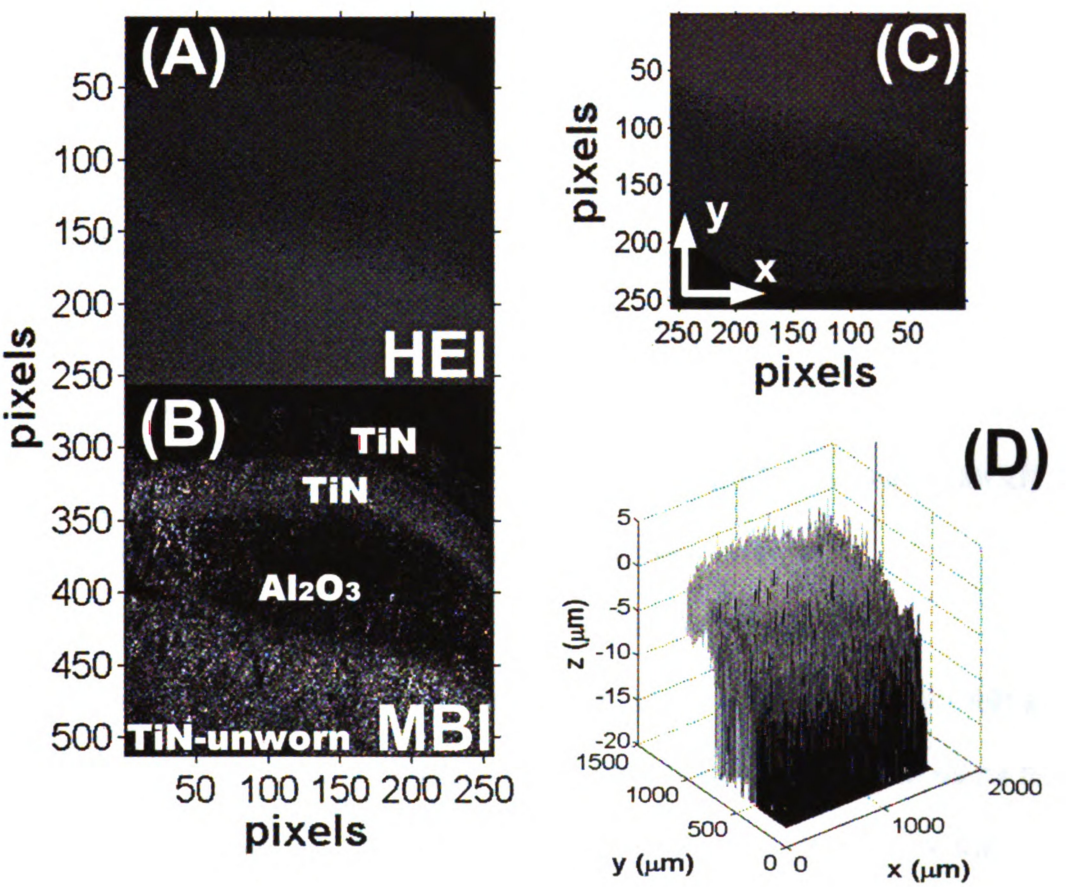

Figure 24 CLSM (A) HEI, (B), MBI, (C) cropped and flipped HEI, (D) raw Z-MATRIX from HEI for 8 min. cutting time.

Figures 24-(A) through 24-(C) show the HEI and its MBI counterpart for the crater after 8 min. of cutting time. The MBI image shows Al_2O_3 surrounded by TiN. The position of the surface is shown in the HEI where bright pixels indicate

high positions relative to the dark ones. Figure 24-(C) renders the unfiltered or raw HEI of Figure 26-(A). The presence of noise, "spikes" and "pits," is clearly noted.

3.4.1 1-D Wavelet Analysis Results and Discussion

Figure 25 shows the reconstructed approximations and details for levels 1, 3, 5, 7, and 9 of wavelet decomposition of the profile. A smooth curve is obtained without curve-fitting and the main features of the surface remain very well localized respect to the raw profile. Another advantage of this wavelet-filtered surface is that the main characteristics of the crater pattern such as the Maximum Crater Depth Location (MCDL) and Maximum Crater Depth (MCD) are now unambiguously defined according to the wavelet analysis.

In Figures 26 through 28, the original (raw) profile and their approximations reconstructed from the 7th, 8th, and 9th levels (A7, A8, A9) are compared. Level 7 (Figure 26) has a smoothed profile keeping at the same time the shape trend of the original (raw) crater pattern, e.g. the position of the cutting and trailing edge. A8 in Figure 27 loose the exact position of the trailing edge and small distortions starts to show up in the cutting edge. A9 in Figure 28 not only looses the position of the trailing edge but also does not capture the pit in the center of the crater and the position of the cutting edge.

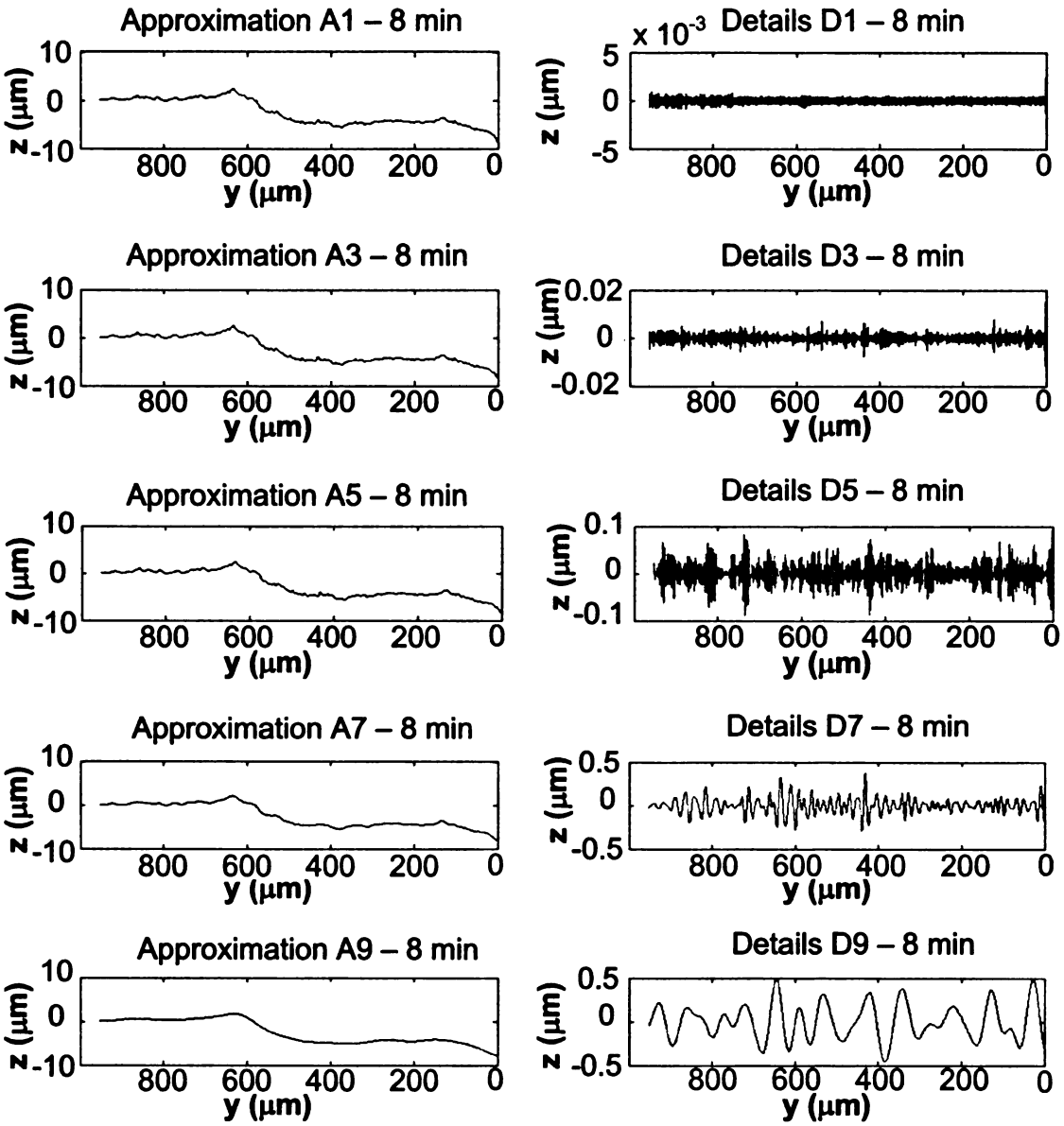

Figure 25 Wavelet Approximations and Details for profile at 8 min. (1st, 3rd, 5th, 7th, and 9th levels)

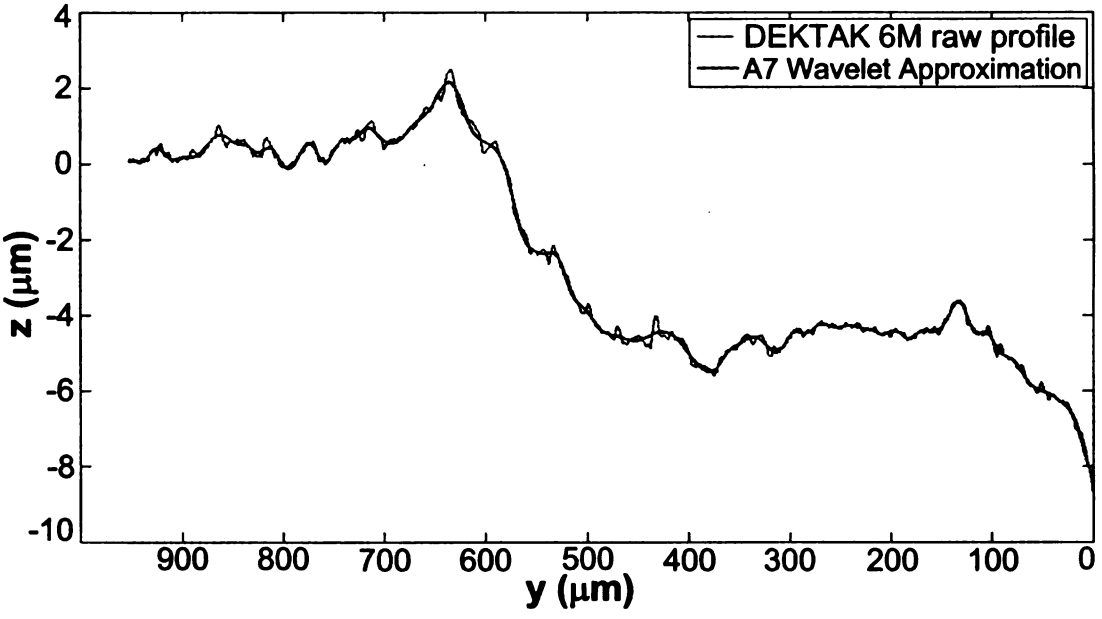

Figure 26 Comparison of original DEKTAK6M profile with its A7 wavelet approximation for 8 min.

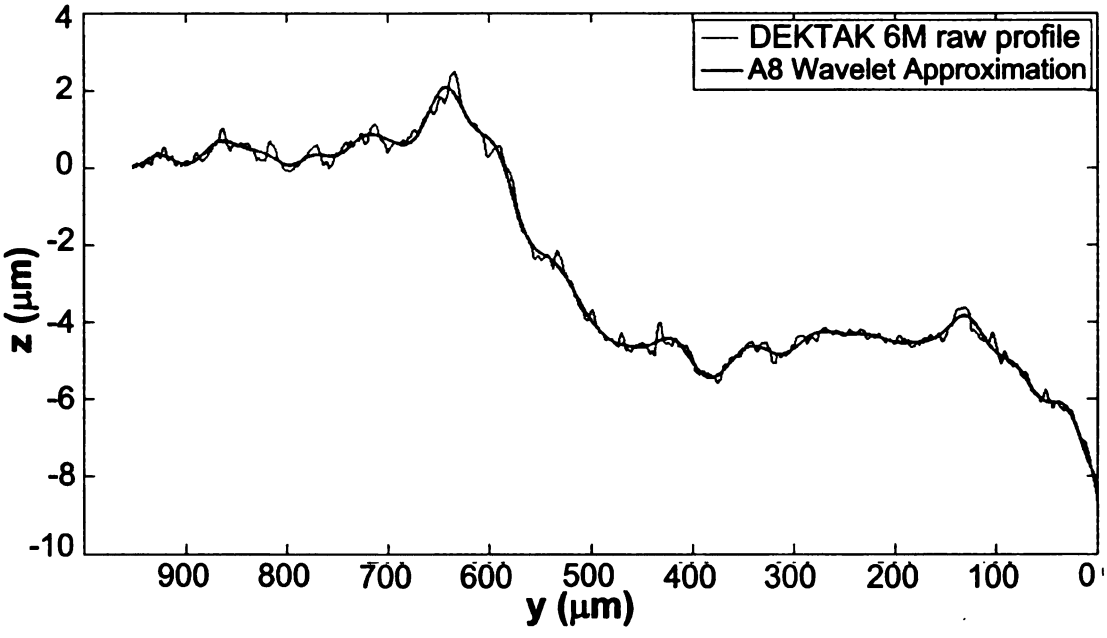

Figure 27 Comparison of original DEKTAK6M profile with its A8 wavelet approximation for 8 min.

Thus, the A7 approximation is picked as the best profile representing the crater wear pattern. A6 (not shown in figures) followed the original, raw profile very closely without filtering out any details.

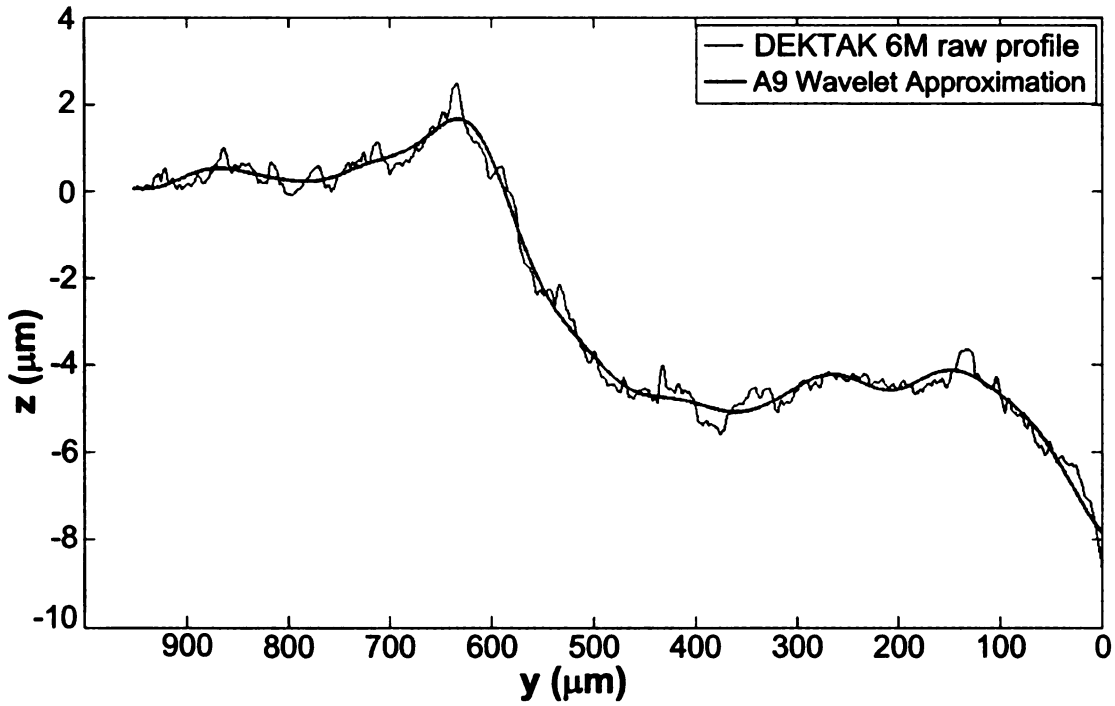

Figure 28 Comparison of original DEKTAK6M profile with its A9 wavelet approximation for 8 min.

3.4.1 2D Wavelet Analysis Results and discussion

With a 2-D version of the MATLAB program, Daubechies20 ('db20') was also observed to provide the best results. However, this time a preliminary wavelet-based de-noising step using db20 was necessary due to the presence of noise, spikes and pits in the CLSM raw data (See Figure 24-(D)). Only 4 levels of decomposition were pursued due to the unacceptable, gradual distortion of the

cutting edge observed after this level of decomposition. The raw CSLM z-matrix and its A1 approximation for 8 min. cutting time are compared in Figure 29. It is remarkably observed that "spikes" and "pits" have been filtered out without losing the general trend in the crater pattern. In Figures 30 and 31, the raw, de-noised, and A1 MICE profiles extracted from the z-matrices are shown. These profiles have been obtained in a nearby position of the DEKTAK6M profile in Figure 23. The crater pattern obtained with the wavelet-filtered CLSM data is resembles closely to that obtained with the DEKTAK6M profiler after filtering.

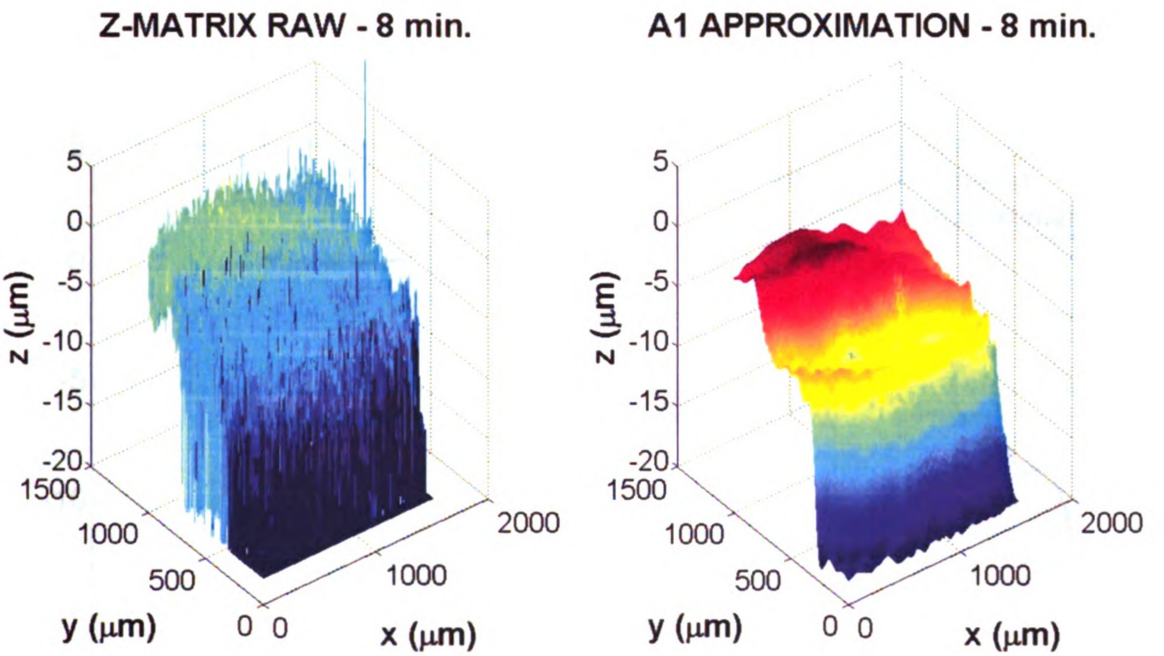

Figure 29 Comparison between the raw CLSM z-matrix and its wavelet de-noised and filtered version at the 1st level of decomposition – 10X objective

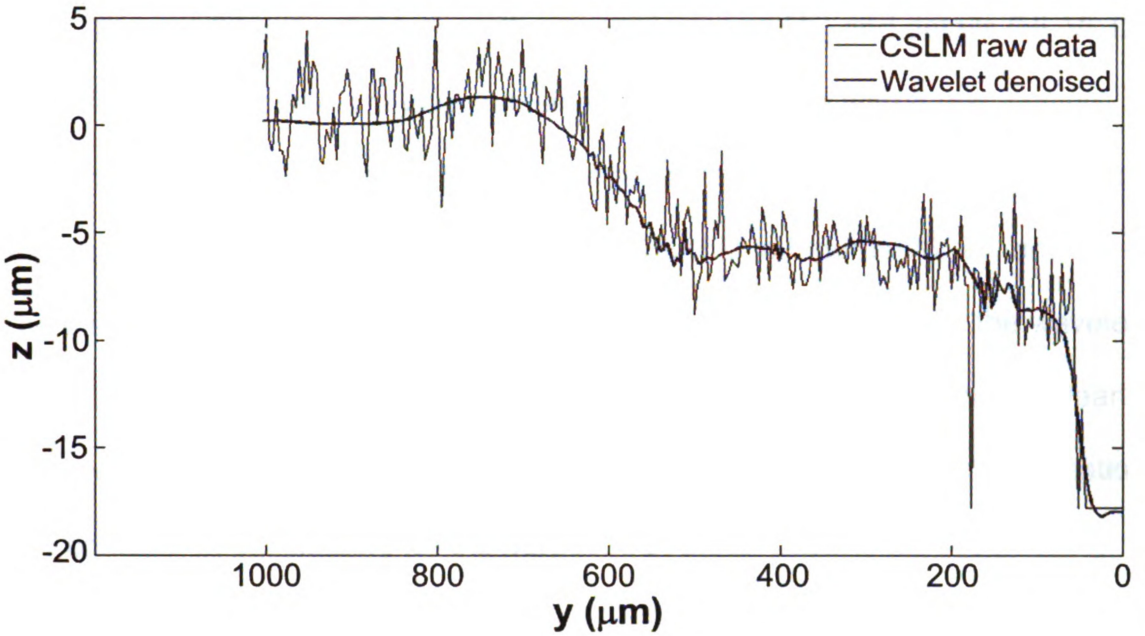

Figure 30 Raw CLSM profile compared to its wavelet-denoised version for 8 min. cutting time

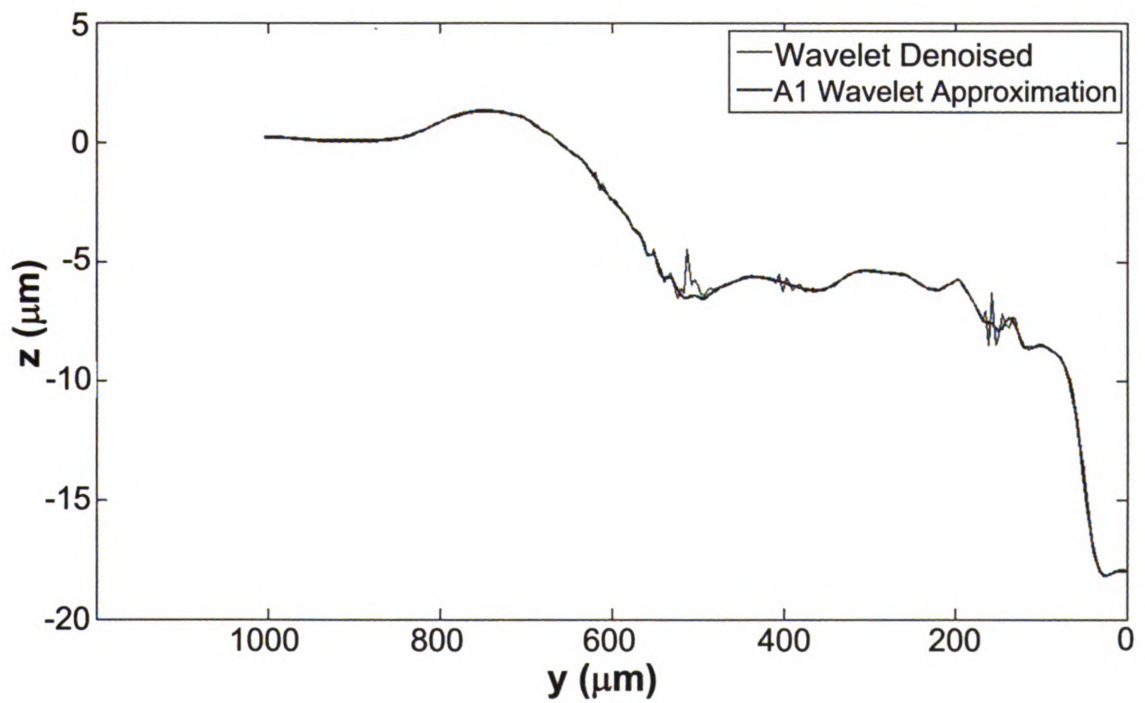

Figure 31 Wavelet-denoised profile compared to its A1 wavelet-filtered version for 8 min. cutting time

Figures 32 through 35 show the approximations (Aj) and details (Hj, Vj, Dj) at the four different levels of decomposition for the z-matrix with 8 min. cutting time. In Figures 32 through 36, the vertical reference has been adjusted to match approximately the reference level of the DEKTAK6M in Figures 26, 27, and 28. The distortion in shape and position of the cutting edge produced by the wavelets analysis increases gradually with the level of decomposition and it can be clearly observed in the "details" pictures in Figure 35. Accordingly, the A1 approximation was considered satisfactory for the purposes of crater pattern extraction using the 10X/0.30 objective.

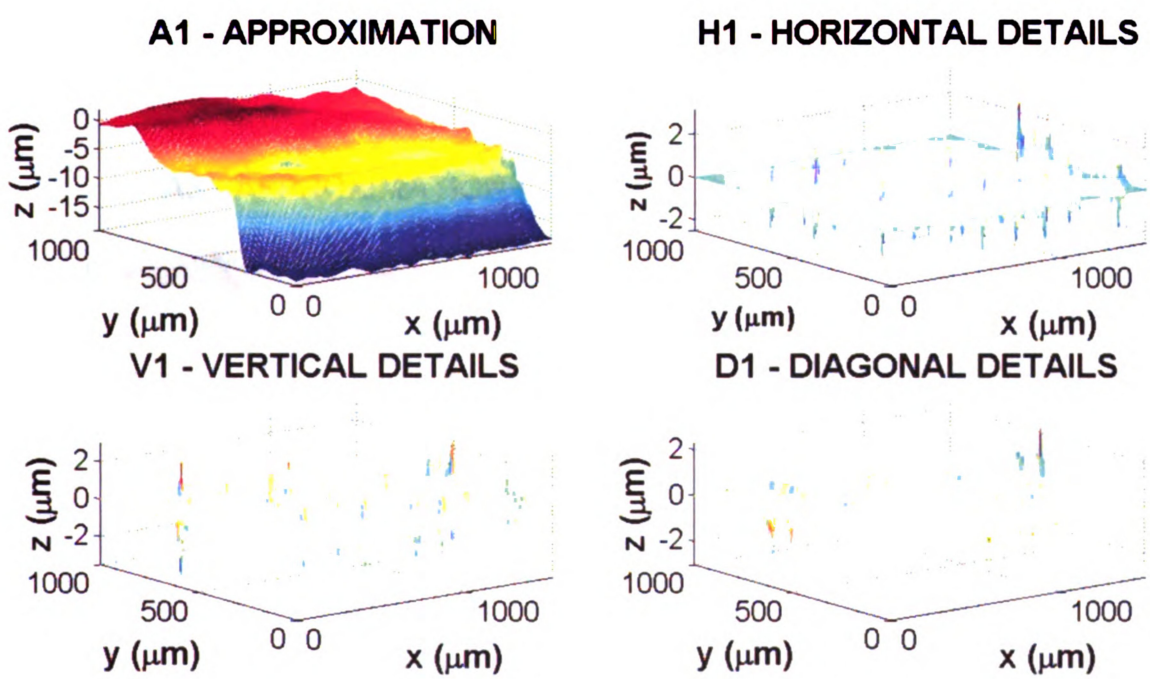

Figure 32 1st Level Approximation and Details for 8 min. cutting time -10X objective

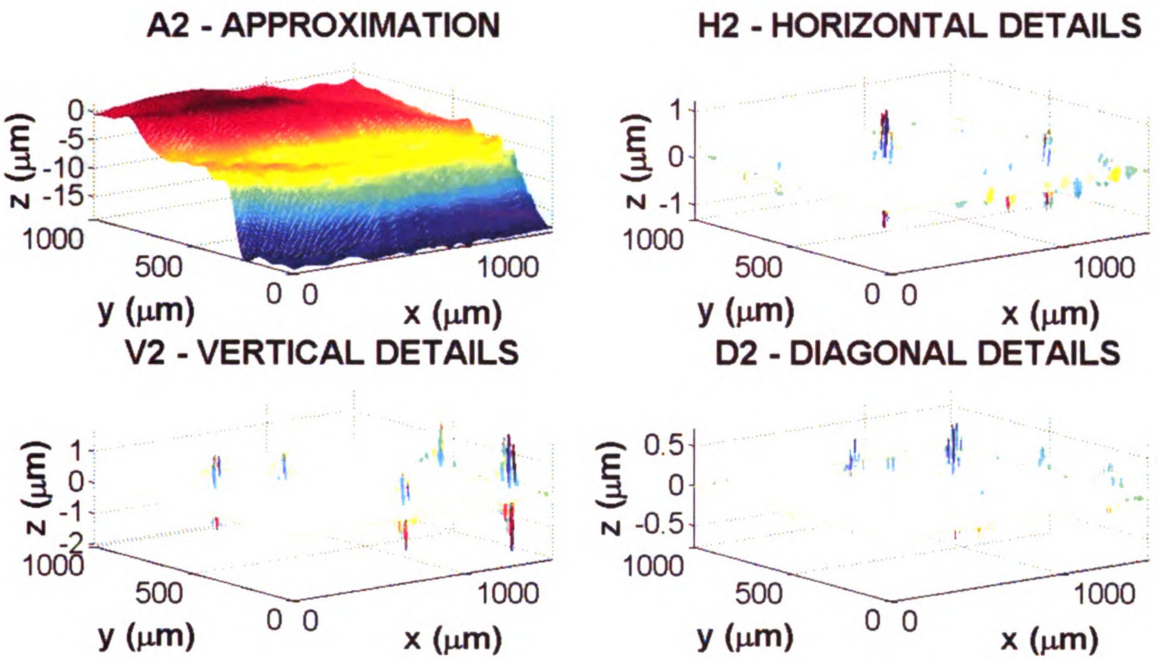

Figure 33 2nd Level Approximation and Details for 8 min. cutting time -10X objective

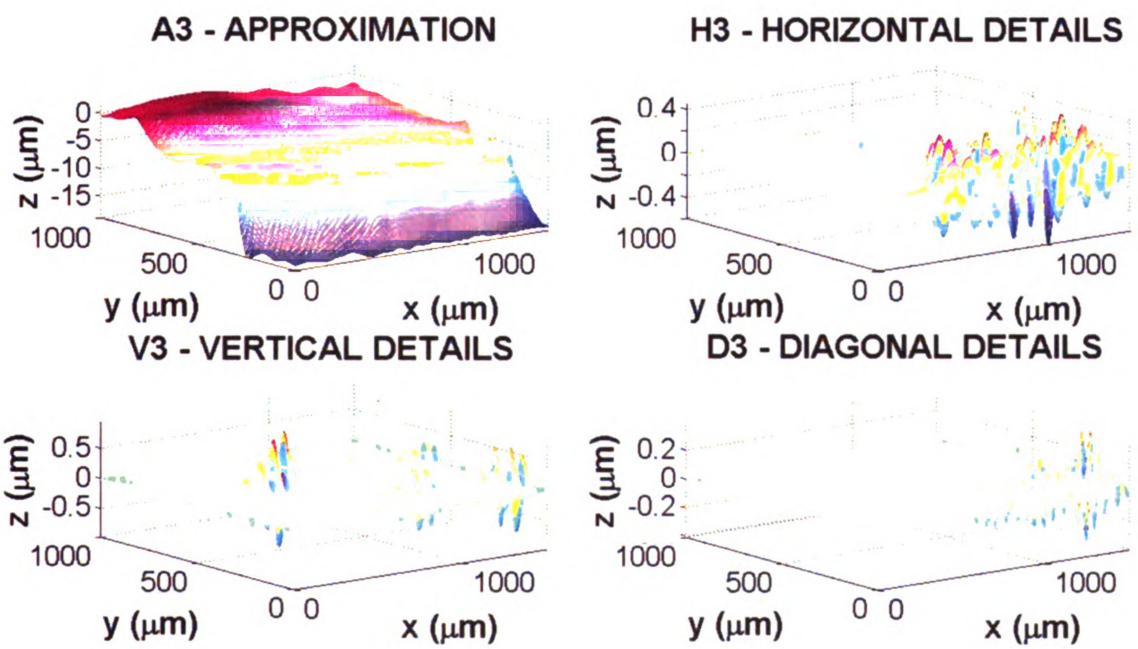

Figure 34 3rd Level Approximation and Details for 8 min. cutting time -10X objective

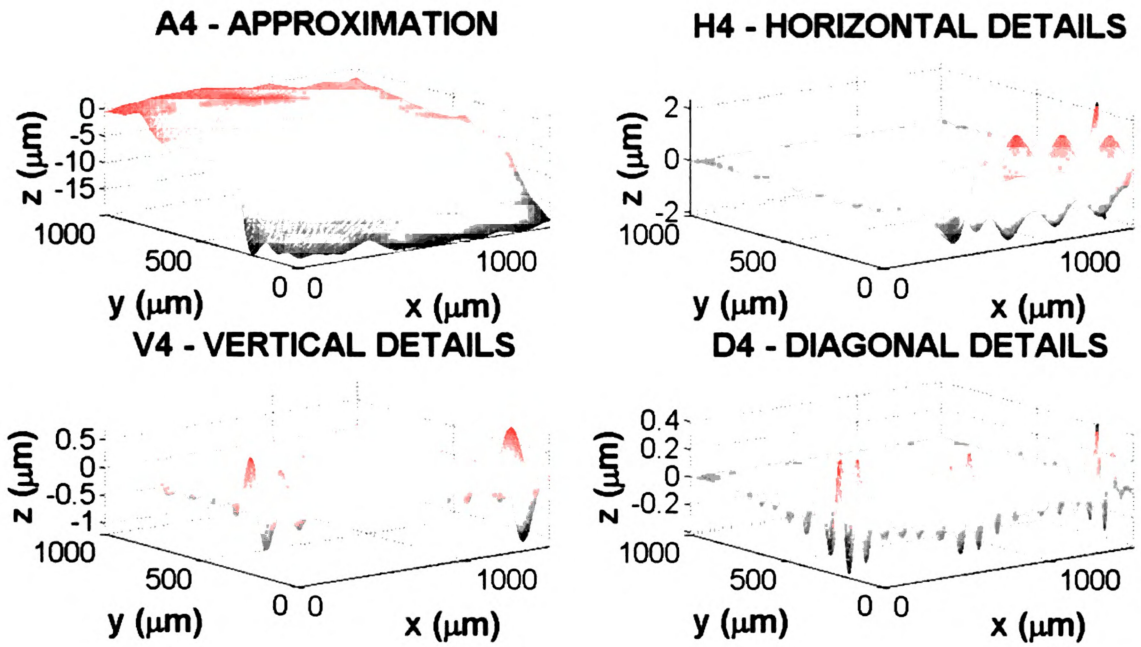

Figure 35 4th Level Approximation and Details for 8 min. cutting time - 10X objective

The evolution in cutting time of the different wavelet-filtered z-matrices up to the 1st level (A1) is shown in Figure 36. This is the time series from which the 8 min. tool tip was extracted (Appendix B). Considering the rake face area, some interesting observations can be made. A very small slope (~ arctan(10 μm/1500 μm) =arctan(Δz/xmax))) can be observed in the unworn (0 min.) insert. This inclination of the surface is not observed in the next (1 min.) and the following z-matrices. These could be explained by the initial deformation of the tool at the initial tool-work engagement and to the gradual deformation of the tip insert. The surface at the trailing edge is also observed to bulge increasingly from 1 min. through 12 min cutting time. Along with trailing-edge bulging, the cutting edge is gradually lowered from its unworn vertical position.

These observations corroborate the findings in Chapter 2 and Appendix B, where only profiles (2D) and unfiltered 3D surface data were available. In the present chapter, using the wavelet-filtered 3D data, it is observed that, for example, debris accumulation alone cannot explain the trailing edge deformation ("bulging"). Though the meso-scale features of the crater are nicely obtained in the A1 approximations in Figure 36, not much information can be extracted from the reconstructed details as observed in Figures 32 through 35. Provided that the CSLM raw data for these figures was captured with a Zeiss10X/0.3 objective, the logical step was to increase the resolution of the objective. Thus, to extract further, more accurate crater patterns and small-features from these patterns a z-matrix was obtained using a Zeiss20X/0.50 objective and a step size of 50 nm for the insert with 8 min. cutting time. Then the 2D wavelet transform program was applied and the results can be observed in Figures 37 through 39. Figure 37 is outstanding as it reveals the details of the crater surface topography not available in the raw CSLM data or even after passing Gaussian low-pass filters available in the LSM210 built-in software. The crater pattern has been extracted (A3) and its top view after rotation is provided as a visual aid. To highlight further the importance of the information obtained through the wavelet analysis, contour lines (isolines) at 15 different height (z) levels are also plotted. Two contiguous spots at the center of the isolines picture become evident indicating the current deepest points where the wear is progressing.

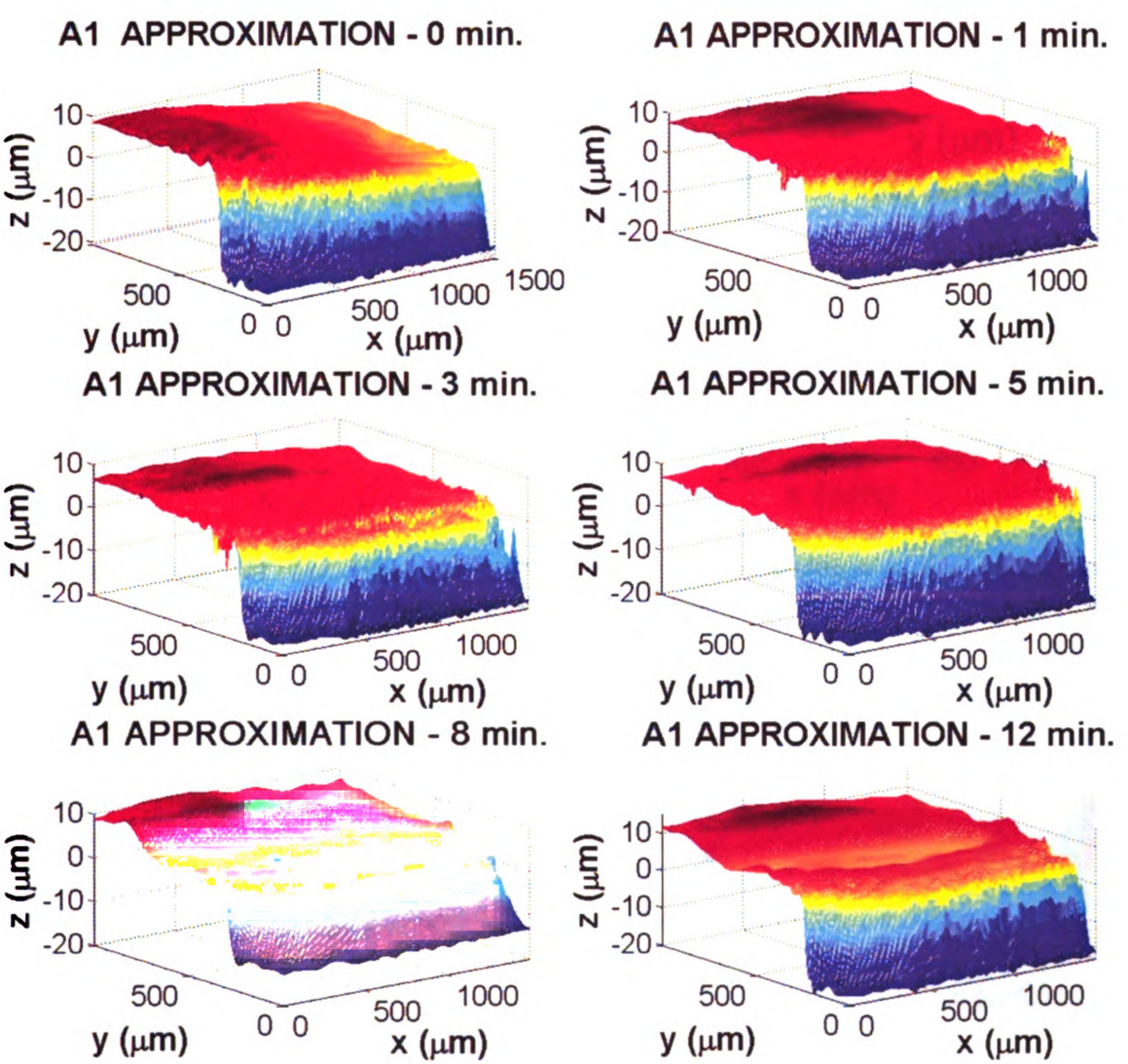

Figure 36 Evolution of crater wear patterns reconstructed from the 1st level of wavelet decomposition (A1 Approximations) – 2nd batch

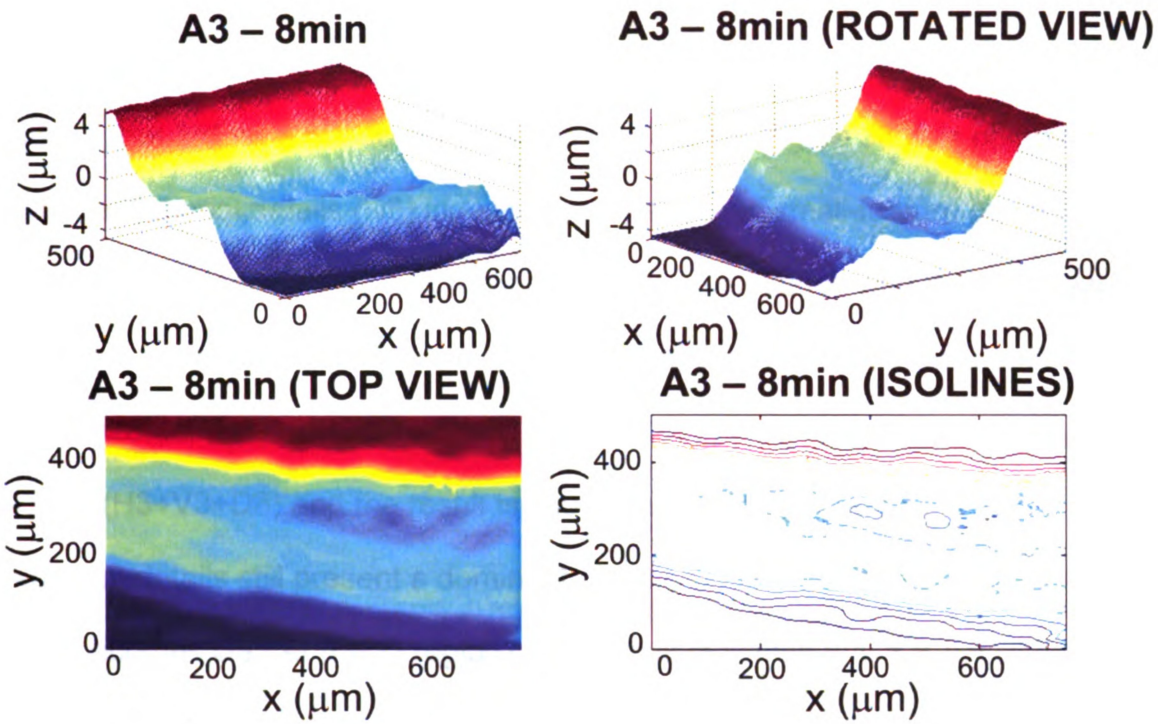

Figure 37 Wavelet reconstruction (A3) of the crater surface at 8 min. cutting time using a 20X/0.5 objective

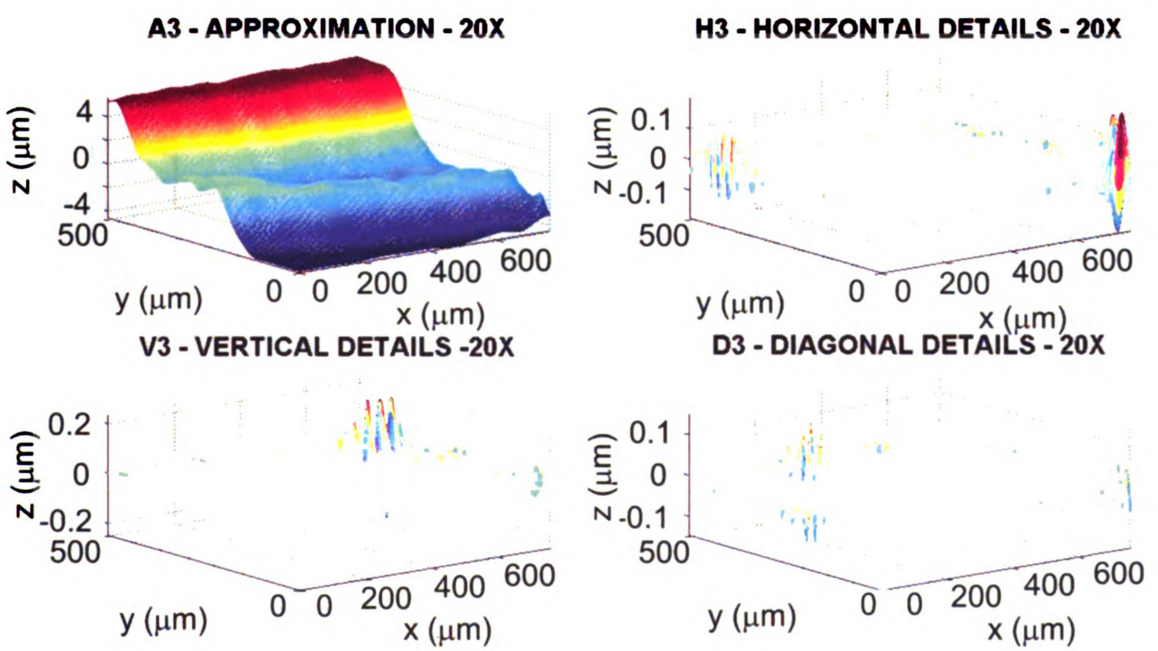

Figure 38 Wavelet Approximation and Details reconstructed from the 3rd level of decomposition - 20X/0.5 objective.

The usage of a higher resolution objective gives the additional advantage of being able to use higher levels of decomposition with meaningful detail data. Indeed, the 3rd level of decomposition is rendered in Figure 38. It is pointed out that the diagonal details (D3) indicate the presence of small-feature patterns having some directionality which could be easily associated with the chip flow direction. In an attempt to have a clearer idea of the extracted details at this level, the horizontal (H3), vertical (V3) and diagonal (D3) details are arithmetically added (H3+V3+D3) and the result is shown in Figure 39. Interestingly, the resultant details still present a dominant direction and their position on the rake face becomes clearer (MCD region). This result indicates that it is possible to capture the localized micro-features of the crater surface.

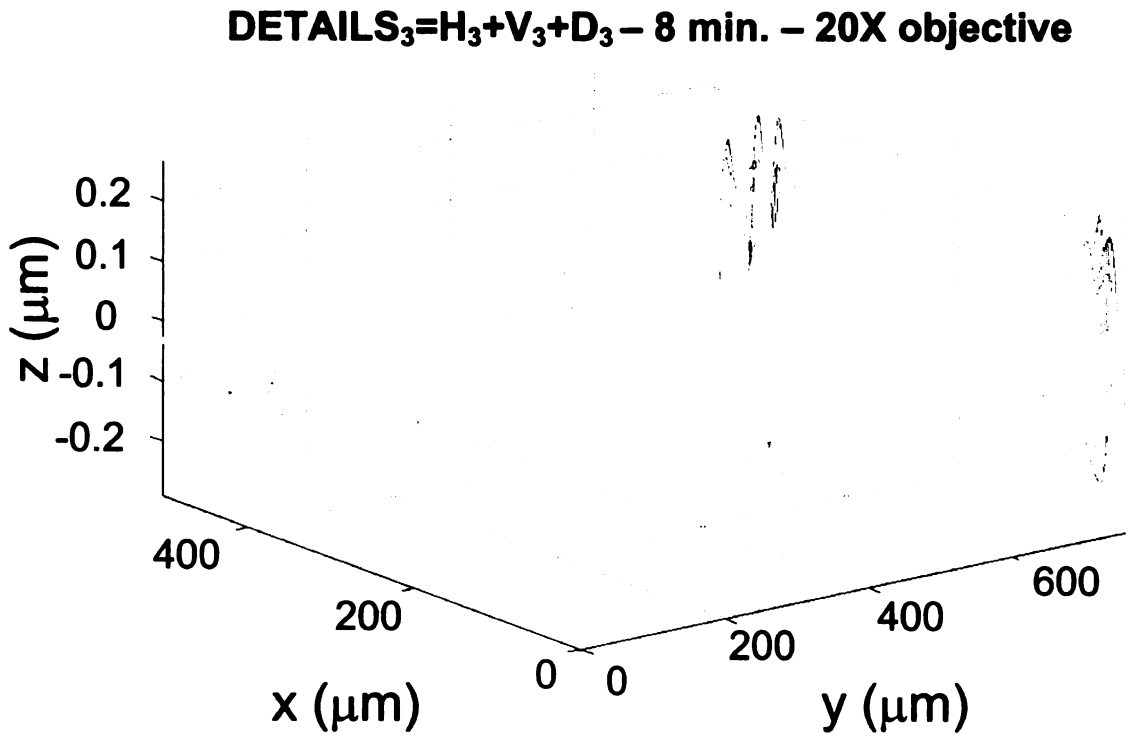

Figure 39 Addition of Details at the 3rd level of decomposition - 20X/0.5 objective.

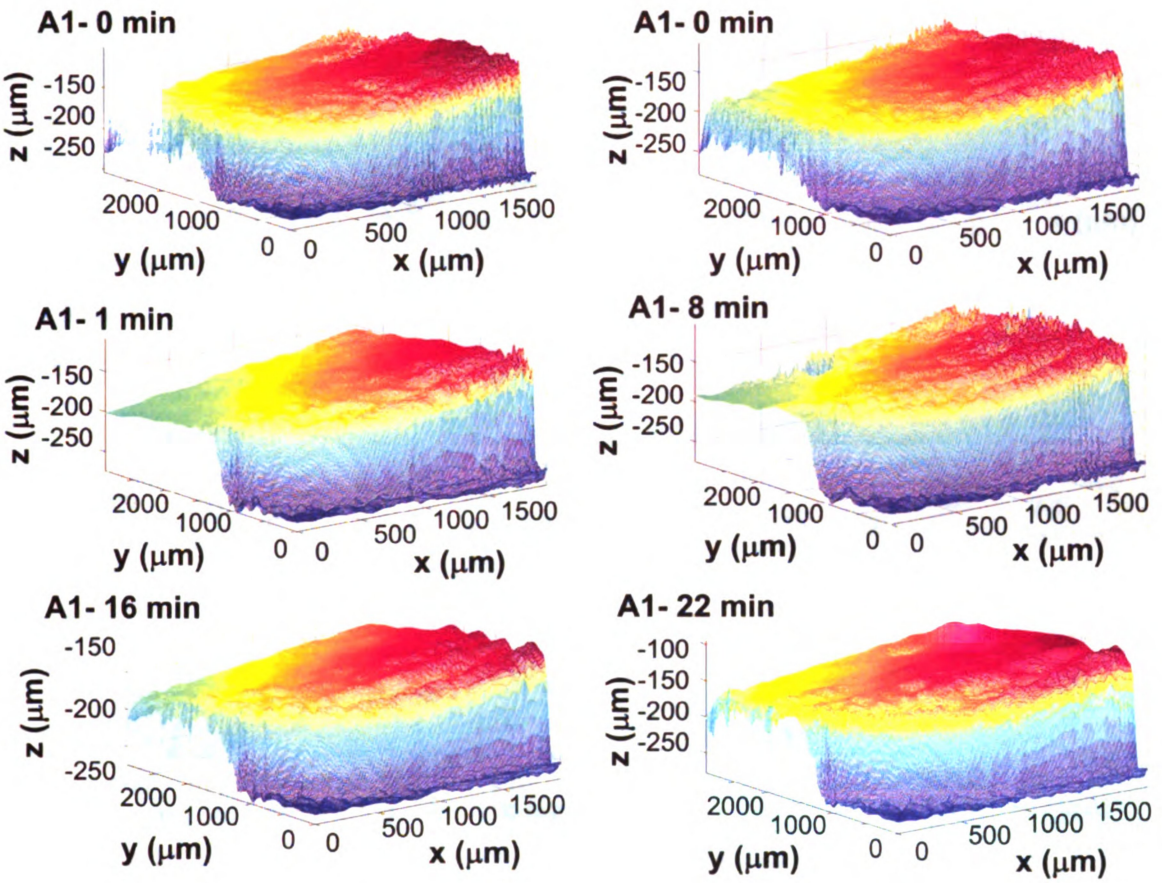

Figure 40 Wear evolution A1-wavelet approximations using 5X/0.30 objective – 2nd batch

The multilayered carbide tools from the second set of turning experiments in Chapter 2 (1, 3, 6, 8, 12, 14, 16, 18, 20, 22 min.) was imaged and wavelet filtered. This time objectives 5X/0.13 and 20X/0.50 were use in attempt to have crater topographies with different scale and different objective resolutions. The results for the 5X/0.13 objective are shown in Figure 40, for the corners with 0 min (NEW), 3 min, 8 min, 16 min, and 22min. Two fresh corners (0 min) of different inserts are plotted in order to confirm the initial topography of the inserts.

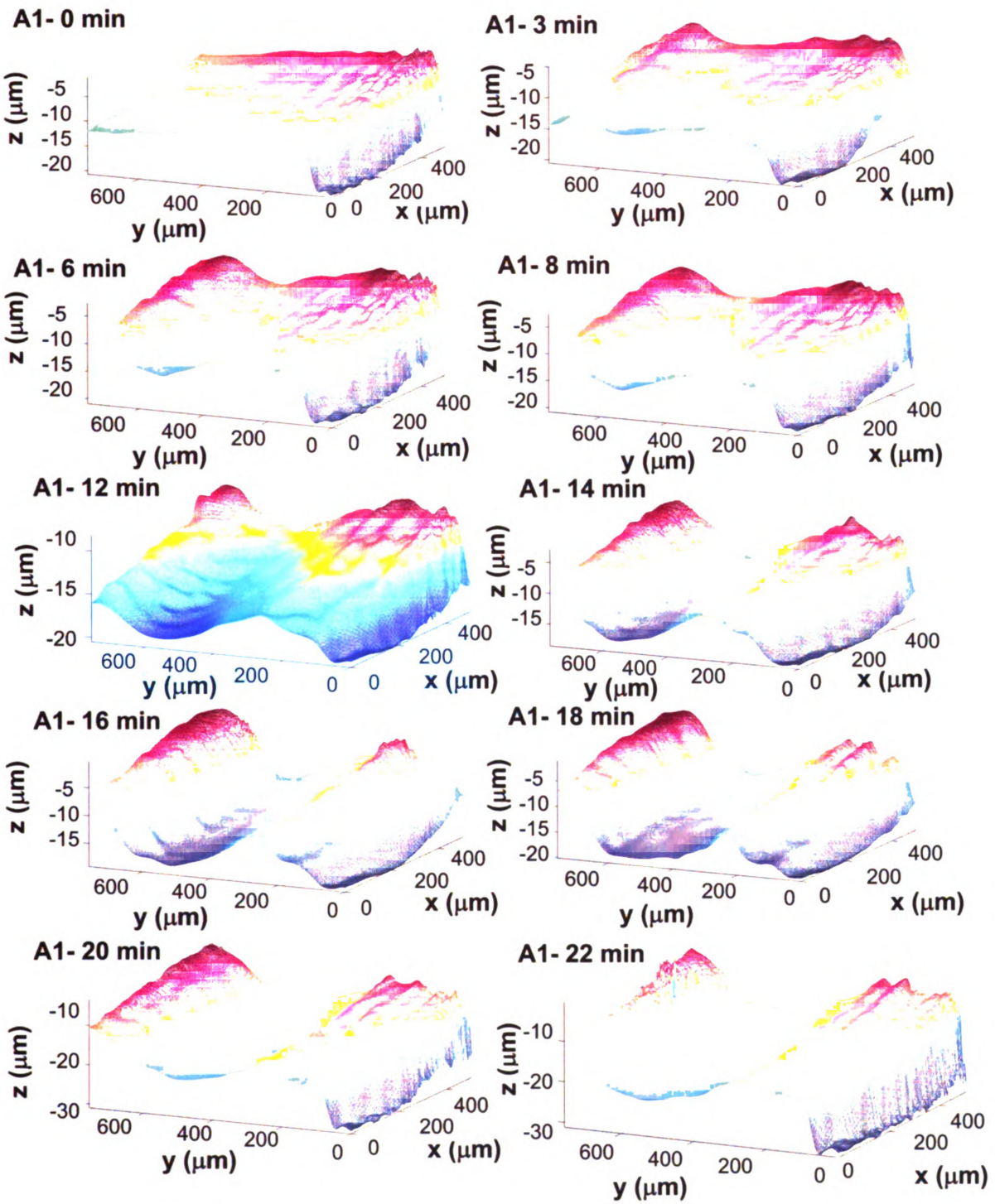

Figure 41 Wear evolution of A1-wavelet approximations - 2nd batch. A1-0min through A1-18min were captured using 200nm step size.A1-20 and A1-22min were captured using a 250 nm step size – 20X objective

Interestingly, it is noted that in this batch the inclination angles have a different orientation respect to the first batch information which cannot be obtained from the manufacturer. The first is a depression angle which can be seen in the plane x-z and an elevation angle which can be seen in the y-z plane. Even using the 10X/0.15 objective the wear evolution can be clearly observed.

In order to get a clearer view of the wear trend, the surface topography for the whole time series was collected using a higher-resolution objective (20X/0.50) near to the region were the rounded edge becomes straight and the results are shown in Figure 41. The clarity of the wear trend after wavelet de-noising and first level approximation (A1) reconstruction is remarkable. From Figure 41, it seems that the location of maximum crater depth moves in the (-)x axis direction as wear progresses through the coating layers. This is the result of changing interfacial friction conditions as different coatings materials are being exposed. Additionally, the bulging of the trailing edge is again noticeable. This adds to the idea proposed in Chapter 2 regarding the wear front digging in different spots as it progresses.

Figure 42 present the separation of a z-matrix into its roughness, waviness, and form components using the 100X/1.30 objective, 50 nm step size and wavelet analysis using 6 levels of decomposition. The z-matrix was captured close to the trailing edge in a worn insert (1 min. cutting time) from the tool batch in Appendix B. The importance of having such decomposition for tool wear analysis resides in the possibility of relating surface parameters with wear micro-mechanisms.

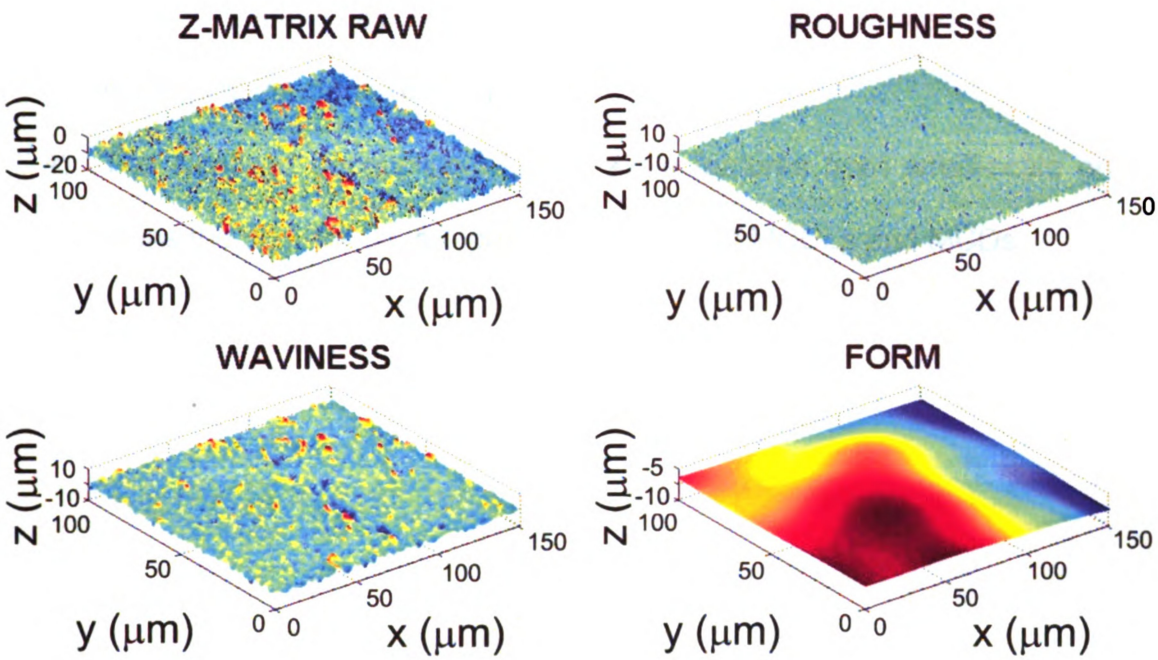

Figure 42 Roughness, waviness and form decomposed extracted using wavelet analysis (100X/1.30 and 50nm step size)

3.3 SUMMARY OF WAVELETS ANALYSIS APPLIED TO WEAR PATTERNS

From the results obtained it is concluded that

1) 1D and 2D wavelets analysis is a very useful tool to study crater micro-and-meso crater wear patterns.
2) The combination of CLSM with the FWT in a multi-resolution approach present a very promising path to study the micro-mechanisms involved in tool wear as roughness, waviness and form can be now correlated separately to surface features.
3) By means of multi-resolution analysis, it is verified that bulging at the trailing edge and deformations at the cutting edge occur simultaneously with tool wear. Also, the changing position of the MCDL as wear exposes

different coating layers was clearly observed and related to changing tribological interfacial conditions.

4) The localized decoupling of large-scale features from small-scale ones opens the door for unambiguous definitions of MCDLs and MCDs.

Chapter 4

LOCAL WEAR PROFILE PREDICTIONS USING PHYSICS-BASED MODELS

This chapter is based on previous findings of our research group regarding fundamental tool wear mechanisms and the findings of the present work. Kwon and Kountanya (1999) in the experimental study involving TiN, Al_2O_3, and TiCN single-layer coated carbides reported that crater wear was fairly well explained by dissolution and abrasion mechanisms. Kim and Kwon (2001) concluded that the existence of a layer of work material detaching periodically from the stagnant zone provides a convective motion at the interface; thus promoting dissolution along with three-body abrasive wear. Wong et al. (2004) showed the experimental support for a comprehensive wear model based on dissolution (Kramer and Suh, 1980) and abrasion (Rabinowicz, 1977) models. In chapters 2 and 3, the high solubility resistance of Al_2O_3, the stacking sequence and the thickness of the coatings have been observed to play a relevant role in the wear evolution of tool wear in multilayer coated carbides. In particular, the solubility resistance of the intermediate layer (Al_2O_3) played an important role in wear retardation.

4.1 MODELLING ASPECTS

The present modeling effort starts by defining the geometry of the tool in a cross section parallel to the Minor Cutting Edge (MICE) and its relationship with the temperature and pressure profiles.

Figure 43-(A) shows the coordinate system used as well as the interfacial temperature ($T(x)$) and pressure ($\sigma(x)$) profiles expected during machining. The origin of the coordinate system starts at the Major Cutting Edge (MACE), which is defined as the point over the rake face where the honed edge starts (Figure 43-(B)). It should be noted that for convenience the "x" axis in this chapter correspond to the "y" axis in Chapters 2, 3 and Appendix B.

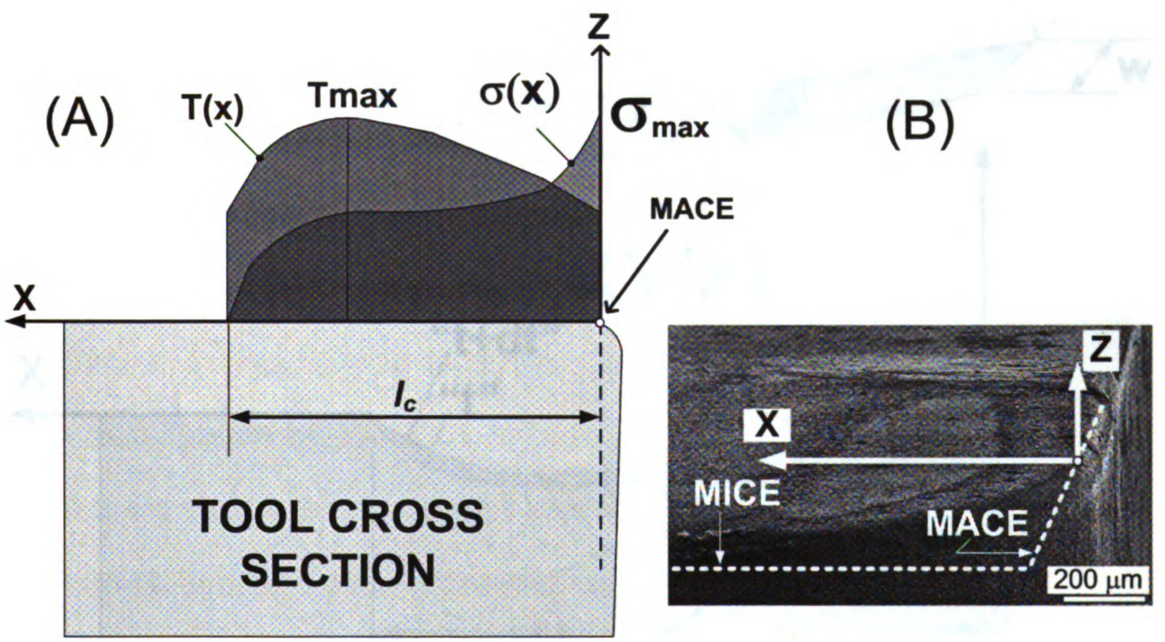

Figure 43 (A) Temperature and pressure profiles (B) Coordinates location in a real insert (50 s cutting time)

In Figure 44, the wearing rake face profile is shown at two different instants "t" and "$t + dt$" in which, l_c is the chip-tool contact length and $dV(x)$ is the differential volume lost by wear at location "x". The width w is used to render a volume in order to fit the definitions of the original abrasion (Rabinowicz, 1977) and dissolution (Kramer and Suh, 1980) models. In practice, w could

receive a meaningful value such as the wear groove width on the rake face or a multiple of it. The crater surface curvature will not be considered due to the small value of the ratio between the maximum crater depth and the contact length (around 0.04 for the biggest experimental crater before failure). Mathematically, this is expressed by $S \approx X$ in Figure 44, where "S" is the actual contact length.

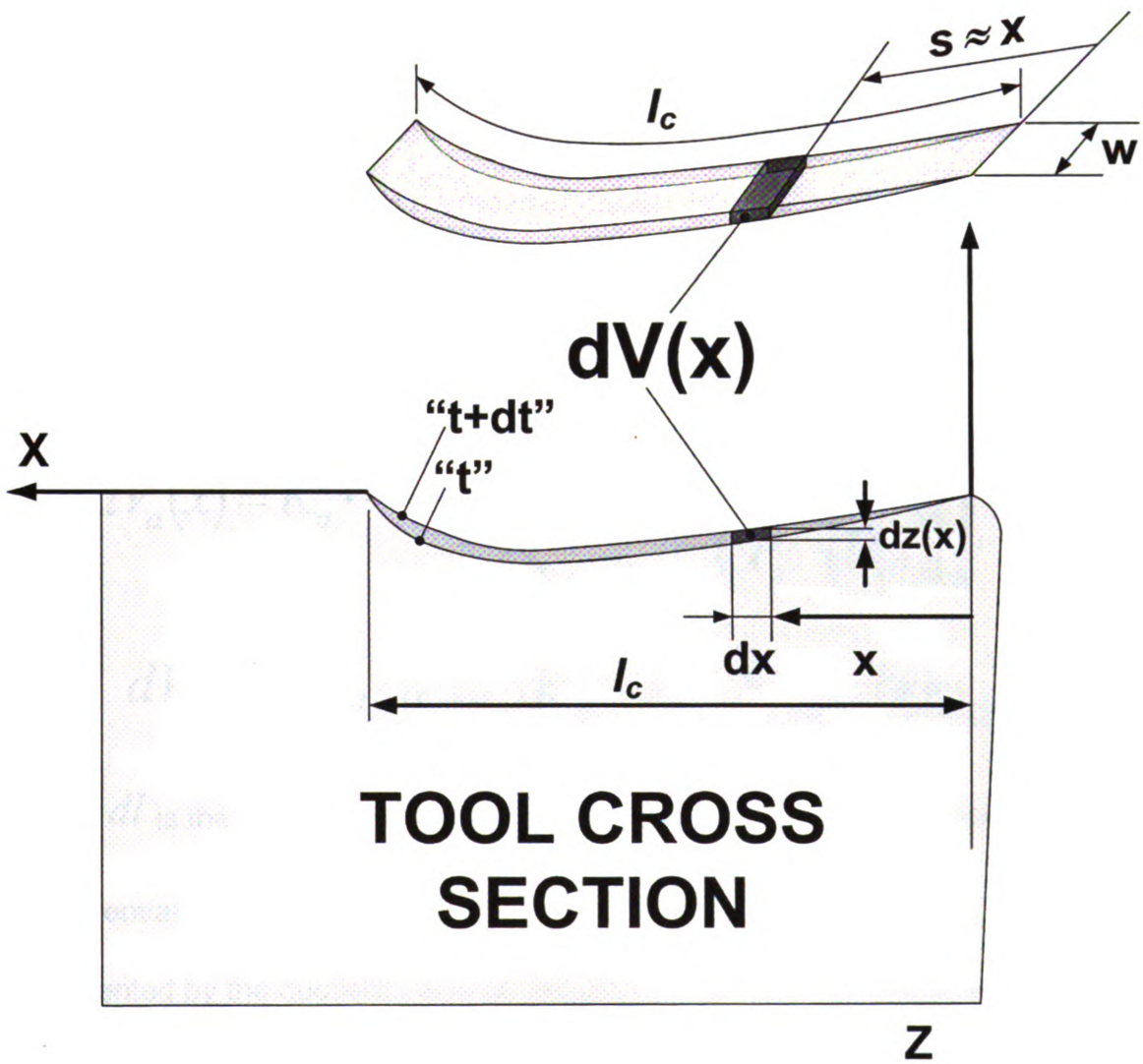

Figure 44 Wear in local form

Next, the total differential volume at location x, i.e. $dV(x)$, is assumed to be composed by the volumes worn-off by the dissolution and abrasion mechanisms as follows

$$dV(x) = dV_d(x) + dV_a(x) \quad \text{...(18)}$$

where $dV_d(x)$ and $dV_a(x)$ represent the local, volumetric wear losses due to the dissolution and abrasion wear mechanisms, respectively. The two terms in the Right Hand Side (RHS) of Equation (18) are proposed as local versions of the averaged type of models represented by Equations (3) and (11) in Chapter 1. Thus, the following relationships are proposed associated with Figures 43, 44, and 45

$$dV_a(x) = K_a \cdot \frac{\sigma(x) \cdot w \cdot dx \cdot dl}{K_e} \cdot \left[\frac{P_a^{n-1}[T(x)]}{P_t^{n-1}[T(x)]} \right] \quad \text{...(19)}$$

$$dV_d(x) = K_d \cdot w \cdot dl \cdot dz_{\text{int}} \cdot M_r \cdot S_{AxByCz}(x) \quad \text{...(20)}$$

where dl is the differential length of chip which has slid over the element dx in a differential of time dt (Figure 45). M_r is the relative molar volume represented by the quotient between the molar volume of the tool material and the molar volume of the chip material, and $S_{AxByCz}(x)$ is the solubility of the tool material in the chip material. K_d and K_a are the wear coefficients for the

dissolution and abrasion wear mechanism, respectively. In Figure 45 it is observed that in a differential time, dt, a differential of chip length dl slides over all tool locations of length dx. dz_{int} is a quantity introduced solely for the purpose of modeling the volumetric nature of solid solution formation at the interface, and can be interpreted as a distance measured from the tool-chip interface towards the inside of the chip. dz_{int} limits a differential chip volume instantaneously interacting with the tool at location x.

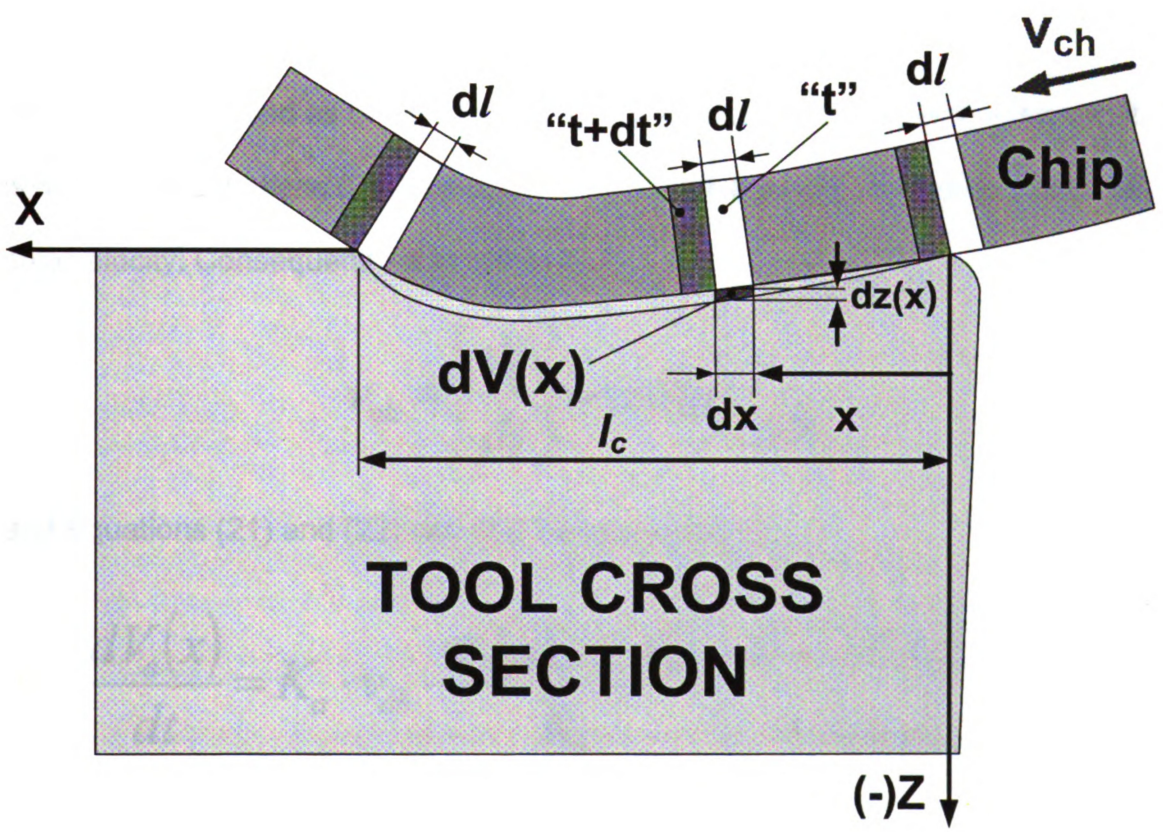

Figure 45 Differentials of chip length sliding simultaneously over rake face elements

If both sides of Equations (19) and (20) are divided by dt and terms are rearranged for the volumetric wear rates for dissolution and abrasion are obtained

$$\frac{dV_s(x)}{dt} = K_a \cdot \left(\frac{dl}{dt}\right) \frac{\sigma(x) \cdot w \cdot dx}{K_e} \cdot \left[\frac{P_a^{n-1}[T(x)]}{P_t^n[T(x)]}\right] \quad ...(21)$$

$$\frac{dV_s(x)}{dt} = K_s \cdot \left(\frac{dl}{dt}\right) w \cdot dl \cdot dz_{\text{int}} \cdot M_r \cdot S_{AxByCz}(x) \quad ...(22)$$

Evidently dl/dt represents the local chip velocity v_{ch}. In this development, this term will be modeled as being constant at any point on the rake face; however, it is noted that Equations (21) and (22) can accommodate also a varying interfacial chip velocity. Consequently, it is stated that

$$v_{ch} = \left[\frac{dl}{dt}\right] = const \quad ...(23)$$

and Equations (21) and (22) can now be expressed as

$$\frac{dV_a(x)}{dt} = K_a \cdot v_{ch} \cdot \frac{\sigma(x) \cdot w \cdot dx}{K_e} \cdot \left[\frac{P_a^{n-1}[T(x)]}{P_t^n[T(x)]}\right] \quad ...(24)$$

$$\frac{dV_d(x)}{dt} = K_d \cdot v_{ch} \cdot w \cdot dl \cdot dz_{\text{int}} \cdot M_r \cdot S_{AxByCz}(x) \quad ...(25)$$

The wear rate $\dot{z}(x)$ can be obtained using the following relationship

$$\frac{dV(x)}{dt} = \frac{dz \cdot dx \cdot w}{dt} = \left(\frac{dz}{dt}\right) \cdot dx \cdot w = \dot{z}(x) \cdot dx \cdot w \quad \text{...(26)}$$

Applying to (24) and (25)

$$\dot{z}_a(x) = K_a \cdot v_{ch} \cdot \frac{\sigma(x)}{K_e} \cdot \left[\frac{P_a^{n-1}[T(x)]}{P_t^n[T(x)]}\right] \quad \text{...(27)}$$

$$\dot{z}_d(x) = K_d \cdot v_{ch} \cdot \left(\frac{dz_{\text{int}}}{dx}\right) \cdot M_r \cdot S_{AxByCz}(x) \quad \text{...(28)}$$

Although the introduction of dz_{int} was needed for modeling purposes (i.e., to transform Kramer-Suh's averaged model (1980) into a volumetric, local version), no information is available at this time to estimate its value; thus, in what follows its effect is absorbed into the wear coefficient K_d. To simplify further the handling of Equations 27 and 28, the following conventions are used

$$I_d(x) = M_r \cdot S_{AxByCz}(x) \quad \ldots(29)$$

$$I_a(x) = \frac{\sigma(x)}{K_e} \cdot \left[\frac{P_a^{n-1}[T(x)]}{P_t^n[T(x)]} \right] \quad \ldots(30)$$

The symbols chosen for these quantities, i.e., $I_d(x)$ and $I_a(x)$, are related to their role when integrating them to obtain wear losses. Because of this integration step the quantities $I_d(x)$ and $I_a(x)$ are called integrands in what follows.

Finally the wear rate can be expressed as

$$\dot{z}(x) = \frac{dz(x)}{dt} = v_{ch} \cdot \left[K_d \cdot I_d(x) + K_a I_a(x) \right] \quad \ldots(31)$$

Then the difference between two consecutive profiles is given by the integration of Equation (31).

$$z(x)\Big|_t - z(x)\Big|_{t_o} = v_{ch} \cdot \left[K_d \cdot I_d(x) + K_a I_a(x) \right] \cdot (t - t_o) \quad \ldots(32)$$

4.1.1 Compound solution and abrasion integrands

Equation (32) can be readily applied to the case of a single material, e.g. an uncoated carbide insert, as long as we assumed that dissolution and abrasion

dominate the gradual tool wear. Provided that in the current model a carbide substrate coated with multiple layers is considered, it is expected that at an arbitrary time the rake face will be a composite surface. That is, an area of one material repeatedly surrounded by another area of a different material, being the most complex configuration that of an area of WC (substrate) surrounded by TiCN, surrounded by Al_2O_3, and finally surrounded by TiN (top layer). In Figure 46, an example where the current wear front (crater profile) composed by TiN surrounding Al_2O_3, and Al_2O_3 in turn surrounding TiCN is shown. Thus, a compound expression for $I_d(x)$ and $I_a(x)$ which reflects the heterogeneity of the rake face at any instant was sought. The relationships defining $I_d^c(x)$ and $I_a^c(x)$ for Figure 46 can be expressed as

$$I_d^c(x) = \sum_{i=1}^{i=5} \left[\langle I_d(x) \rangle_i \right] \quad \text{...(34)}$$

$$I_a^c(x) = \sum_{i=1}^{i=5} \left[\langle I_a(x) \rangle_i \right] \quad \text{...(35)}$$

where the brackets $\langle\ \rangle$ indicate the validity of the quantity only within the region indicated by the number in the subscript. The each region's length in Equations (34) and (35) is defined automatically by the wear front as it progresses into the

coatings. The computer model developed in Matlab 7.0 "senses" the boundaries of each coating based on their experimental thicknesses. The compound integrand is a formal way to express the utilization of specific tool wear integrands according to the position x and the current depth z (i.e. current coating exposed at location x). On view of this, Equation (32) was re-written as

$$z(x)\Big|_{t} - z(x)\Big|_{t_o} = v_{ch} \cdot \left[K_d \cdot I_d^c(x) + K_a I_a^c(x)\right] \cdot (t - t_o) \quad \ldots(36)$$

here $I_d^c(x)$ and $I_a^c(x)$ are the compound expressions for the dissolution and abrasion integrands, respectively.

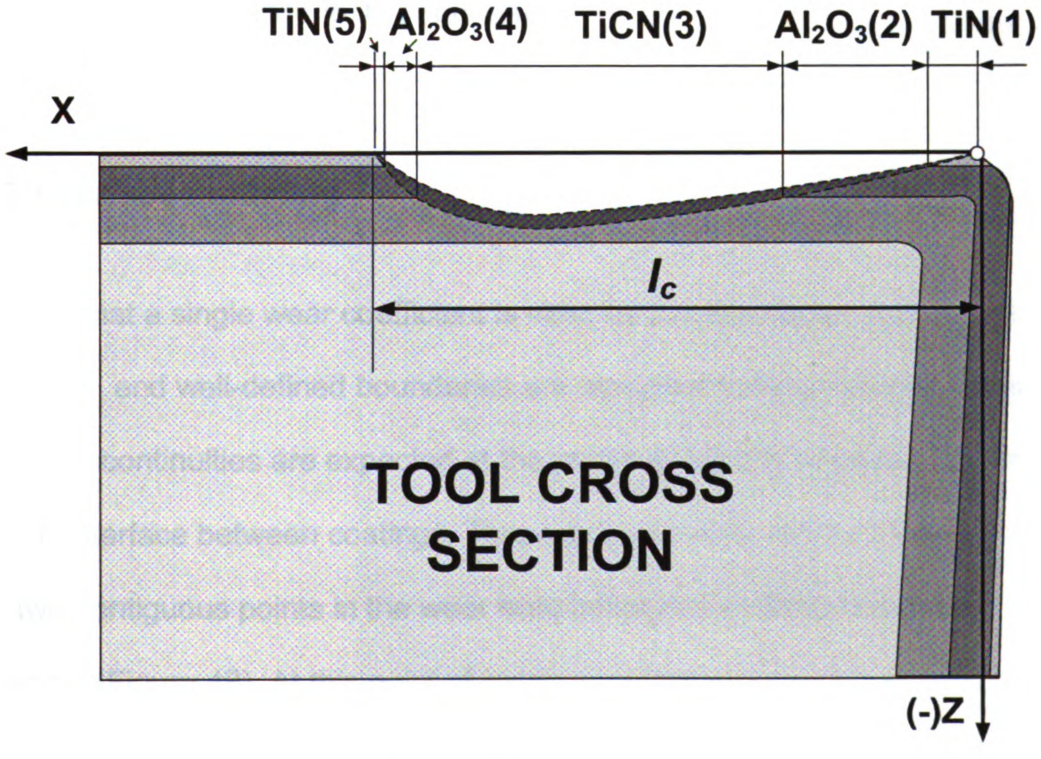

Figure 46 The compound nature of the tool wear front

4.1.2 Active wear zone

The rake face can be divided into two main zones (Figure 47) according to experimental observations in Appendix B. The first zone, close to the cutting edge, is the stagnant zone where periodic accumulation and detachment of chip material is expected (Kim, 2000). Experimentally, plenty of steel particles are found to be attached to the stagnant zone when observed under the microscope; however, signs of wear produced by the flowing chip are not noticeable. On the other hand, in the zone between the limit of the stagnant zone and the trailing edge wear activity is clearly noted (i.e., wear micro-grooves marks in the direction of the chip flow). Thus, this zone is where the tool wear occurs. From this point onwards, this zone will be named the active wear zone and all the wear calculations will be limited to its boundaries.

4.1.3 Interface modeling

Provided that a single wear coefficient is used for the dissolution and abrasion integrands, and well-defined boundaries are assumed between coating layers, sudden discontinuities are expected at the points where the wear front coincides with the interface between coatings. These discontinuities will be evident if we take two contiguous points in the wear front belonging to different layers (coatings) (Figure 48). At this point of model development, these two points, though contiguous, will be assigned different wear rates by the algorithm.

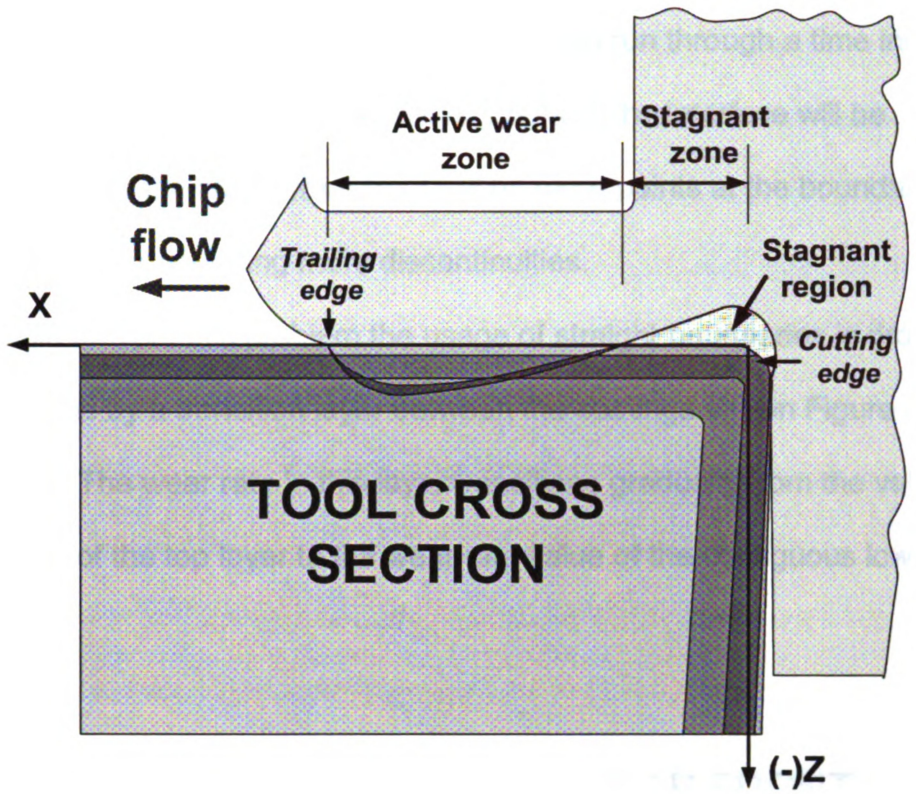

Figure 47 The active wear zone

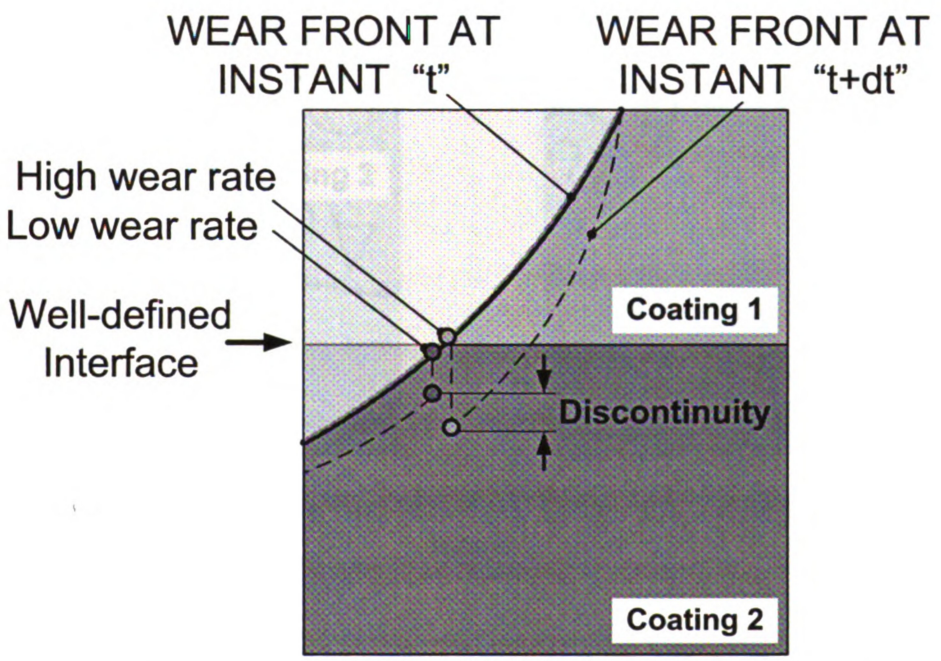

Figure 48 Wear front at the interface between coatings

If the computer simulation is implemented to run through a time interval with the assigned wear rates a discontinuity right at the interface will be observed. In time, the crater wear front will hit more points at the boundaries between coatings generating more discontinuities.

To circumvent this problem the usage of straight boundaries is dropped and is replaced by a transition layer between the coatings shown Figure 49 as Interface 1-2. The wear rate in this layer transitions gradually from the value of the wear rate of the top layer to the wear rate value of the contiguous lower layer (Figure 50).

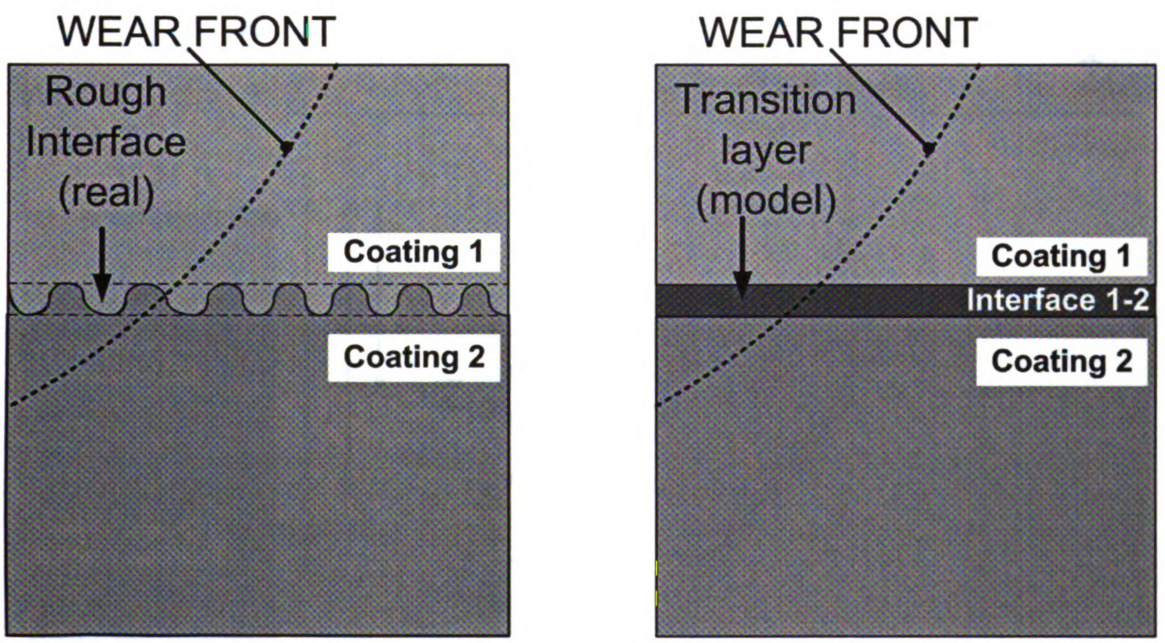

Figure 49 Replacement of a real interface between coatings by a transition layer

The assumption of this transition layer is in accord with the experimental observations of cross sectional areas of new inserts where the boundary

between coatings is rough (peaks and valleys). The distance peak-to-valley of the interfaces was measured to be around 1 μm. In Figure 50 the wear rate assigned by the model to a point of the wear front currently located at the transitional interface is linearly interpolated between two wear rates as depicted by

$$\dot{z}(x)=\dot{z}_1(x)+\left[\frac{\dot{z}_2(x)-\dot{z}_1(x)}{z_{I_f}(x)-z_{I_o}(x)}\right]\left(z(x)-z_{I_o}(x)\right) \quad \text{.....(36)}$$

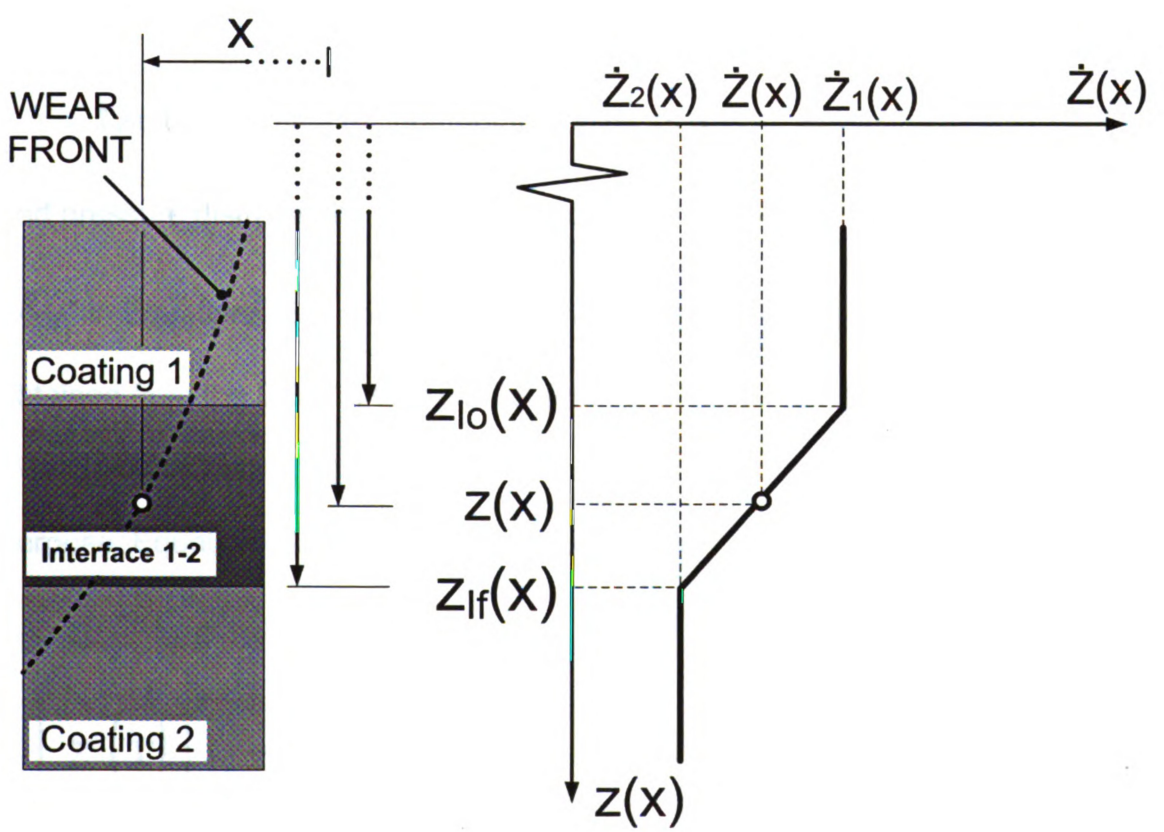

Figure 50 Modeling of the wear rate in the transition layer

Therefore Equations (34) and (35) are modified to

$$I_d^c(x) = \sum_{i=1}^{i=5} \left[\langle I_d(x) \rangle_i \right] + \sum_{i=1}^{i=4} \langle I_d(x) \rangle_{(i)(i+1)} \quad \ldots(37)$$

$$I_a^c(x) = \sum_{i=1}^{i=5} \left[\langle I_a(x) \rangle_i \right] + \sum_{i=1}^{i=4} \langle I_a(x) \rangle_{(i)(i+1)} \quad \ldots(38)$$

4.1.4 Wear coefficients determination

Two consecutive experimental profiles as well as interfacial temperature and pressure distributions can be used to obtain the wear coefficients "K_d" and "K_a" in Equations (32) and (36). In this work, wavelet-filtered crater profiles obtained from the DEKTAK6M profiler and FEM temperature and pressure distributions (Chapter 3) were used for the coefficients determination. For this purpose, Equation (36) may be expressed as

$$\left[\frac{z(x)\big|_{t_2} - z(x)\big|_{t_1}}{v_{ch} \cdot (t_2 - t_1)} \right] = K_d \cdot I_d^c(x) + K_a^c \cdot I_a^c(x) \quad \ldots(39)$$

where t_1 and t_2 are the cutting times at which the experimental crater profiles $z(x)\Big|_{t_1}$ and $z(x)\Big|_{t_2}$ have been measured. Equations (24) and (25), however, possesses two unknowns, the wear coefficients K_d and K_a. An important part of the model will be the determination of their values. It is widely accepted that the Maximum Crater Depth Location (MCDL), i.e. $x = x_m$, coincides with the Maximum Temperature Location (MTL) where dissolution wear dominates. At this high temperature the effect of the abrasive wear mechanism is impaired to a great extent and the effect of dissolution wear is at its maximum. Therefore, the following equation can be written at this specific location.

$$\left[\frac{z\left(x_m\right)\Big|_{t_2} - z\left(x_m\right)\Big|_{t_1}}{v_{ch}\cdot\left(t_2 - t_1\right)}\right] \approx K_d \cdot I_d\left(x_m\right) \quad \ldots(40)$$

Assuming the equality K_d can be obtained

$$K_d = \left(\frac{1}{I_d(x)}\right)\left[\frac{z\left(x_m\right)\Big|_{t_2} - z\left(x_m\right)\Big|_{t_1}}{v_{ch}\cdot\left(t_2 - t_1\right)}\right] \quad \ldots(41)$$

where K_d will represent the value of the dissolution wear coefficient. The abrasion coefficient K_a will be obtained as an average value from a modified version of Equation (25) as follows

$$K_a = \left\{ \sum_{i=1}^{M} \left[\frac{z(x)\big|_{t_2} - z(x)\big|_{t_1}}{v_{ch} \cdot (t_2 - t_1)} \right] - K_s \cdot I_s^c(x) \right\}_i / M \quad \ldots(42)$$

where M is the number of points considered on the rake face for the profile during the computer simulation.

4.1.5 Profile prediction

The relevant point for the profile prediction is to define how often the profile is going to be updated. This problem could be solved by updating the profile every time a chip length $l = l_c$ traverses the rake face, however, this results in a extremely small time interval (in the order of $10^{-4} s$ for a cutting speed of 250 m/min) which slows down the computations. Thus, a multiple of this time is proposed to define how frequent the profile is updated. The optimal value of this time could be found by trial and error during the actual simulations. The following equations were used for profile prediction

$$\Delta t = \frac{v_{ch}}{l_c} \quad ...(43)$$

$$\Delta t_{sim} = N_{sim} \cdot \Delta t \quad ...(44)$$

$$\Delta t_{sim} = t_i - t_{i-1} \quad ...(45)$$

$$z_i(x) = z_{i-1}(x) - \left[\Delta z(x)\right] \Big|_{i-1} \quad ...(46)$$

$$\left[\Delta z(x)\right] \Big|_{i-1} = \left[K_s \cdot I_s^c(x) + K_a \cdot I_a^c(x)\right] \Big|_{i-1} \left[\frac{v_{ch} \Delta t_{sim}}{l_c}\right] \quad ...(47)$$

Where:

Δt_{sim} : Time step for the computer simulation

N_{sim} : integer defining a multiple of Δt

i : time step index identifier

4.2 PREDICTION RESULTS AND DISCUSSION

In Figure 51 a comparison between the wavelet-filtered profiles and the predicted profiles is presented. The horizontal lines drawn in both pictures represent the limits between coating layers and transition layers. The calculated limit between α–Al_2O_3 and κ–Al_2O_3 is also considered. It is noted that the model

predicts the profile fairly well up to 8 min. of cutting time; however, after this cutting time some deviations start to show up.

The differences between the model predictions and the experimental profiles after 8min. can be explained if it is noted that the experimental "stagnant" profiles for 6, 8, and 12 min lie in the α-Al_2O_3 region, whereas the profiles for 12, 14 and 16 min. belong to the κ-Al_2O_3 region. Vuorinen and Karlsson (1992) reported that CVD deposited α-Al_2O_3 possessed a much better wear resistance compared to CVD κ-Al_2O_3 when machining steels. However, they also observed that if the κ–to-α phase transformation the typical thermal-CVD cracks expanded and smaller cracks formed inside the original thermal cracks which lead to poor wear resistance of the newly transformed α-Al_2O_3 According to the FEM results shown in Chapter 2, the temperature is between 850 °C and 1000°C and the pressure is around 1GPa. These are the ideal conditions for the κ–to-α transformation to occur. Thus, when the wear front hits κ-Al_2O_3 higher wear rates are expected compared to α-Al_2O_3 assuming the transformation occurs.

As pointed out in Chapter 2, the cutting tool edge deforms plastically. The trailing edge is moved upwards (~3μm) while the cutting edge was lowered (~4μm). This phenomenon has been pointed by some authors (Kramer, 1993; Astakhov, 2006) as critical for coated carbides due to their longer exposure to higher temperatures and pressures compared to uncoated ones.

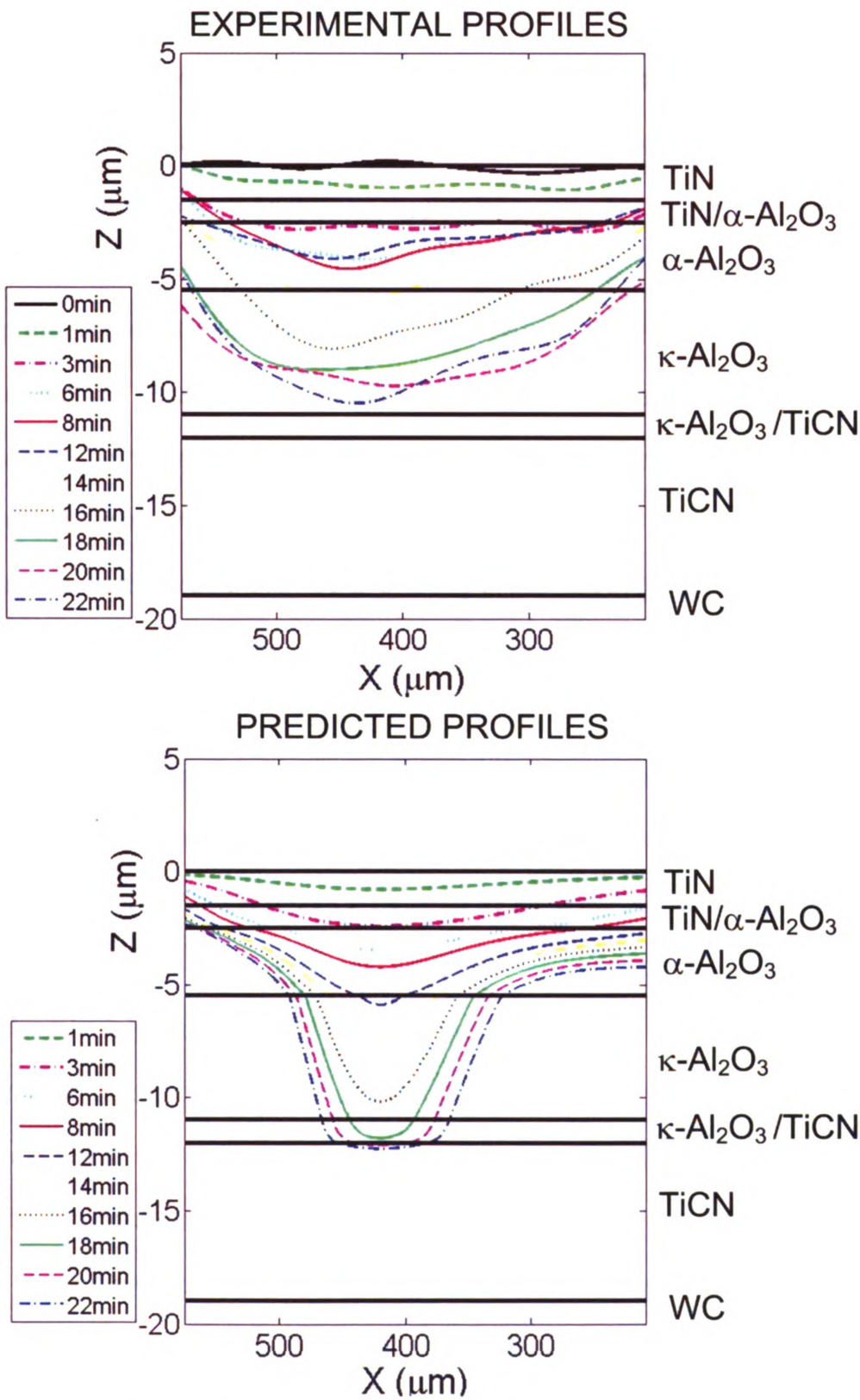

Figure 51 Experimental and Predicted Profiles

An schematic view of the deformation of the tool tip is presented in Figure 52. Although the deformation distances mentioned seem to be very small they are comparable in size to the thickness of the coatings. Therefore, it can be argued that the wear front instead of digging perpendicular to the coatings, starts hitting the coatings from the side after plastic deformation happens. This can explain the slanted position of the TiCN when exposed and also can contribute to a longer tool life. Plastic deformation of the tool impacts the wear parameters readings impairing an accurate extraction of wear coefficients, i.e. the crater profiles contain inevitably deformation that is accounted as wear in the calculations. In the present case this is a key issue due to the comparable sizes of coatings and deformations. Tool tip deformation is controlled by a creep process (Astakhov, 2006).

When TiCN was hit a high wear rate was expected due to the large difference in solubilities with Al_2O_3, however, the experimental profiles showed that the wear front followed a shape dictated by the Al_2O_3 surrounding the TiCN coating. Although the model takes care of this by assuming wear coefficients for TiCN close in value to the TiCN ones, a qualitative explanation of how this happens can be attempted. Figure 53 presents the wear front hitting for the first time the TiCN layer. If a high wear rate settles in due to the differences in solubility, the presence of Al_2O_3 surrounding TiCN will impede the wear front growth in such a way. Therefore, the wear front is dictated by Al_2O_3. As TiCN is exposed more and more, the friction conditions will change reducing the temperature and thus reducing wear. When enough

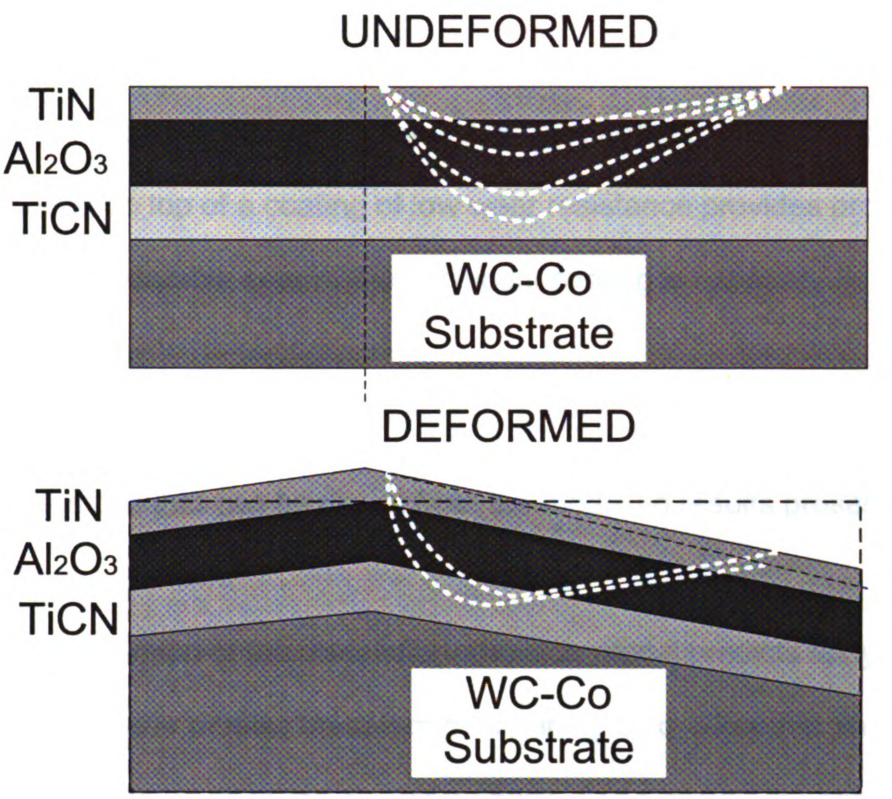

Figure 52 Plastic deformation of the tool tip

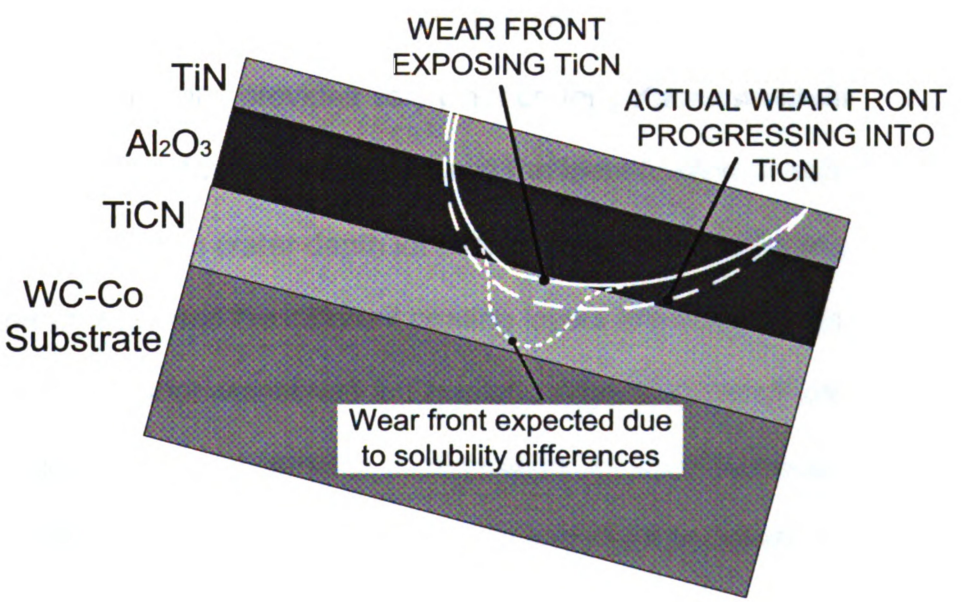

Figure 53 Effect of the stacking sequence on the wear rate

TiCN interfacial area is exposed, the differences in solubility will override these two previous effects and very fast wear rate will happen. This apparent high wear resistance is a property of the stacking sequence where a high resistant coating on top of a coating of low wear resistance provides protection even when a considerable area of the subjacent coating is exposed.

4.3 SUMMARY ON LOCAL TOOL WEAR PREDICTIONS

The conclusions that can be drawn from the modeling results presented in this chapter are as follows

- The local version of the dissolution-abrasion model predicts fairly well the crater tool wear profiles up to 8 min. of cutting time. After that phase transformation, cutting-tool tip deformation, and the stacking sequence configuration (change in tribological conditions) play a role in the deviation of the present model away from experimental observations.
- Wavelet filtering provides very clear crater patterns which facilitates the calculation of wear coefficients and the identification of wear trends
- The maximum crater depth location is observed to change as wear progresses and the different coating layers are being exposed. This confirms what was stated in Chapter 2 regarding the effectiveness of multilayer coated carbides configuration. As wear progresses digging into multiple crater locations, longer time and much more effort are required.
- The stacking sequence plays an important role in the wear resistance of multilayer coated carbides.

Chapter 5

CONCLUSIONS

A tool wear modeling effort in which averaged wear models were recast into local expressions for multilayer coated carbides has been presented in this work.

Before undertaking the modeling step, a survey on the current state of tool wear mechanisms, experimental work and surface feature extraction was performed. In this survey the main wear mechanisms in the machining of steel with coated carbides were identified, namely the generalized dissolution and abrasion. The generalized dissolution wear was accepted to be more applicable to explain crater wear .Regarding, abrasion it was recognized that three-body abrasive wear model can be readily applied to model tool wear at the rake face. Chemical reaction was also shown to be plausible when machining highly reactive materials such as Titanium.

Several conclusions can be drawn form the experimental findings. The effectiveness of multilayer coated carbides was observed to depend in the changing location of the maximum crater depth as well as in the combined wear resistance of the coatings currently present at the interface. The former implies not only the maximum crater location changes as wear progresses but that the whole crater pattern varies with cutting time. This is analogous to digging a hole in the ground by concentrating efforts in multiple locations. Evidently, much more effort and time is required compared to the situation in which one fixed location is picked. The fresh inserts though not specified by the manufacturer contain an

intermediate Alumina layer composed by two different layers made of α-Al_2O_3 (first) and κ-Al_2O_3 (second). Due to the high pressure and temperature at the rake face provided by the ALE-FEM simulations the κ– α -Al_2O_3 transformation is highly probable. The analysis of the SP crater profiles along with the CSLM topography led to the conclusion of the creep deformation of the cutting tool substrate. The cutting edge was observed to be lowered while the trailing edge moved up from their original positions.

The application of wavelet analysis to CLSM and SP data sets from the tool surface proved very powerful to de-noise and decouple roughness, waviness, and form. Wavelet-filtered crater patterns provided clear wear trends in both 2D and 3D topography description without losing the localization of the wear features. Additionally, SP crater patterns post-processed with wavelets were useful to identify unambiguously the changing nature of the wear front as well as the calculation of the wear coefficients. The deformation at the trailing edge was clearly observed using the surfaces reconstructed with wavelets. Finally, a potential path for the characterization of wear micro-patterns was opened, by proving the feasibility of scale decupling by means of wavelets.

The profiles predicted present fairly good agreement with the experimental profiles until 8 min cutting. After that the model agrees with the general trend observed experimentally but deviations start to take over. The deviations in the predicted profiles stem from different sources such as the changing friction conditions as the wear front exposes subjacent coating layers, the κ– α -Al_2O_3 phase transformation and the tool edge deformation. Although the changing

location of the maximum crater depth points to changing friction conditions, the present model assumes steady state temperature and pressure profiles based on a single friction coefficient. Here it suffices to say that contact conditions modeling and implementation is a problem by itself. The model developed cannot explain the "stagnant" profiles observed experimentally at 6, 8, and 12 min cutting time. However, it was noted that the MCDL in these three profiles was in the α-Al_2O_3 layer and a faster wear rate was observed for crater depths coinciding with the κ-Al_2O_3 layer. This is in agreement with previous findings (Vuorinen and Karlsson,1992) in which CVD α-Al_2O_3 was more wear resistant than CVD κ-Al_2O_3 mainly because of phase transformation. Interestingly, the phase transformation goes from κ to α but the α-Al_2O_3 thus formed resists wear poorly compared to the original κ-Al_2O_3.

The cutting tool tip deformation concurrently happening with crater tool wear cripples to some extent the extraction of model wear coefficients. The measured crater wear geometry convolutes both wear and tip deformation and thus the wear coefficients contained this coupled effect. A visible evidence of the tip deformation is the slanted TiCN area exposed when the crater wear front hits this coating.

The stacking sequence plays a chief role in the resistance of multilayer coated carbides. This was clearly manifested when the crater wear front hit the Al_2O_3 -TiCN interface. Based on the solubility differences, a fast wear rate at the crater center was expected when the wear front hit the TiCN layer; however, the real wear profile did not show any abrupt change when going from Al_2O_3 to TiCN.

It was observed that the wear front shape was dictated by the Al_2O_3 regions still remaining on the rake face. The model takes this into account by assuming wear coefficients close in value to those of TiN (top layer).

APPENDIX A: ALE Finite Element simulations

Arbitrary Eulerian-Lagrangian (ALE) adaptive meshing in ABAQUS/Explicit is capable of preventing numerical errors and severe distortions without altering the topology of the mesh so that a high-quality mesh can be maintained during the simulation (Madhavan and Abidi-Sedeh, 2005 and Haglund et al., 2006, ABAQUS Manual).

FINITE ELEMENT MODEL

The following are results obtained by the Michigan State University Predictive Tool Wear research group. The ALE formulation was adapted for orthogonal cutting simulation using ABAQUS/Explicit version 6.6. The Johnson-Cook (J-C) (Johnson and Cook, 1983) model was implemented for its simplicity and availability of material parameters. Four node bilinear displacement and temperature quadrilateral elements (CPE4RT) for both workpiece (2143 elements) and cemented carbide tool (1282 elements) including the composite coating (278 elements) were used. The cutting tool was assumed a mechanically rigid body. A single composite coating combining the thermal conductivities of each layer was used to avoid complications when modeling layers individually. The 'equivalent' thermal conductivity (Yen et al. 2004) was calculated based on the data provided by Grzesik and Nieslony (2004), as

$$\frac{L_{total}}{K_{eq}} = \frac{L_{TiN}}{K_{TiN}} + \frac{L_{Al_2O_3}}{K_{Al_2O_3}} + \frac{L_{TiCN}}{K_{TiCN}} \quad \text{...(A-1)}$$

Table A-1 Workpiece material's constants according to Johnson-Cook model (Yen et al., 2004)

Material Constants for J-C model (AISI 1045)					
A (MPa)	B (MPa)	C	n	M	Tm
553.1	600.8	0.0134	0.234	1	1460

Table A-2 Materials' properties (Yen et al., 2004)

Material/Property	AISI 1045	WC-Co	TiN	TiN/Al_2O_3/TiCN
Young's modulus (GPa)	212 (20°C) 207 (100°C) 192 (300°C) 175 (500°C)	612	250	
Poisson's ratio	0.3	0.22	0.25	
Density (kg/m3)	7844	11900	4650	
Conductivity (W/m°C)	50.7 (100°C) 41.9 (400°C) 30.1 (700°C) 26.8 (1000°C)	86	9.4	
Specific heat (J/kg°C)	486 (75°C) 548 (275°C) 649 (475°C) 770 (675°C) 548 (875°C)	334.01 +0.12T(°C)		22/26/27 (25°C) 23/18/30.5(200°C) 26/8/34 (727°C) 26.5/4/35 (927°C) 27/6/36 (1200°C)
Thermal Expansion (µm/m°C)	11.9 (20°C) 12.5 (100°C) 13.6 (300°C) 14.5 (500°C) 15.1 (700°C)	4.9 (200°C) 5.2 (400°C) 6.5 (600°C)		25.9 (25°C) 22.21(200°C) 12.96 (727°C) 7.25 (927°C) 10.33 (1200°C)

The Coulomb friction model between workpiece and carbide tool was implemented and four simulations were run with friction coefficients of 0.25, 0.4,

0.5, and 0.75. The material properties of the workpiece, tool insert and coatings are given in Tables A-1 and A-2.

Constitutive model for workpiece

The J-C constitutive model, suited for the simulation of metals subjected to large strains, high strain rates and high temperature, was used for the AISI 1045 steel. It can be expressed as

$$\sigma = (A + B\varepsilon^{n})(1 + C\ln\dot{\varepsilon}^{*})(1 - T^{*m}) \quad \text{...(A-2)}$$

where σ is the stress, ε is the equivalent strain, $\dot{\varepsilon}^{*} = \dot{\varepsilon} / \dot{\varepsilon}_0$ is the dimensionless strain rate ($\dot{\varepsilon}_0$ =1.0 s^{-1}) and A, B, C, n and m are the material constants (Ozel and Zeren, 2005). T_m^* is equal to (T-Tr)/(Tm-Tr) where T_r is a reference temperature (25°C) and T_m is the melting temperature of the workpiece.

Boundary Conditions

Figure A1 shows the boundary conditions and dimensions for workpiece and coated tool insert of our FE model. The workpiece is fixed in 1 and 2 direction and tool insert is fully constrained. Initial chip length and thickness are initially defined and chip outflow surface is defined as an Eulerian boundary so that the chip flows through the surface. The cutting conditions used in the experiments (Chapter 2) and the wear model (Chapter 4) were simulated.

These are also indicated in Figure A1 as cutting speed (V_c = 250 m/min), feed rate (f = 0.3125 mm/ rev), and cutting honing radius (r = 50 μm).

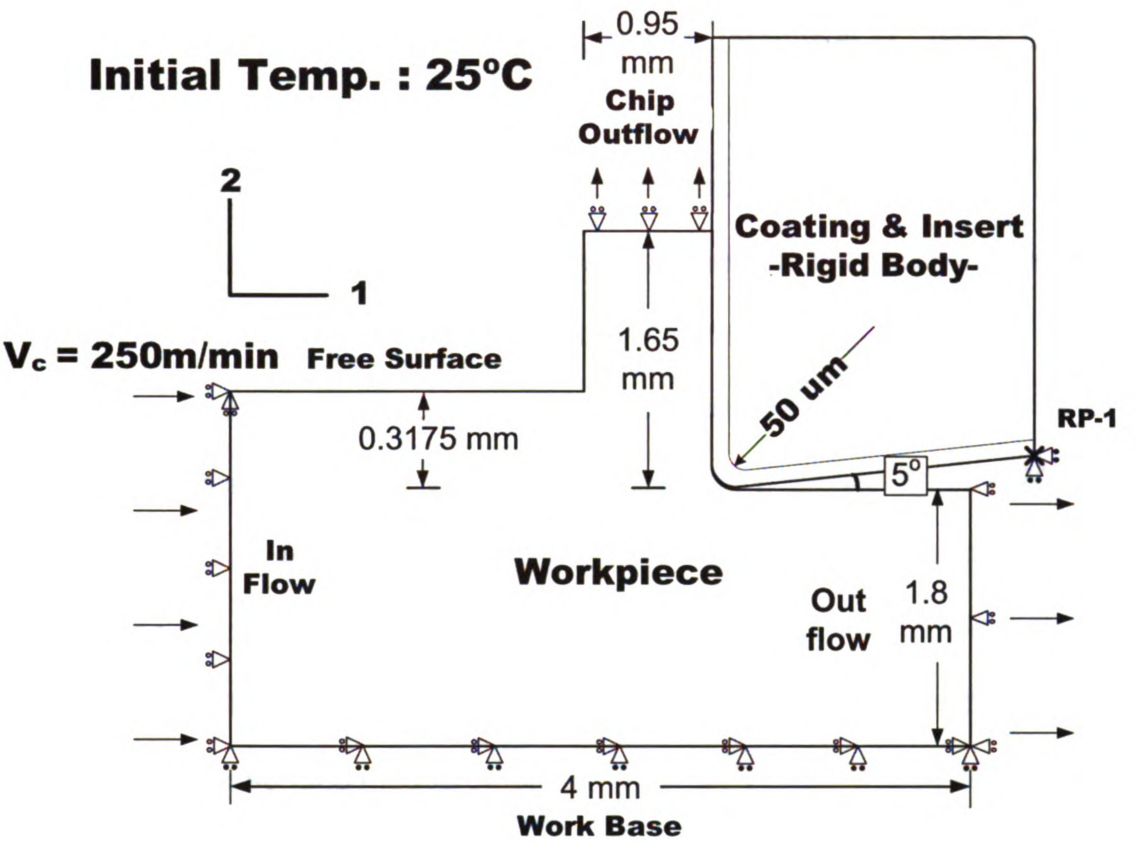

Figure A1 Cross section parallel to MICE showing the FEM model geometry and the boundary conditions.

APPENDIX B: CSLM applied to Tool Wear Analysis

Many microscopy techniques have been commonly used to characterize the surface topography in numerous scientific fields (Mathia et al., 1995): atomic force microscopy (AFM), stylus profilometry, stereo microscopy (SM), scanning electron microscopy (SEM), reflected light interference microscopy (RLIM), and confocal laser scanning microscopy (CLSM). The first two are tactile instruments, while the others are noncontact instruments. AFM, the state-of the-art profilometer, possesses excellent depth and transversal resolution. However, its drawbacks such as slow scan, very small sample field (typically 70 μm × 70 μm), restricted depth range (about 5 μm), its inability to scan deep holes, and the extreme fragility of the tip (Corle and Kino, 1996) prevented its immediate application to tool wear analysis. Stylus profilometers have been used conventionally for surface measurement of tool wear. However, this method has a number of disadvantages, which include the resolution limitations, the slow scanning rate, the potential damage to the surface investigated, and the influence of the stylus wear on the results (Anamalay et al., 1995). SM (Chakraborty et al.,2000), SEM (Farhat, 2003), and RLIM (Dawson and Kurfess 2005; Devillez et al., 2004) have also been applied to measure tool wear. Except for RLIM, these methods have proven to be burdensome and/or time consuming due to limitations on the depth of field, difficulties while obtaining and interpreting images, and the high equipment cost. CLSM has been established as a powerful tool to extract surface topography and has been used extensively in the

biological sciences since the early 1980s due to its versatile depth of field, its depth discrimination property, the minimal sample preparation required, and the cost savings relative SEM technology. However, its use in tribology research has been extremely limited.

In the past few years, some studies on the performance of confocal microscopes have been carried out to characterize machined surfaces, tribological surfaces, concrete surfaces, and biomedical surfaces (Anamalay et al., 1995; Gee and McCormick, 1992; Becker et al., 2001; Semler et al., 1997). A superior performance of confocal systems was always found for surface profiling when compared to the stylus profilometer readings. In a comparative study (Udupa et al., 2000), confocal and interferometer systems outperformed stylus ones when acquiring 3-D surfaces features. It was also found that confocal systems present important advantages against interferometry systems, such as the simplicity in their architecture, insensibility to environmental conditions, and the elimination of the interferometer's reference surface. Thus, even though RLIM has a more flexible field of view and better depth resolution compared to CSLM (Udupa et al. 2000; Miyoshi 2002; Devillez et al., 2004), RLIM is unable to determine the true surface topography when rough surfaces are involved (Whitehouse 1997; Miyoshi 2002), when the specimen is transparent to the wavelength of the system, and when the aberration
errors are present for numerical apertures larger than 0.5 (Corle and Kino, 1996). More importantly for Multi-layer coated tools (MLCCTs), RLIM is difficult to use when more than one material is involved (Miyoshi 2002) .

The Confocal Principle

The power of CLSM resides in its ability to retrieve an image exclusively from the light in the focal plane. The out-of-focus light is blocked by the pinhole in the final image, allowing a sharper image compared to that of a light microscope. In the confocal microscope, the light coming from the focal plane is focused at a point right in the position of the detector pinhole (Figure B1), and rays coming from out-of focus regions are focused either in front of or behind the detector pinhole. The contrast is improved drastically and the resolution is increased slightly. The image is mostly formed by rays coming from in-focus regions. This allows to "optically" section the sample in the region coinciding with the focal plane. The screen display of the focal plane is known as the optical section of the sample at the focal plane level (Figure B1). The gathering of data and the rendering of the images is done point by point because CLSM uses a laser beam to raster the surface. To cover the whole 3-D region of interest, the laser is scanned transversally (x and y) while the stage is stepped axially (z).

The Focus Detection Technique

When axially scanning a planar or a sloping surface through the focus of a confocal microscope, the light intensity detected reaches a maximum when the sample surface coincides with the focal plane position (Sheppard and Shotton 1997). The focus detection technique uses a computational algorithm to determine the z-position of maximum intensity during the axial scan, which corresponds to the local surface position.

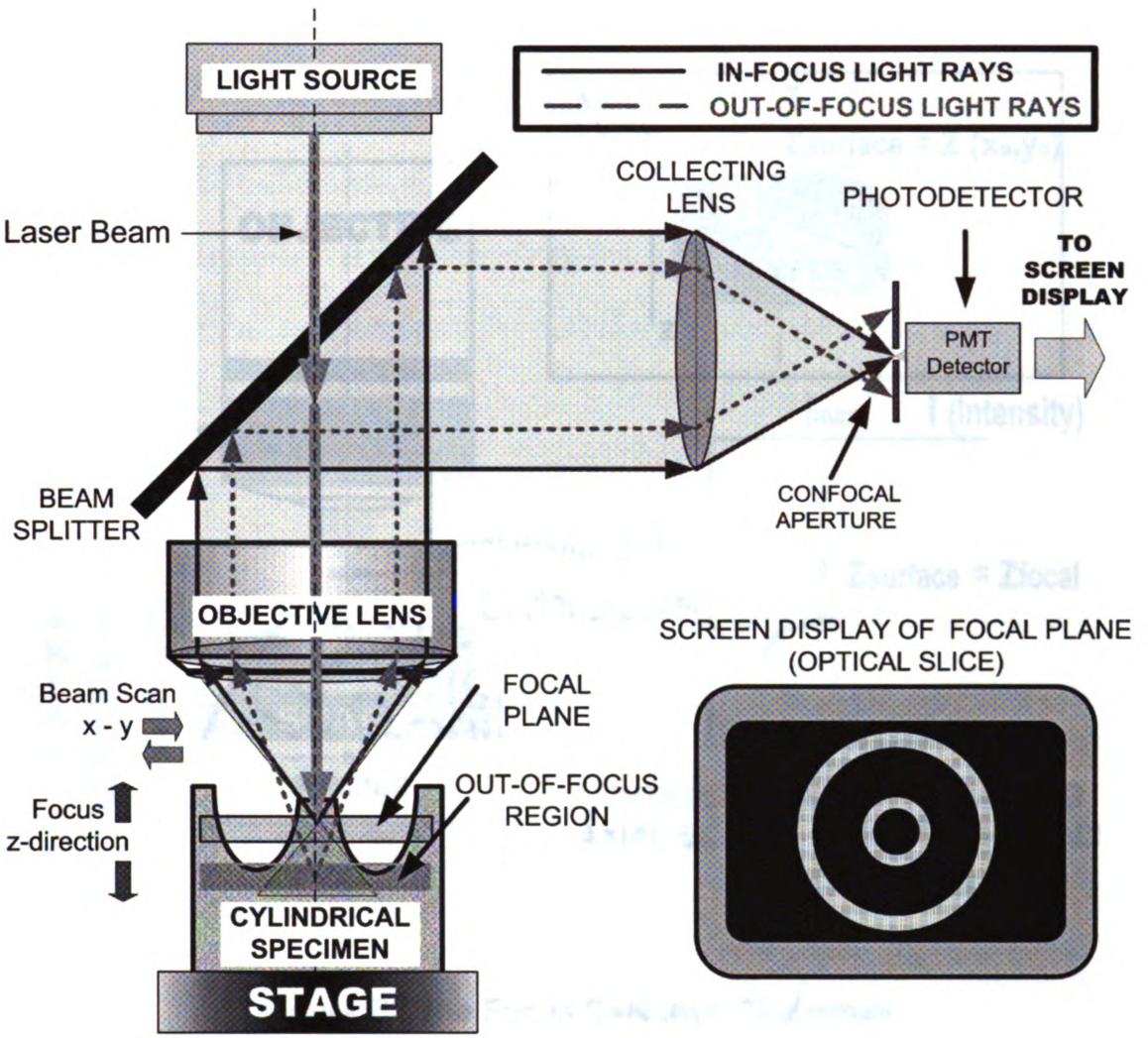

Figure B1 The Confocal Principle

The intensity maxima algorithm (Sheppard and Shotton, 1997) and the center of gravity algorithm (Sheppard and Shotton, 1997; Jordan et al., 1998), followed by the three point-fit method (Sheppard and Shotton, 1997) are the most common algorithms used to detect the axial location of the surface by identifying the intensity maxima position.

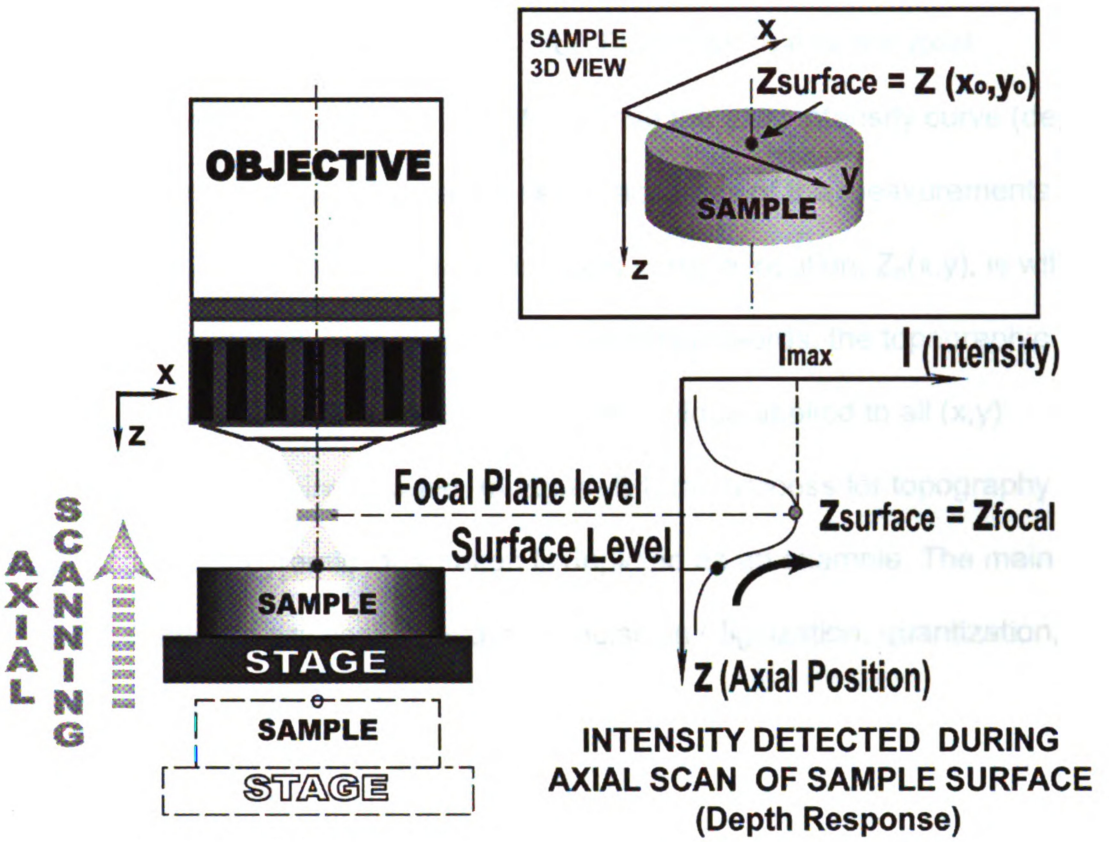

Figure B2 The Focus Detection Technique

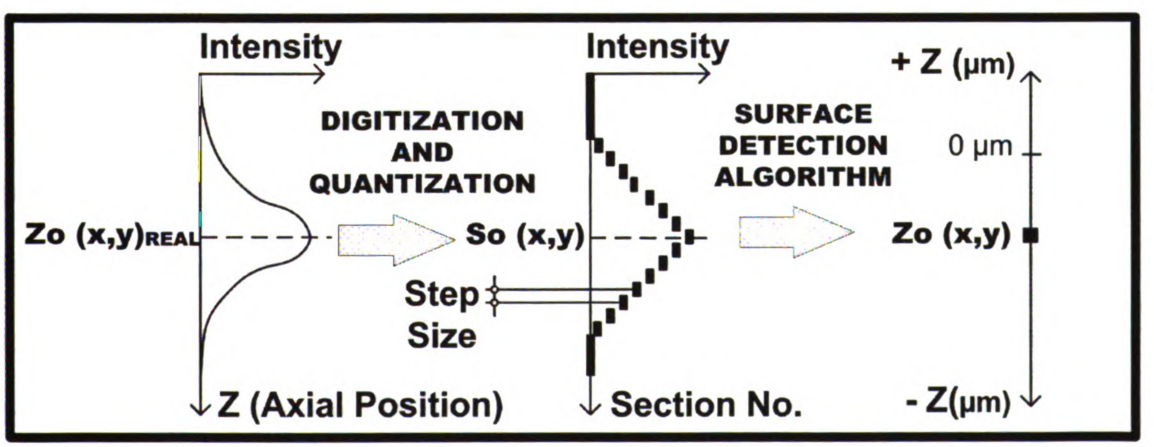

Figure B3 Focus Detection Technique Implementation

Figure B2 and B3 illustrate the focus detection principle and implementation, respectively. Figure B3 shows how the Step Size (SS), that is, the axial displacement unit of the stage, is used to sample the axial intensity curve (depth-response). Ultimately, the SS determines the accuracy of the measurements in the z-direction, i.e., how accurate the detected surface location, $Z_o(x,y)$, is with respect to real surface location, $Z_o(x,y)_{REAL}$. In simple words, the topographic surface reconstruction is the focus detection technique applied to all (x,y) locations of the area being imaged. In Figure B4, the process for topography reconstruction of a pyramid indentation is depicted as an example. The main parts of this process are scanning, data acquisition (digitization, quantization, and storage), focus detection technique application, grayscale encoding of the z-matrix, and rendering.

The scanning is done laterally (x-y) and axially (Optical Section Number – SN). The former is performed by the laser beam while the axial scanning is done by a motorized stage. The motorized stage steps according to the predefined value of the SS. The data acquisition part generates the intensity matrix, I(x,y,SN), which is the collection of discretized values of intensity at each pixel position, (x,y). The z-matrix, z(x,y), obtained as a result of the focus detection technique based on the intensity matrix, contains the detected surface positions for all discretized locations. For example, for the pixel location (7,12) shown in Figure B4, the surface will be generated based on I(7,12,13). The height encoded image (HEI) records the z-matrix information using grayscale height encoding. In the HEI, the maximum number of optical sections allowed are

matched to the maximum value of the grayscale (e.g., 256(2^8) optical sections for eight-bit grayscale). Finally, the surface topography is rendered using specialized imaging software.

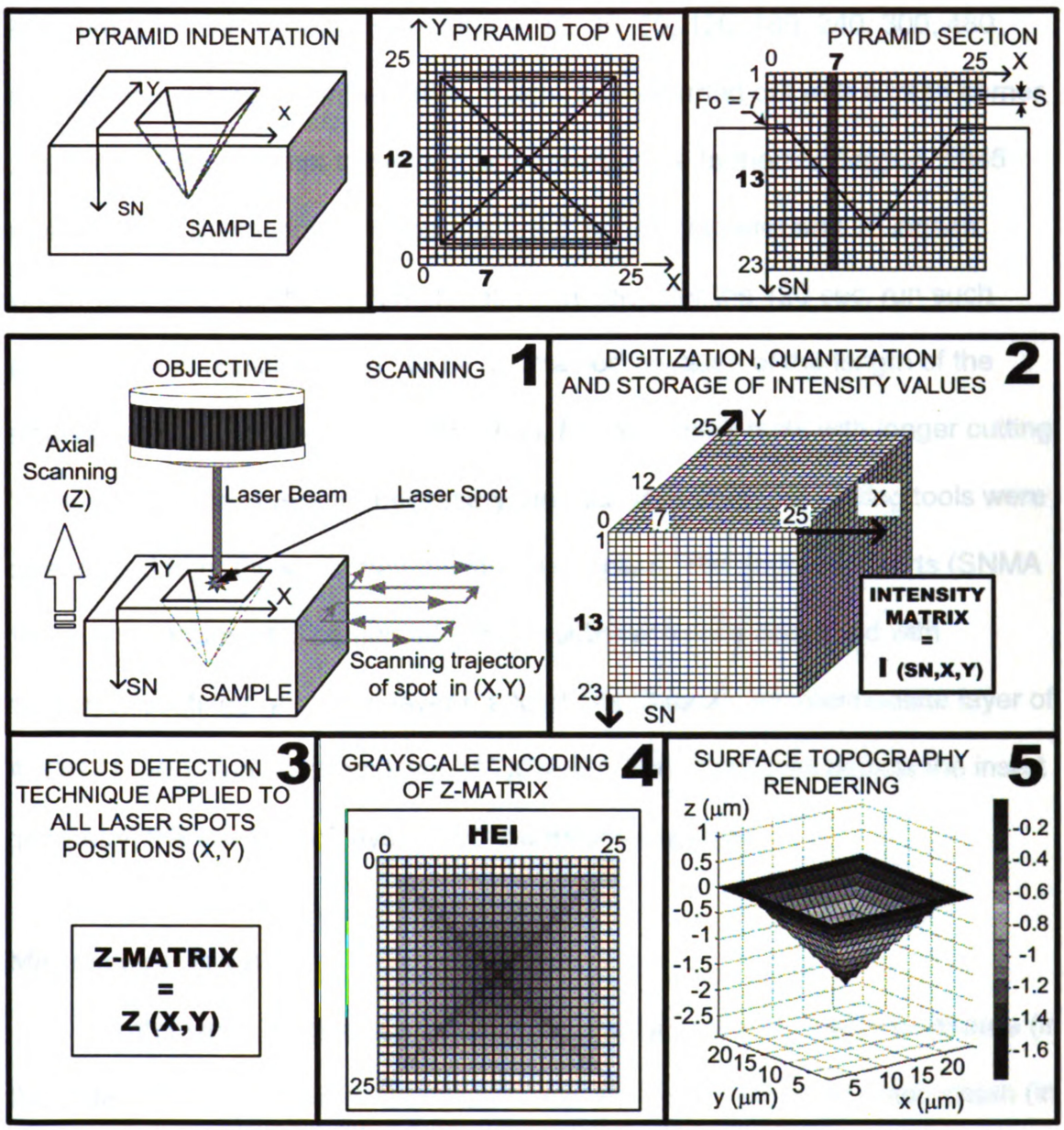

Figure B4 Surface Topography Reconstruction in a CLSM system. Example: pyramid indentation

Experimental Procedure

Machining Tests and Cutting Inserts

To generate the worn tools, dry turning tests were conducted at the constant feed of 0.3175 mm/rev, depth of cut of 1.905 mm, and cutting speed of 250 m/min. Machining was interrupted at 10, 30, 60, 120, 180, 240, 300, 480, and 720 sec. After each interruption, machining is carried out with a fresh corner of an insert in an attempt to prevent any damage due to thermal fatigue. 1045 steel rounded bars whose dimensions are 6 inches diameter and 18 inches length were used as the work material. However, after the 120 sec. run such steady-state conditions could not be maintained because of the length of the steel bar and the reduced diameter. Thus, for the turning tests with longer cutting times, multiple passes were necessary, and subsequently, the cutting tools were disengaged from the work material after each pass. The squared inserts (SNMA 190612-ISO) with a C6 cemented carbide substrate were deposited with multilayer coatings with a top layer made of TiN (3.0μm), an intermediate layer of Al_2O_3 (7.0 μm), and a bottom layer of TiCN (8.6 μm). Figure B5 depicts the insert geometry, the stacking of layers, and the machining times.

Microscope Setup

Crater wear imaging is particularly challenging due to a large worn area (in the order of mm) that has to be imaged, and yet a relatively small crater depth (in the order of microns) has to be considered. A Zeiss LSM 210 confocal microscope was used in a reflection mode to obtain the z-matrices for all of the worn corners in the form of height encoded images (HEIs) and intensity maxima

images (IMIs). The latter are extended-DOF images obtained by the collection of all the intensity-maxima value spots in every pixel position.

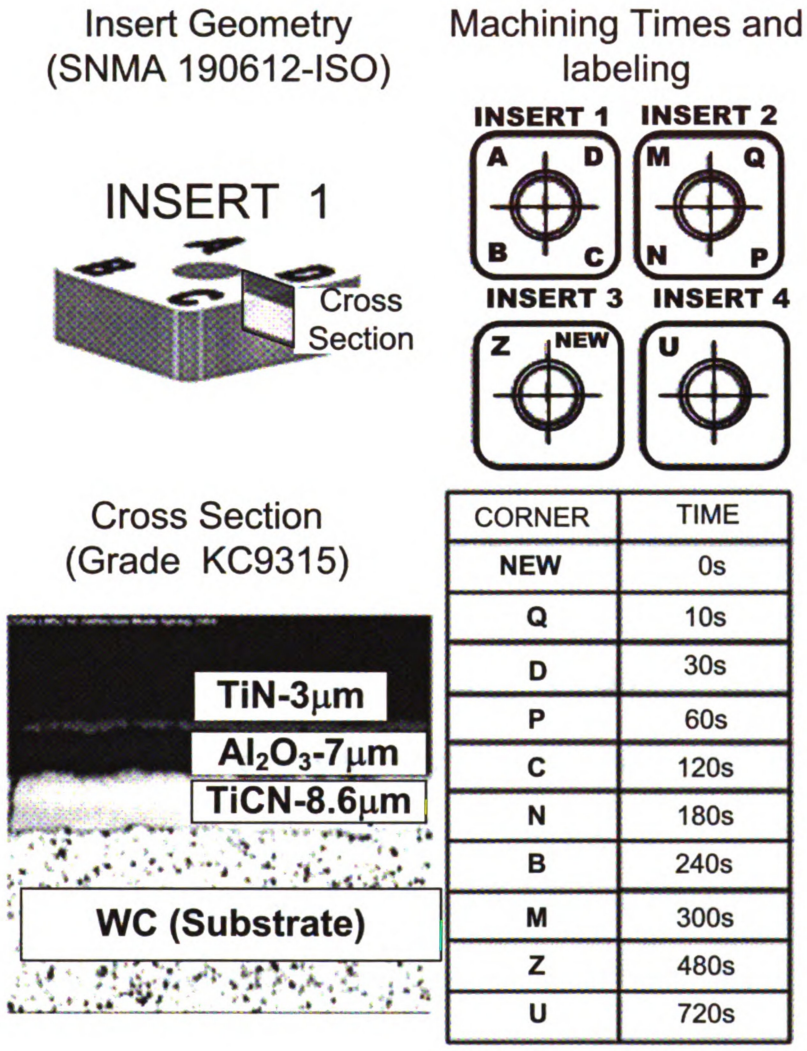

Figure B5 Cutting Inserts and Machining Time

Laser Line Selection

The L488 argon-ion (488 nm) laser at 100% power was selected for better contrast and appearance after optimization via color range indicator. Additionally,

the Ar-ion laser possesses the lowest laser wavelength available so as to obtain the highest resolution [see Eqs. (B-1)–(B-3)].

Measurements Calibration

In general, axial and transversal resolution depends strongly in the detector pinhole size. However, the LSM 210 has a fixed circular pinhole size (15 μm), which stopped further resolution optimization via pinhole adjustment. Calibration in the transversal direction (*x*-*y*) was done using a micrometer slide containing marks of 1000 μm, 100 μm, 50 μm, and 10 μm. In the LSM 210, the accuracy in the axial (*z*) direction depends on both the photomultiplier (PMT) sensitivity and the SS selected. The sensitivity of the PMT depends on the contrast used. The contrast was optimized at the vertical level corresponding to the brightest optical slice aided by the color range indicator. In fact, optimal contrast and brightness values were found at 31 and 395, respectively. The color range indicator allows modifying contrast and brightness so as to avoid saturated and empty pixels. At these values of contrast and brightness, the voltage gain of the PMT, PMT voltage, and PMT sensitivity were 38.4, 116 V, and 0.031, respectively. After the PMT sensitivity is optimized, the final axial (*z*) accuracy in the LSM 210 microscope will only depend on the SS chosen. The selection of the SS will be described in the following section.

Topography Reconstruction Parameter Selection

The lower the SS is, the higher the accuracy in the *z*-direction that can be achieved. However, this limited by the compromise among the minimum SS

selectable, the maximum number of optical sections allowed, and the depth of field (DOF) needed. The DOF is the vertical extension of the *z*-matrix and is obtained by multiplying the SS times the number of sections. The minimum SS and maximum number of sections for the LSM 210 are 50 nm and 200, respectively. Because the total depth of more than 18.6 μm is not expected, a DOF of 20 μm could be enough. However, due to the slopes detected near the corner of the fresh inserts (see Figure B15), the DOF was increased to 35 μm. A SS of 200 nm was chosen along with 200 optical sections, giving a DOF of 40 μm. This SS not only covers the required DOF but allows an accurate imaging of the thinnest coating thickness (TiN-3.0 μm). In Figure B6, the profiles obtained with a stylus profilometer (Dektak 6M –Veeco) and a confocal microscope (LSM 210) are compared. The sample used was the crater developed after 720 sec. of machining time. A 10X objective, with 200 nm SS and 200 optical sections, was used for the confocal topography. For the sake of clarity, the original DOF (200 nm × 200 sections = 40 μm) was reduced to 25 μm in the confocal image.

As it is observed from Figure B6, the confocal profile reveals more surface details than its stylus profiler counterpart, as other works (Gee and McCormick, 1992; Udupa et al. 2000) have previously reported.

Objective Selection

Resolution and field of view (FOV) are always coupled. While higher numerical aperture (NA) apertures and higher magnifications result in improved resolutions, the FOV is reduced. This means that more frames are required to

capture the whole worn area, which increases acquisition times and the possibilities of cumulative errors when merging *z*-matrices.

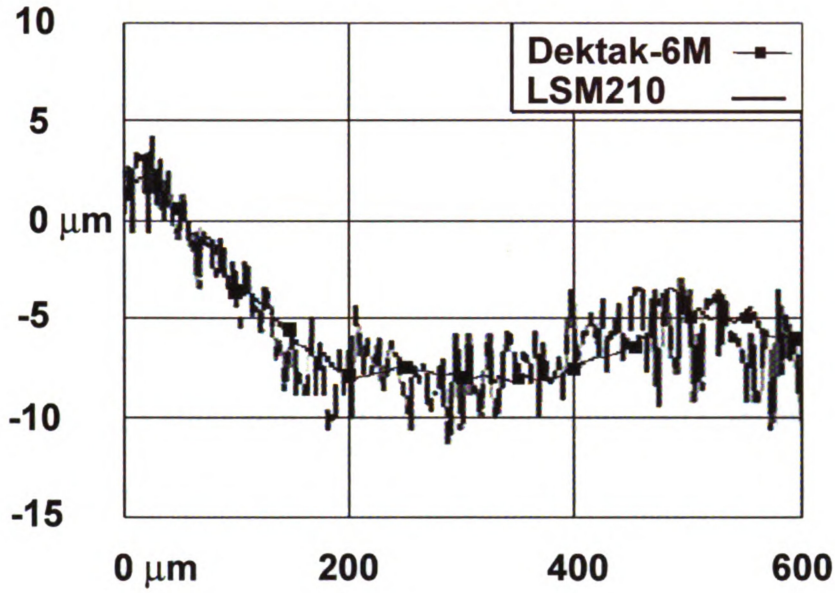

Figure B6 Comparison between stylus profiler and Confocal profile

Three Zeiss Plan-neofluar 5X, 10X, and 20X objectives were tested before collecting the final data. In Table B-1, the performance of these objectives is compared. The normalized values of the pinhole size, as well as axial and vertical theoretical resolution, ($FWHM_{theory}$), were calculated with the following formulae (Wilhelm et al. 2003):

$$PH(in \cdot AU) = \frac{PH(in \cdot \mu m)}{\frac{1.22\lambda(in \cdot \mu m)}{NA}} \quad \text{...(B-1)}$$

$$\left(FWHM_{theory}\right)_{LAT} = \frac{0.51\lambda}{NA^2} \quad \text{...(B-2)}$$

$$\left(FWHM_{theory}\right)_{AX} = \frac{0.88\lambda}{\left(n - \sqrt{n^2 - NA^2}\right)} \quad \text{...(B-3)}$$

where PH represents the pinhole size in Airy units (AU), λ is the laser wavelength, NA is the numerical aperture of the objective, and n is the medium's refractive index between the lens and the surface (n=1 for air). Equations (2) and (3) correspond to geometrical confocality (0.25 AU < PH <1 AU). The experimental axial resolution, $(FWHM_{exp})_{AX}$, was obtained from the actual depth response of each objective, acquired with the z-line function of the LSM 210 and a flat mirror. The 5X objective was used to get an estimate of the extension of the worn area and a preliminary inspection of the crater due to resolution limitations. The worn area extension for all corners covered approximately 1000 × 2000 µm. The 10X objective was found to be a good trade-off between axial resolution and number of z-matrices needed to capture the worn area (Table B-1).

TABLE B-1. Optical properties comparison for the 5x, 10x, and 20x objectives.

Obj.	N.A.	PH (AU)	$(FWHM_{theory})_{AX}$ (µm)	$(FWHM_{exp})_{AX}$ (µm)	$(FWHM_{theory})_{LAT}$ (µm)	F.O.V. (µm x µm)	ZMN
5X	0.15	3.78	37.956	48.0	11.061	2931X1954	1
10X	0.30	7.56	9.323	12.96	2.765	1506X1004	2
20X	0.50	12.6	3.205	4.30	0.995	498X748	6
ZMN : z-matrices needed							

CLSM Data Acquisition

Two z-matrices with an overlap of 50–100 µm were gathered with the 10X objective from the insert corners (Figure B7). The center-of-gravity algorithm was

used for the 10X objective due to its symmetrical and well-shaped experimental depth response (Jordan et al., 1998). The topography information, obtained in the form of two images of 256 × 256 pixels each and combined in a 256 × 512 pixel frame, was stored in the hard disk of the LSM 210 in .PIC format (reserved format owned by Zeiss). These two images are the HEI and the IMI, the former being the picture that carries the *z*-matrix information (Figure B8). Then, these .PIC files were transferred to another computer containing the supporting software of a Zeiss LSM 310 microscope. Here the .PIC images were converted into a .TIF format. Surface topography analysis program was developed in Matlab 7.0 to separate the HEI from the IMI and decode the HEI's grayscale values into height values (z-matrix). This program is also able to merge, filter, and render the z-matrices. During confocal scanning, artifacts can appear due to steep localized regions in the sample. These artifacts are viewed as empty pixels (holes) and spikes in the final surface reconstruction. To overcome this problem, a "spike" filter, which replaces the spikes or the empty pixels with the arithmetic average of the eight local nearby points, was designed. Finally, overlaying of profiles and labeling was done in Adobe Photoshop 8.0.

Layer Identification and Topography Validation

Back-scattered electron (BSE) images and energy dispersive X-ray spectroscopy (EDS) elemental mapping were used to identify the extent of the wear in each of the three layers for all machining times. Atomic force microscopy (AFM) and scanning electron microscopy (SEM) images were used to validate

the topography obtained from the confocal microscope for the cutting tool with 300 sec. machining (see Figure B12).

Figure B9 shows the final rendering of a CLSM topography reconstruction at the corner of the tool with 720 sec. of cutting time. The profiles have the minor cutting edge (MICE) and the main cutting edge (MACE) as references for positioning. The texture mapping function of the Matlab program combined the HEI and IMI provided by the LSM 210 microscope to give a realistic 3-D view of the worn corners (Figure B10). The CLSM topography and texture mapping (realistic 3-D view) revealed a hump starting approximately at 190 μm from the main cutting edge for all machining times between 60 and 300 sec. No detectable evidence of wear was found for the cutting corners with 10 sec. and 30 sec. cutting times. Next to the hump, a growing crater was observed. A thin trench was also discovered in the edge side on the hump.

The BSE images shown in Figure B11 and the EDS elemental mappings for Ti, Al, and Fe shown in Figure B13 indicated that the alumina (Al_2O_3) layer was being exposed in the crater and that the hump was made of TiN. The SEM and AFM images in Figures B12-(A) and B12-(B) showed a good agreement with the CLSM topography. In particular, the AFM reading, which is limited by the size of 77 μm × 77 μm, shows that the crater depth range of the cutting corner with 300 sec. of machining was about 2.5 μm, which agrees with the confocal profiles [see Figure B-14(E)].

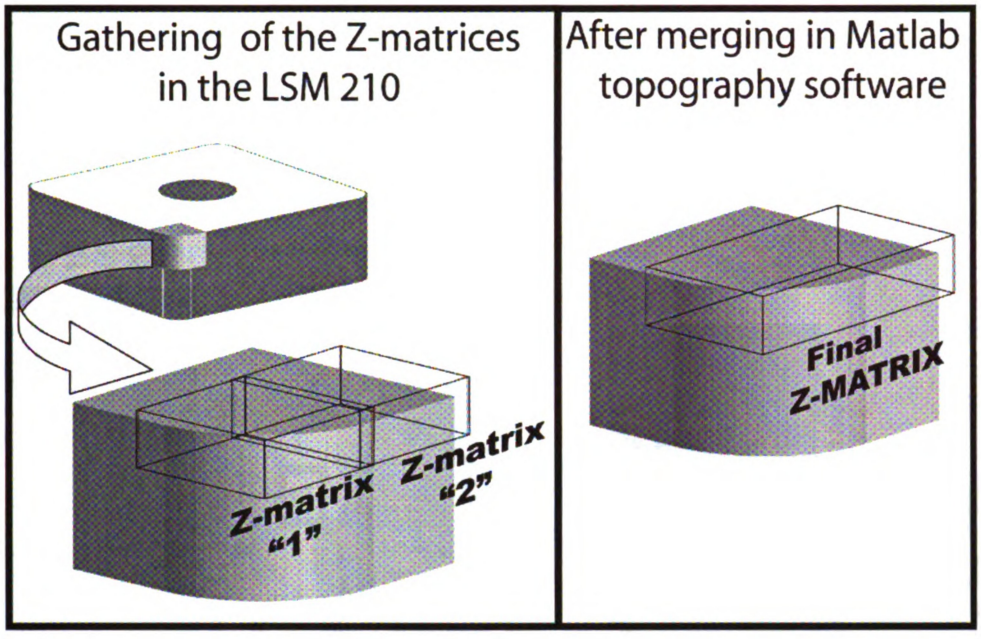

Figure B7 Merging of the z-matrices

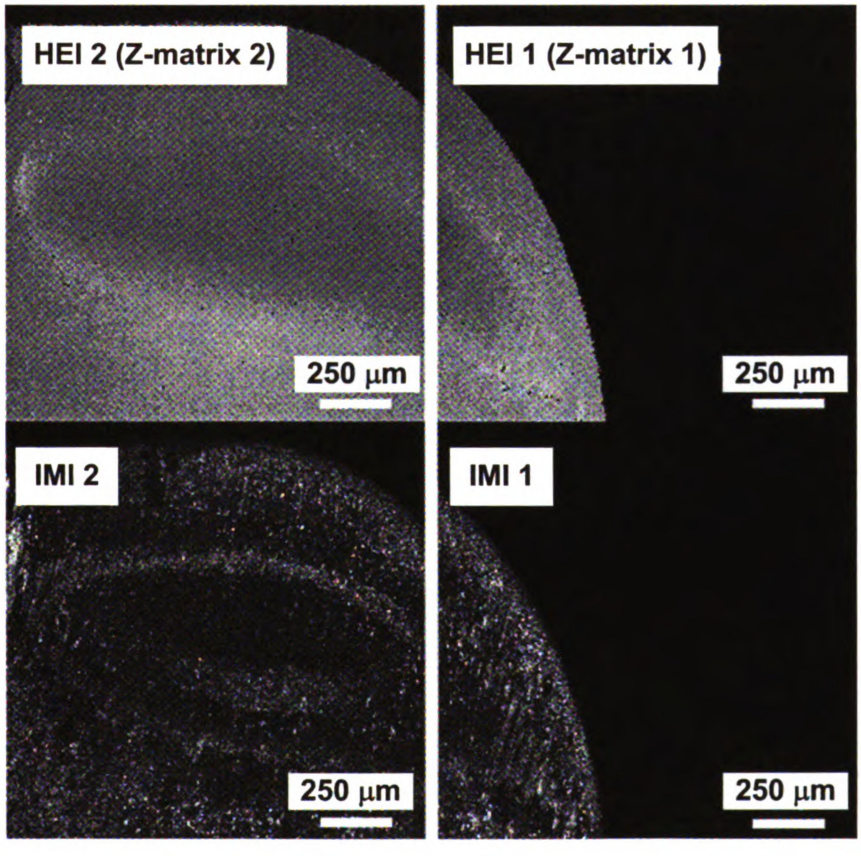

Figure B8 HEIs and IMIs images obtained for the 720s cutting time corner

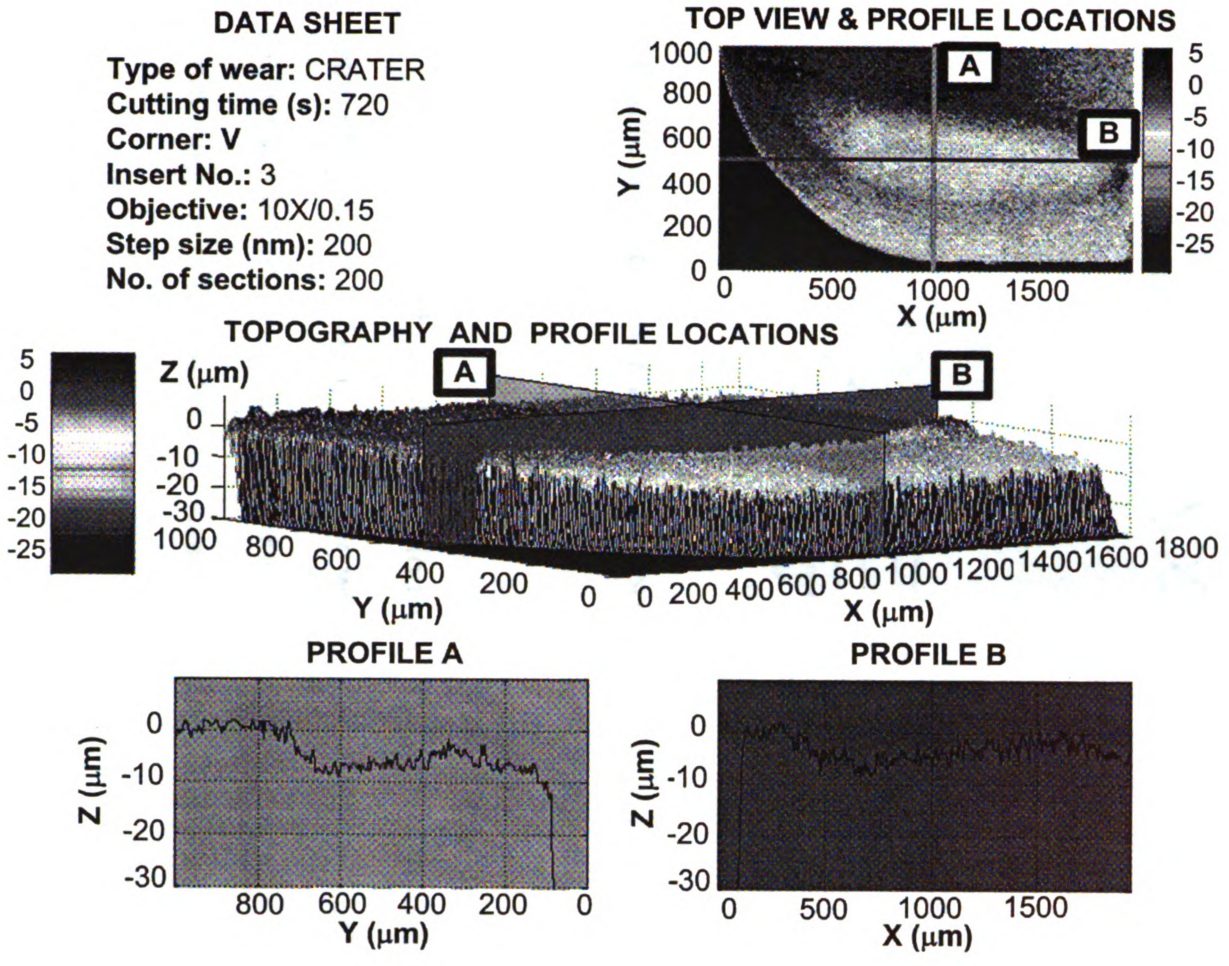

Figure B9 CLSM Surface Topography Reconstruction for 720s cutting time

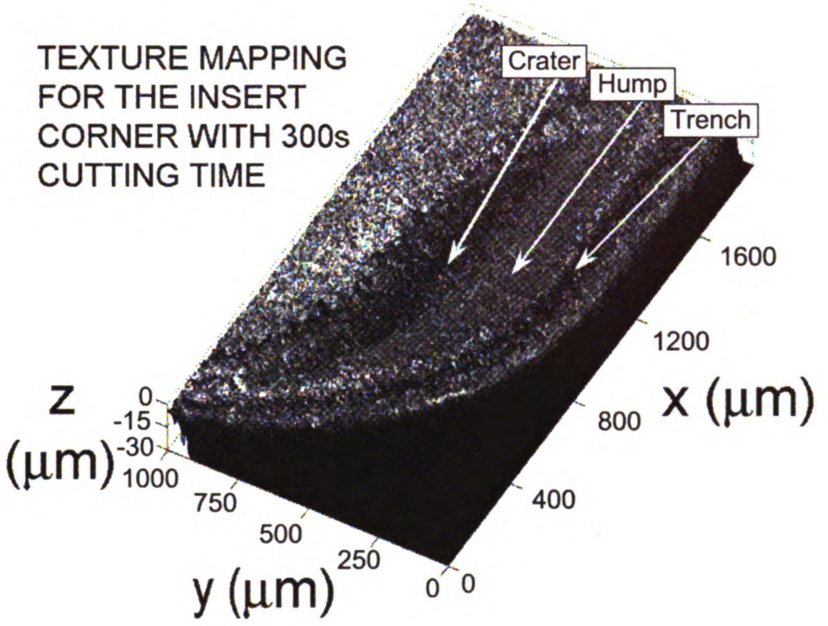

Figure B10 Texture Mapping of Worn Corner with 300s cutting time

Results

Figure B13(B) shows the trench found with CLSM coinciding with a 20–30 μm strip of exposed Al_2O_3 running along with the TiN hump and defining one end of the hump's boundary. Steel, represented by Fe (light shade) in the EDS element mapping of Figure B13(C), was found attached in the very well defined area surrounding the steel-free zone in the center of the crater. The series of EDS images from the corners between 10 sec. and 720 sec. indicates that as more Al_2O_3 was exposed more steel is attached to the Al_2O_3-exposed area. Interestingly, steel did not attach to TiN in the humped zone that is between 200 and 400 μm from the start (S) shown in Figure B14. The TiCN layer was found to be barely reached after 720 sec. cutting time.

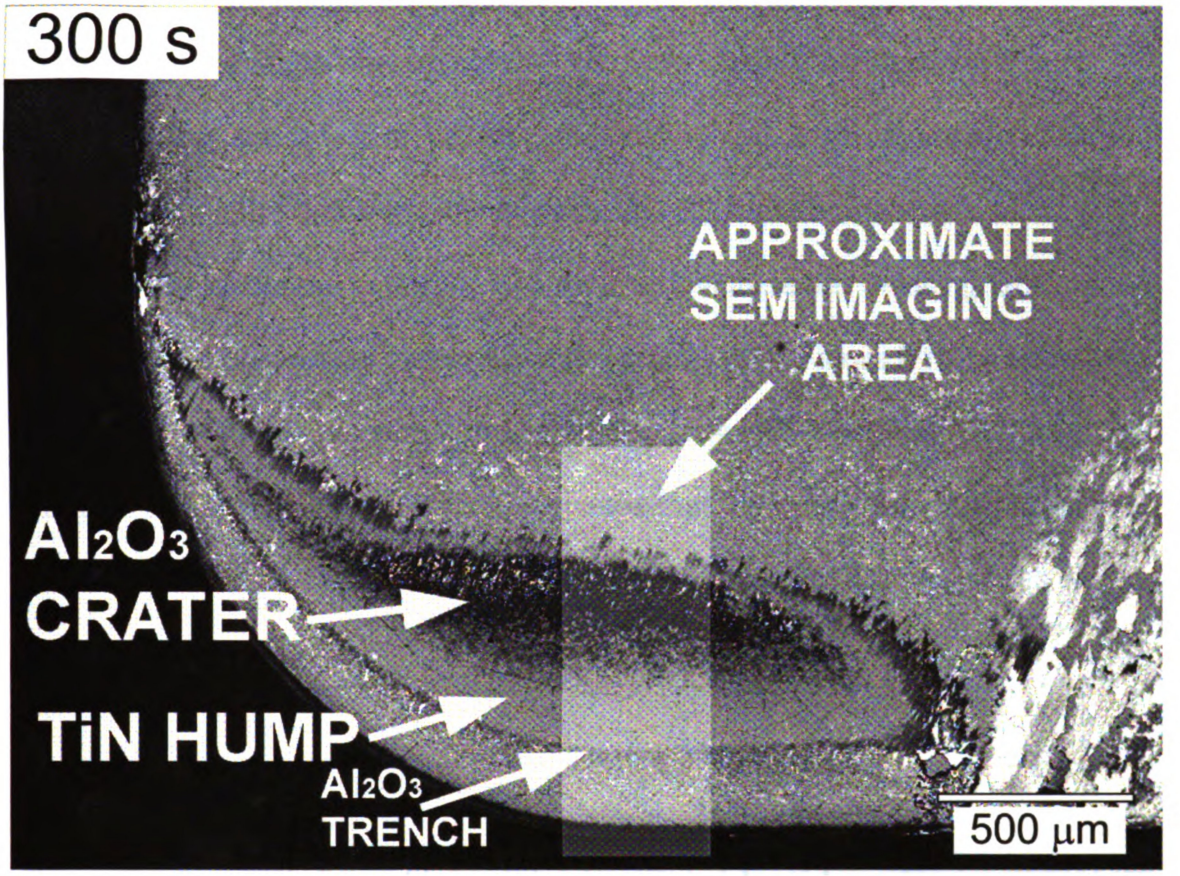

Figure B11 BSE image of corner with 300s cutting time

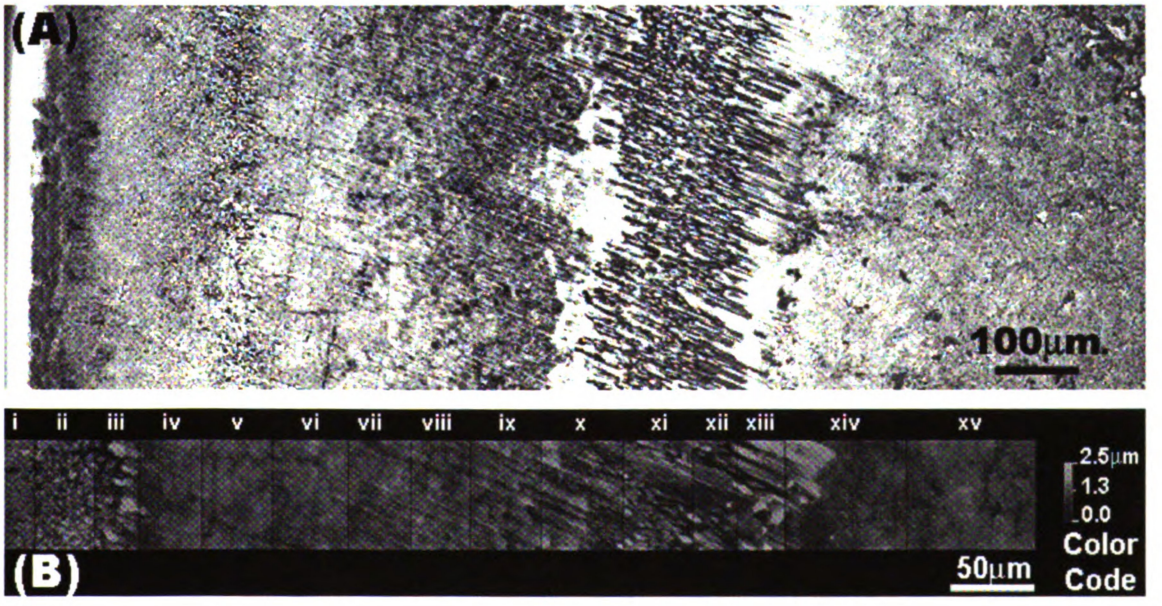

Figure B12 (A) SEM and (B) AFM images for 300 sec. cutting time

With the isolines feature of the LSM 210 built-in software, slight slopes in the rake surface of the unworn corners were discovered, as shown in Figure B15(A). This is consistent on all the corners observed. It was found also that, to clearly discriminate between isoline levels, the SS had to be decreased. However, the decrease in the SS was avoided because the resulting DOF cannot capture the whole vertical extension of the crater wear. Figure B15(B) shows the isoline map of the corner with 720 sec. cutting time with the SS of 150 nm. Even with this 150 nm SS, Figure B15(B) indicates that the entire area P without the area Q has the same maximum depth, which in reality has the roughness of about 2 μm.

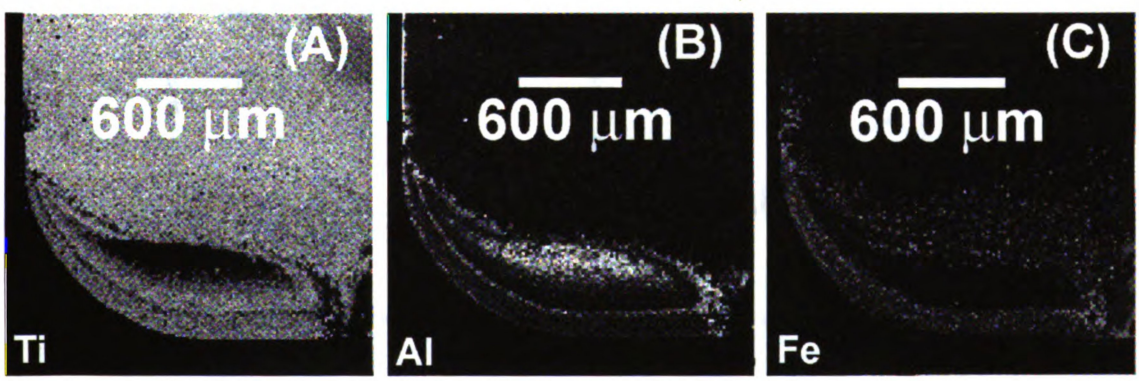

Figure B13 Ti, Al, and Fe EDS Element Mappings for 300 sec. cutting time

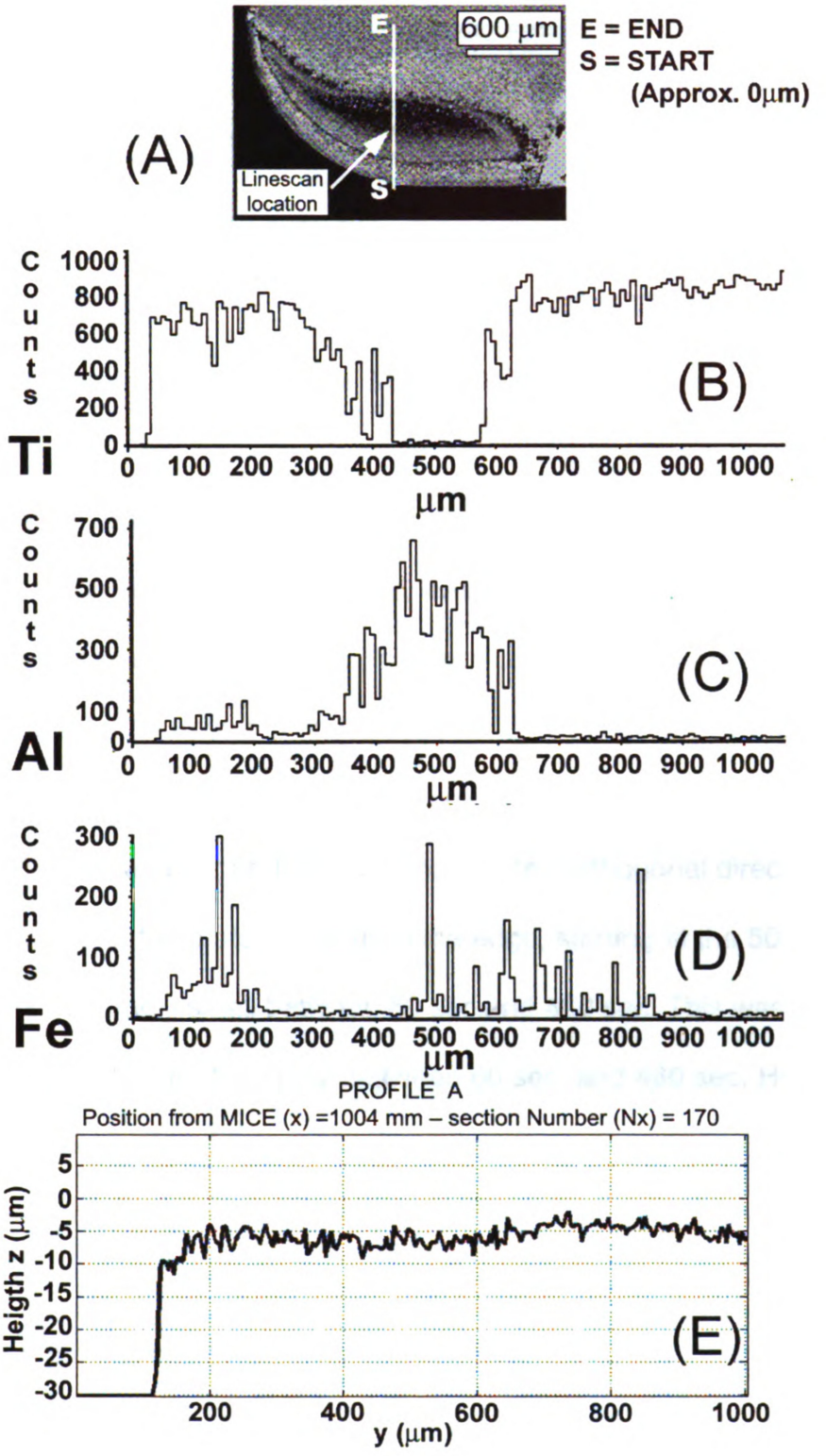

Figure B14 EDS Linescan for 300 sec. cutting time. (A) Linescan location, (B) Ti mapping, (C) Al mapping, (D) Fe mapping, and (E) CLSM profile at a nearby location.

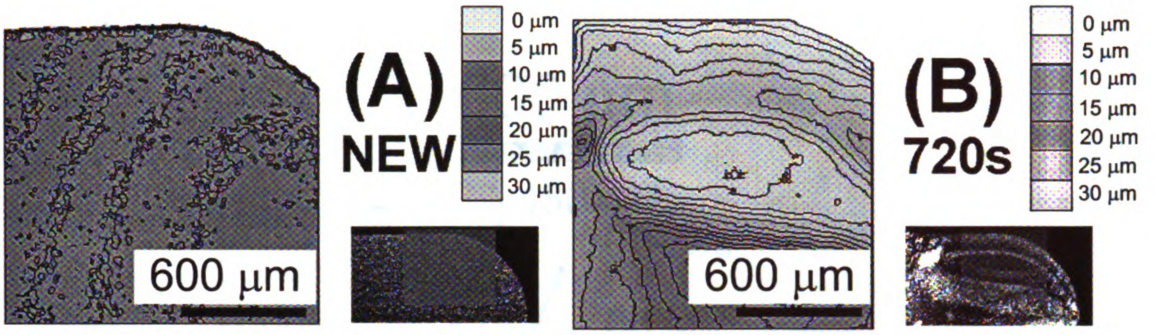

Figure B15 Isolines with 150 nm SS for (A) NEW insert, and (B) 720 sec. cutting time

Therefore, an alternate method, which involved the extraction of the Al_2O_3 exposed area from the Ti EDS dot maps, was used. The area containing no Ti at all supposes to have exposed Al_2O_3. This area contains the maximum crater depth locations (MCDLs) that cannot be resolved by the LSM 210 with 200 nm SS. The Al_2O_3 crater grew toward the cutting edge from a small area at about 500 µm for 60 sec. and expanded much more in the orthogonal direction (Figure B16). The growth of the crater away from the edge, starting at the 500 µm location, was extremely small between 60 sec.and 480 sec. This was seen as a well-defined boundary for the crater between 60 sec. and 480 sec. However, between 480 sec. and 720 sec. this limit was expanded to 620 µm.

A fixed position close to the tangential point at the nose curvature (Sect. No. (Nx) = 170 in Figure B9) was chosen to obtain profiles for all machining times. These profiles were ultimately overlaid to render a wear evolution shown in Figure B17.

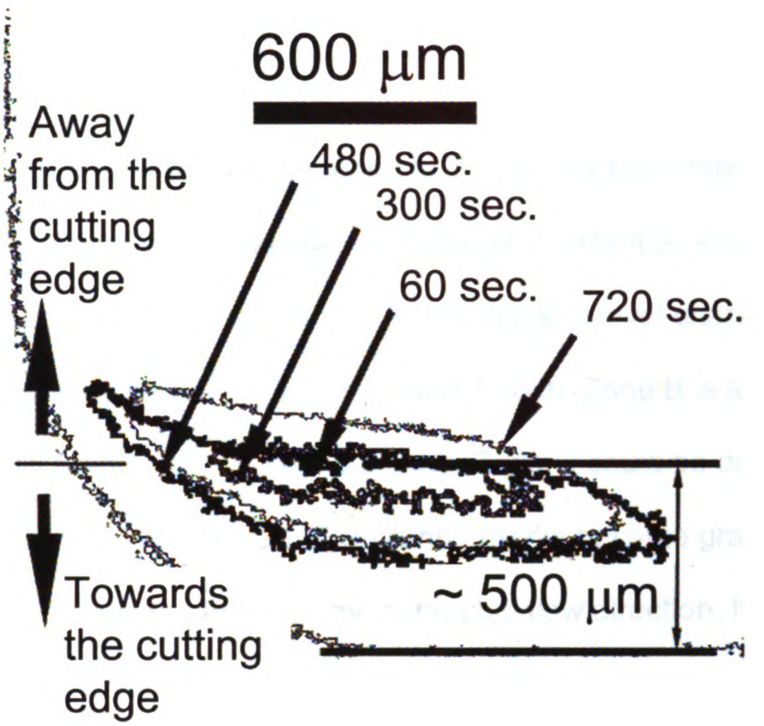

Figure B16 Al_2O_3 Crater Evolution from EDS Mapping of Ti

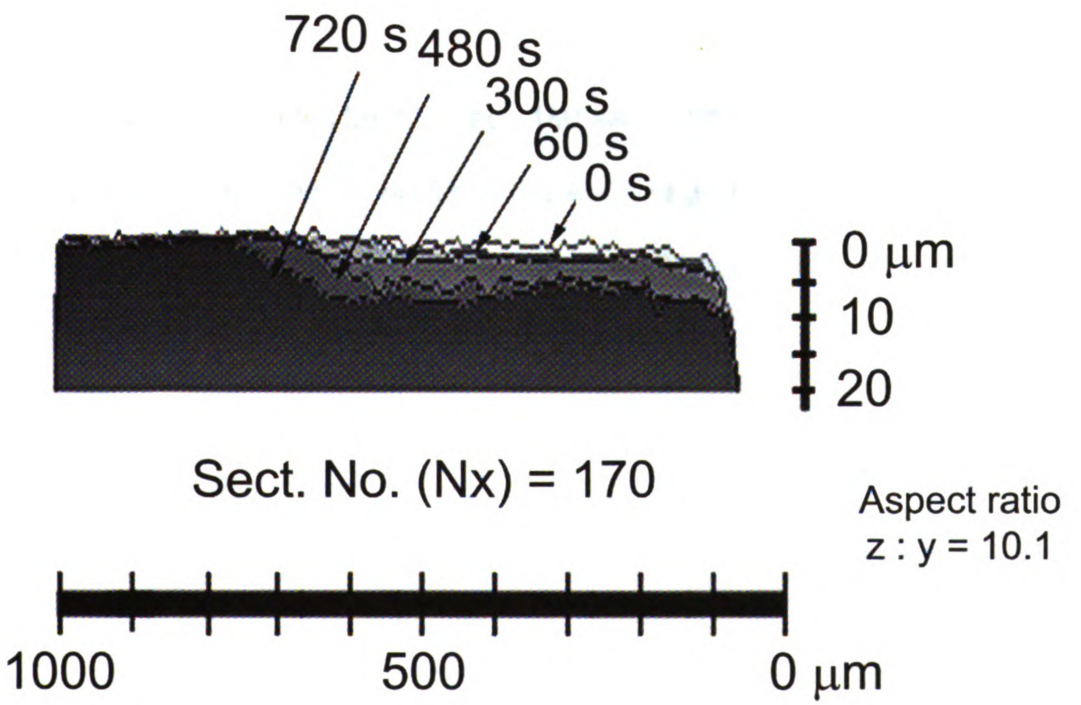

Figure B17 Evolution of Crater Wear Profiles from CLSM Topography

Description of crater zones

The crater wear was divided into six zones for a better description (Figure B18). Zone A is an area with steel attached to TiN, no scoring marks [Figures B11(A)and B11(B)], and width that stays somewhat constant at about 200 μm from 30 sec. to 300 sec. Figures B11 and B16 suggest a level change when going from zone A to B coinciding with the Al_2O_3 trench. Zone B is a TiN zone with slight scoring marks and no steel attached. Zone C could be defined as a zone of transition from TiN to Al_2O_3. The scoring marks become gradually stronger and the Ti detected fades away in the chip flow direction. No steel is attached to zone C, which is mainly composed of TiN. Zone D is the alumina layer with steel attached. It can be inferred from Figure B17 that the MCDLs are contained here.

The wear profiles for 120 sec., 180 sec., and 240 sec. did not differ much in height from the 300 sec. profile in the Al_2O_3 region; thus, they are not shown in Figure B17. The conclusion that can be drawn from this is that crater wear is "nearly stopped" at the Al_2O_3 layer and spread out into the TiN layer. A shallow region of steel in strong concentration attached to Al_2O_3 distinguishes zone E. No scoring marks were found in zone F, but steel is adhered to TiN (zone F).

The adhesion of steel and the absence of scoring marks in zone A seem to indicate the presence of a stagnant zone of steel at the edge (Kim and Kwon, 2001). The intermediate layer, Al_2O_3, shows a low thermal conductivity compared to TiN and TiCN between 120°C and 1320°C (Grzesik and Nieslony, 2003).

When compared to AISI 1045 steel, Al_2O_3 is a poor heat conductor independent of temperature.

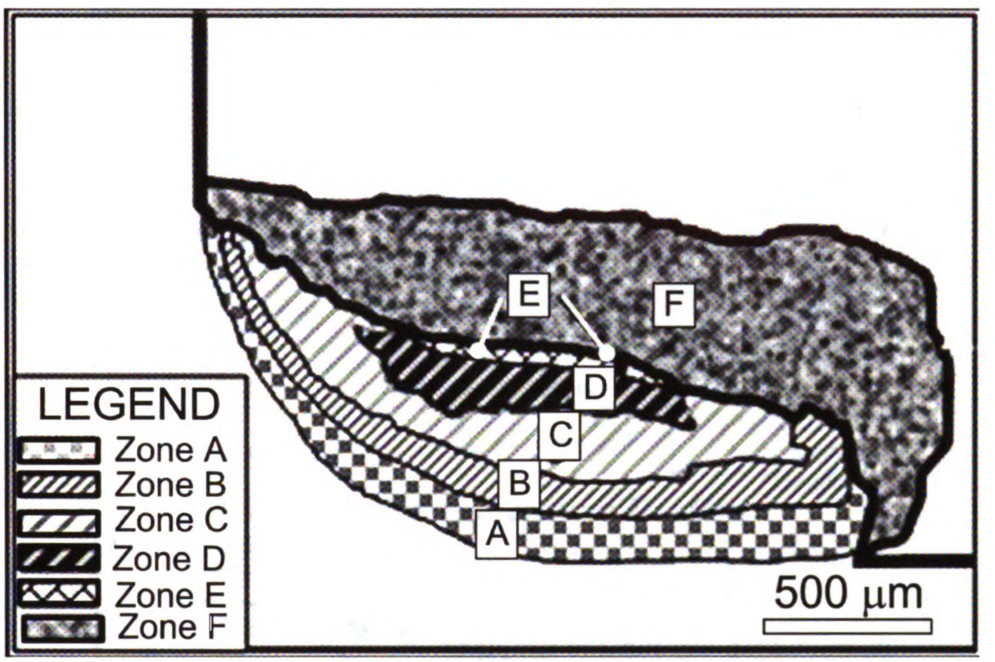

Figure B18 Zones of the Worn Face

This heat-flow barrier posed by alumina could result in a heat partition more to the chip (Grzesik and Nieslony, 2003; Attia and Kops, 2004) causing an overall drop in interface temperature with respect to the uncoated carbide case. The interface temperature may decrease as much as 150°C with multilayer coated carbides (TiC/TiCN/Al_2O_3/TiN) compared to the uncoated insert (Grzesik and Nieslony, 2003).This drop in the rake temperature can help to slow down the wear rate. Additionally, in an FEM simulation for multilayer coated carbides (TiN/ Al_2O_3/ TiCN) considering this barrier effect, a highly localized temperature shifted away from the maximum temperature location for uncoated carbides has been also found (Attia and Kops 2004).

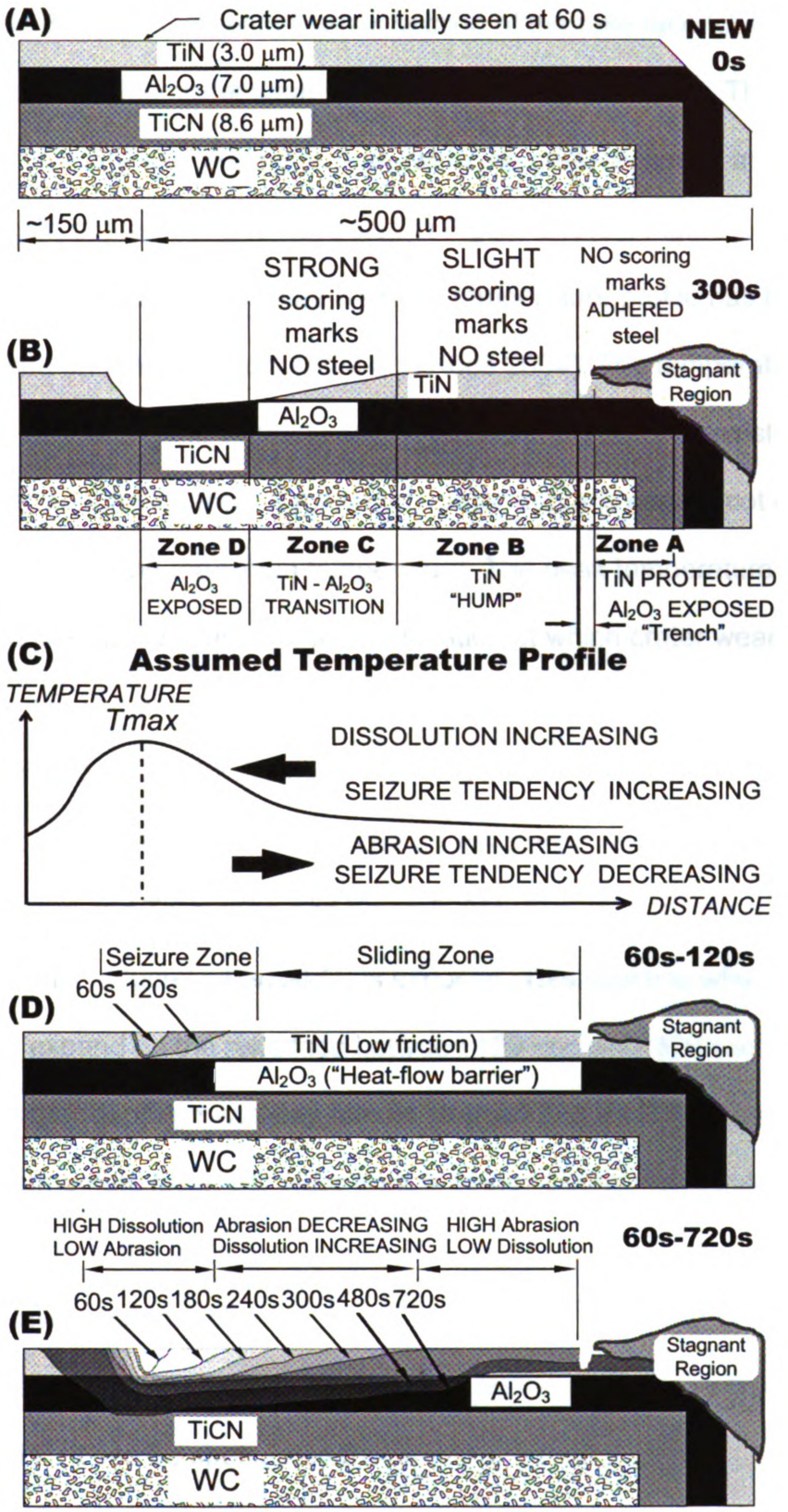

Figure B19 Discussion of Crater Wear Evolution – Not scaled horizontally

Figure B19(A) represents a cross section of the rake face for a new insert with the location where crater wear is first seen on the worn tools. The rake-face cross section for 300 sec. cutting time showing the analysis zones and the stagnant region at the MACE is illustrated in Figure B19(B). Figure B19(C) shows the expected temperature profile as a similar temperature profile has been attained based on the FEM work (Attia and Kops 2004). The temperature is expected to vary within the contact zone. A temperature gradient exists at the contact zone; and the location of maximum crater depth is near, if not coincides with, the location of the maximum temperature. The peak temperature position constitutes a possible explanation for the location at which crater wear initiates [Figure B19(A)]. The temperature distribution can also help explain the crater expansion toward the MACE from a fixed initial position (Figure B15).

Provided that Al_2O_3 has a much better resistance against dissolution wear compared to TiN and TiCN (Kim and Kwon 2001) (Figure B20), the crater growth rate is drastically reduced when Al_2O_3 is exposed. This explains why the crater continued to expand on the rake face between 120 sec. and 300 sec. (Figure B16) while crater depth growth was almost stopped [Figure B19(E)]. With a wear-resistant intermediate layer, the wear front is trying to progress into a much bigger area. This is the main reason why MLCCTs resist tool wear much more than single-layer coated tools.

As steel does not attach to TiN in zones B and C but sticks to Al_2O_3 in zones D and E, it can be speculated that B and C constitute the sliding zone of the contact, while D and E are the sticking zone. The low TiN-steel friction

coefficient and a temperature profile decreasing from the peak temperature toward the cutting edge can be responsible for this behavior. Under these assumptions, a small seizure contact length (about 50–100 μm) could be proposed between 10 sec. and 120 sec. cutting times [Figure B19(D)].

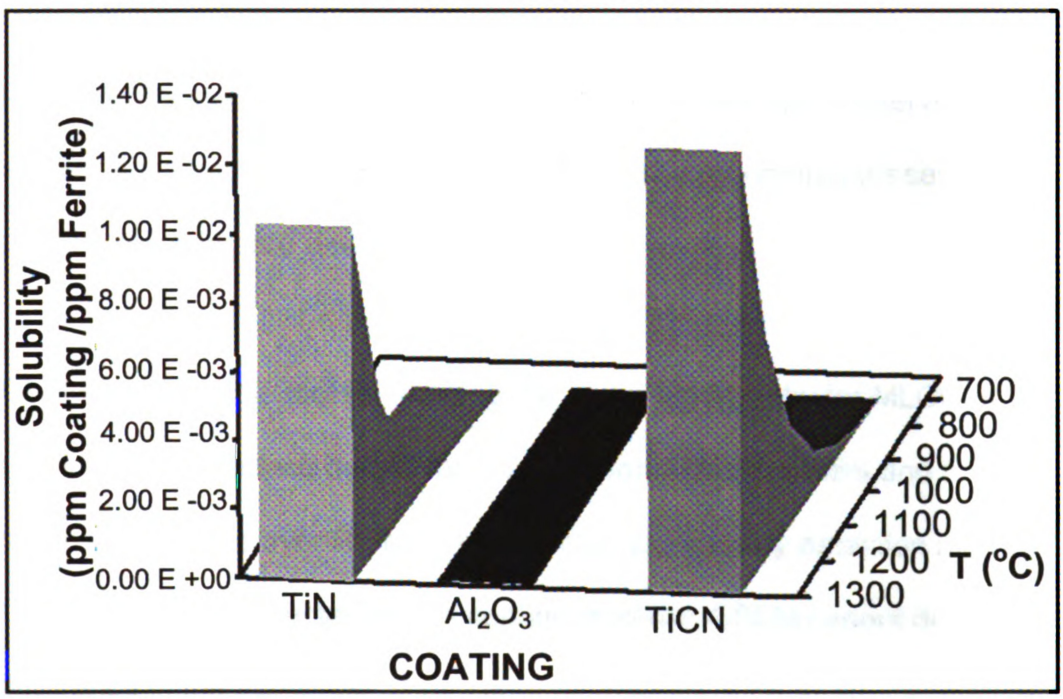

Figure 54 Solubility of Coatings in Iron

The presence of scoring marks, which gradually increase in intensity going from zone B to zone C, points to an abrasive wear mechanism. Knowing that the Fe_3C (cementite) inclusions of the steel only withstand a very short transient heating (Kwon 2000), abrasion of TiN and Al_2O_3 by cementite inclusions is highly probable in zones B, C, and D. TiN possesses higher hardness than Al_2O_3 until about 850°C (Paldey and Deevi, 2003); therefore, abrasion of Al_2O_3 by TiN debris is also possible in zone C. The assumption of a stagnant region in zone A

enhances the possibilities for a three-body abrasion scenario in zones B and C as the work material with hard inclusions extrudes out of the stagnant region. No evidence of wear was encountered in zone F. Thus, zone F it is suspected to be a re-deposition zone for steel.

Conclusions

The topography evolution of crater wear in MLCCTs has been observed using confocal laser scanning microscopy (CLSM). With the experiments presented in this paper, the following are deduced:

- CLSM is a valuable tool for imaging the crater topography for MLCCTs. It provides more surface details than conventional profilometers and has some advantages over RLIM. While surface topography detection in CLSM will not be affected by the coating material, CSLM cannot detect the difference in the materials. Thus, other techniques such as BSE and EDS are needed to differentiate coating materials in MLCCTs.

- The delamination in the coatings of MLCCTs observed in a previous work (Cho and Komvopolous, 1997) was not observed in the MLCCTs despite of the fact that similar machining conditions have been employed. This study indicates that the multilayer coating studied resists crater wear mainly because of the obstruction of depth growth by means of a second layer (Al_2O_3) with a low dissolution potential into steel.

- Other factors such as (i) a possible drop on the interface temperature with respect to uncoated carbides due to a heat-flow barrier provided by a low-conductivity intermediate layer (Al_2O_3), and (ii) the initial delay of dissolution wear onset due to a small seizure region as a result of a low-friction top layer (TiN), may contribute to the wear resistance of the multilayer coating.

- Finally, the stacking sequence and layer thickness are important factors in the design of a MLCCT. Gradual tool wear is the contribution of various wear mechanisms such as abrasion and dissolution. As shown with single-layer coated tools (Wong and Kwon, 2006), TiCN is the most abrasive-resistant coating, while alumina is the most dissolution-resistant coating. With single-layer, coated tools, the coating can provide resistance to one of the wear mechanisms. When each coating material is combined as multilayer coated tools, the overall resistance to tool wear of multilayer coated tools is much more than summing the wear resistance of individual layers. In the present study, because of the dissolution wear resistance of the alumina layer, the progress of crater wear is delayed in depth as a wider area of TiN is being worn.

APPENDIX C: Wavelets Basic Theory

One Dimensional (1D) Wavelet Analysis

A wavelet can be understood as a pulse function capable of dilating to different scales and shifting to different positions. Mathematically, the analyzing or mother wavelet is expressed as

$$\psi_{a,b}(x) = \frac{1}{\sqrt{a}}\psi\left(\frac{x-b}{a}\right) \quad \text{...(C-1)}$$

where "a" is the scaling parameter and "b" is the shifting parameter. By applying different values to "a" and "b", dilated and shifted versions of the mother wavelet, i.e. children wavelets, are obtained. The continuous 1-D wavelet transform (CWT) of an arbitrary function $f(x)$ can be written as

$$CWT_{1D}\{f(x)\} = C(a,b) = \frac{1}{\sqrt{a}}\int_{-\infty}^{+\infty} f(x)\cdot\psi\left(\frac{x-b}{a}\right)\cdot dx \quad \text{...(C-2)}$$

where $C(a,b)$ are called the wavelet coefficients. If the correlation of the function $f(x)$ and the mother wavelet $\psi_{a,b}(x)$ at position b and scale a is strong then the associated coefficient $C(a,b)$ presents a large value. The converse leads to a small or zero value for $C(a,b)$. In surface analysis $f(x)$ represents a profile of the surface, i.e. a 2D surface topography representation. The CWT provides a mathematical frame wherein the mother wavelet can be

explicitly seen; however, its implementation involves too many redundant calculations. The integral in Equation (C-2) can be evaluated for discrete values of a and b (dyadic scaling) in which case the transform is called a Discrete Wavelet Transform (DWT) and is given by

$$DWT_{1D}\{s(x)\} = C^D(a,b) = \frac{1}{\sqrt{a}} \int_{-\infty}^{+\infty} s(x) \cdot \psi\left(\frac{x-b}{a}\right) \cdot dx \quad \text{...(C-3)}$$

For $a = 2^j$, $b = k \cdot 2^j$, where j and k are integers . $C^D(a,b)$ are the wavelet coefficients obtained when the one-dimensional DWT, is calculated. Wavelets are generally use to extract very small details of the surface leaving the task of recording the large scale features to another function called the scaling function (Fu et al., 2003) defined as

$$\phi_{a,b} = \frac{1}{\sqrt{a}} \phi\left(\frac{x-b}{a}\right) \quad \text{...(C-4)}$$

Several types of wavelets and their scaling functions counterparts are available for the CWT (Morlet, Mexican hat, etc.) and also for the DWT (Haar, Daubechies, etc.). In Figure C1, the Daubechies20 ('db20') wavelet and its correspondent scaling function are presented as an illustration. The equations below represent the discrete versions of the wavelet and scaling functions as they are used in the computations.

$$\psi_{j,k}(x) = 2^{j/2} \cdot \psi\left(2^j x - k\right) \quad \text{...(C-5)}$$

$$\phi_{j,k}(x) = 2^{j/2} \cdot \phi\left(2^j x - k\right) \quad \text{...(C-6)}$$

where j and k are the integers which define the scale and position, respectively.

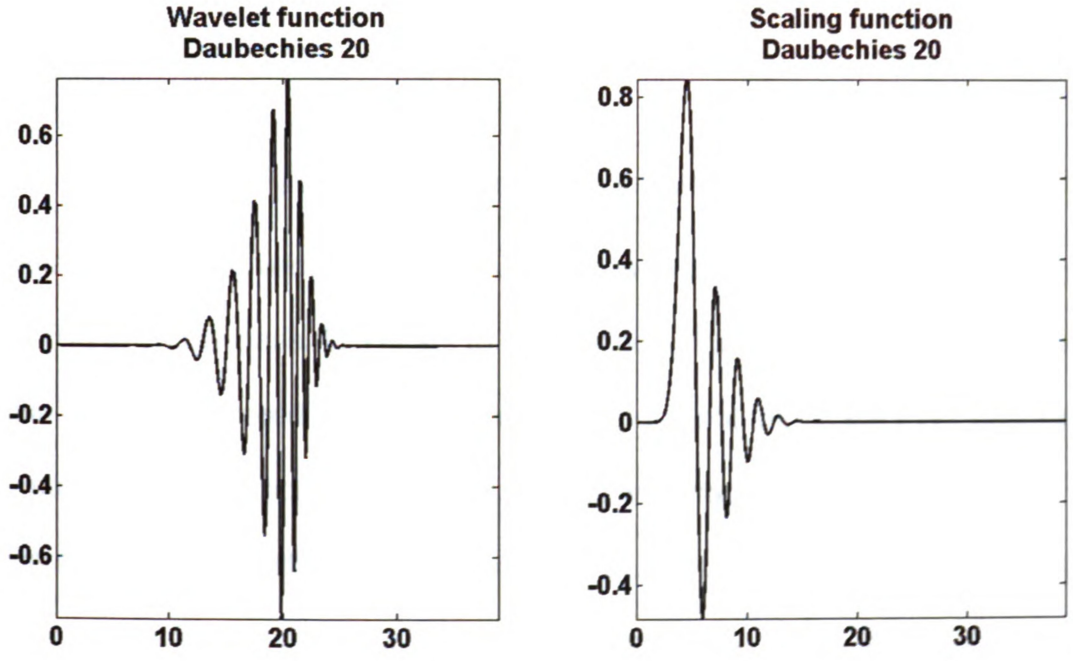

Figure C1 Wavelet and scaling functions for Daubechies 20 (db20) family

In practice, Equation (C-3) is replaced by a scheme known as the Fast Wavelet Transform (FWT) algorithm (Mallat, 1989). The FWT algorithm consists in a classical scheme known as two-channel sub-band coder which takes advantage of the so-called twin-scale property of orthogonal wavelets (MATLAB 7.0 help files). According to this property both the wavelet (ψ) and the scaling function (ϕ) can be expressed as linear combinations of double resolution copies of themselves via the series expansions (Gonzalez et. al., 2004):

$$\psi(x)=\sum_{n} h_{\psi}(n)\sqrt{2}\psi(2x-n) \quad \text{...(C-7)}$$

$$\phi(x)=\sum_{n} h_{\phi}(n)\sqrt{2}\phi(2x-n) \quad \text{...(C-8)}$$

where $h_{\psi}(n)$ and $h_{\phi}(n)$, the expansion coefficients , are now known as wavelet and scaling vectors, respectively. These vectors can be viewed as High-pass (Hi) and Low-pass (Lo) filters to be applied to the surface data in order to obtain a wavelet-filtered output. It is crucial to point out that in the FWT neither the mother wavelets nor the scaling functions are used explicitly in the computations but only their associated Hi and Lo filters (Gonzalez et. al., 2004). The Hi and Lo filters represent in fact four filters two for decomposition (analysis) and two for reconstruction (synthesis). The High-pass Decomposition (HiD) and Low-pass Decomposition (LoD) filters are generated starting with the scaling function, ϕ , in turn, HiD and LoD generate the High-pass Reconstruction (HiR) and Low-pass Reconstruction (LoR) just by flipping their directions and ensuring that the condition for quadrature mirror filters is met (MATLAB 7.0 help files, 2007)

$$HiR(k)=(-1)\cdot k\cdot LoR(2N+1-k) \text{ for } k=1,2,...2N \quad \text{...(C-9)}$$

where N is the length of the scaling vector ϕ. As a consequence of Equation (C-9), it turns out that HiD and LoD are themselves quadrature mirror filters to each other provided that they are flipped versions of HiR and LoR.

The FWT is usually implemented in a multiresolution fashion, i.e., the original data is filtered in a first stage or level where fine features ("details") are separated from coarse features ("approximations"), then in a second level the approximation from the previous level is again separated into "details" and "approximations". This process, known as the wavelet Multi-resolution analysis (MRA), can continue until the scale of the "details" extracted is comparable to that of the size of the data. The 1D wavelet MRA implementation for a 2D topography data set ($f(x)$) for the first level (j+1=1) is shown in Figure C2. The dyadic decimation is indicated as downsampling by two and the boxes containing the filters (Figure C2) imply a convolution of $f(x)$ with the indicated filter. In Figure C2, cA_1 and cD_1 are the approximation and details wavelet coefficients obtained after filtering and decimation. It is evident from Figure C2 that $f(x) = A_0$, i.e. the original 2D surface topography data can be viewed as the wavelet approximation at the zeroth level.

It is important to recognize at this point that the reconstruction step applied for the full recovery of the original signal in Figure C2, fulfills a mathematical requirement for filters in signal analysis.

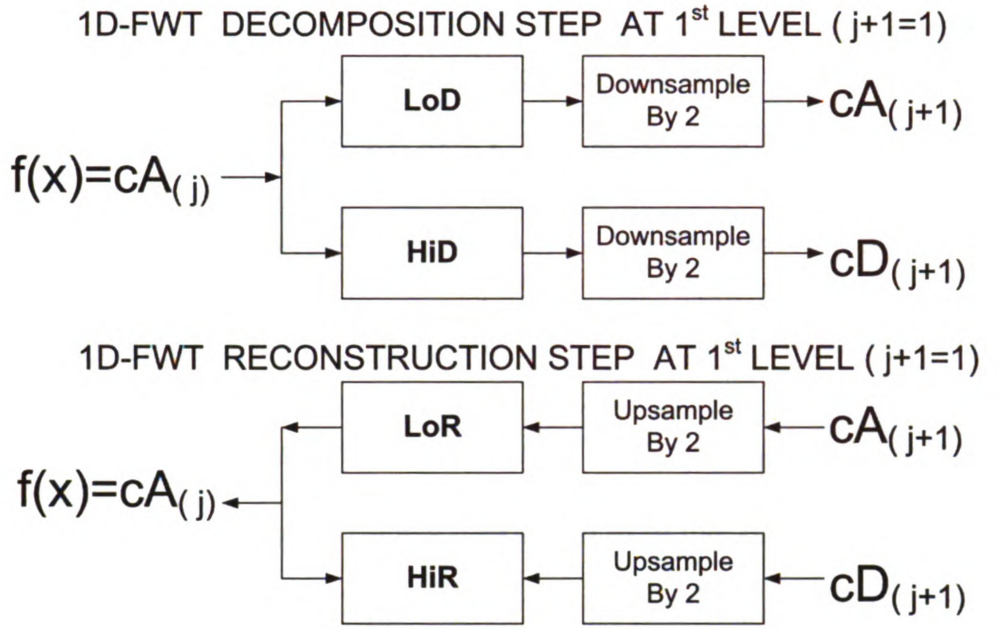

f(x) : 2D Surface Topography (Profile) from Instrument

Figure C2 Decomposition and reconstruction steps using the 1D-FWT algorithm

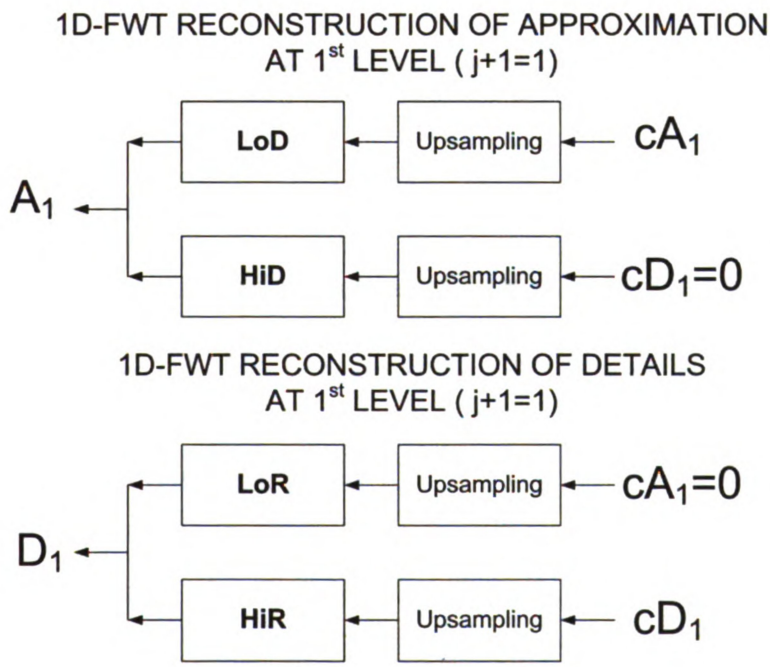

Figure C3 Independent reconstruction of the Approximation and Details

In our application, it seems to be useless decompose a data set into coefficients representing the large scale features and small scale features just to convert them back into the original data set. Here, another advantage of wavelets analysis over Fourier analysis is pointed out, the coefficients cA_1 and cD_1 can be reconstructed separately to obtain A_1 and D_1 (Figure C3) without loosing the localization of the small and large features. A_1 and D_1 constitute the approximation surface and its details decoupled from the 2D topography surface $f(x)$. It clearly follows that

$$f(x) = A_0 = A_1 + D_1 \quad \text{...(C-10)}$$

Upsampling implies zero-padding the coefficients data set to complete the original grid lost by the process of downsampling.

Two Dimensional (2D) Wavelets Analysis

3D surface topography data sets contain the height (z) as a function of two spatial coordinates (x, y); consequently a 2D version of the wavelet transform is needed. Analogous to the 1D-CWT for a function $f(x)$ there exists a 2D-CWT version of a of a given function $f(x,y)$ defined by

$$C_{b,a}(x,y) = \frac{1}{\sqrt{a_x a_y}} \int_{-\infty}^{\infty} f(x,y) \cdot \psi\left(\frac{x-b_x}{a_x}, \frac{y-b_y}{a_y}\right) dxdy \quad \text{...(C-11)}$$

where a_x and a_y are the scaling parameters and b_x and b_y are the shift coefficients in x and y, respectively. Similar to the 1D development a two dimensional discrete wavelet transform (2D-DWT) can be proposed using dyadic decimation and ultimately the 2D-FWT using Mallat's algorithm (1989) can be adapted. However, the implementation of 2D-CWT requires one previous additional step which includes the usage of three separate 2D wavelet functions and one 2D scaling function obtained as products of 1D wavelet and scaling functions

$$\psi^H(x,y)=\psi(x)\cdot\phi(y) \quad \text{...(C-12a)}$$

$$\psi^V(x,y)=\phi(x)\cdot\psi(y) \quad \text{...(C-12b)}$$

$$\psi^D(x,y)=\psi(x)\cdot\psi(y) \quad \text{...(C-12c)}$$

$$\phi(x,y)=\phi(x)\cdot\phi(y) \quad \text{...(C-13)}$$

where $\psi^H(x,y)$, $\psi^V(x,y)$, $\psi^D(x,y)$ are the horizontal, vertical and diagonal wavelets. $\phi(x,y)$ is a scaling 2D function. The discretized counterparts of these wavelet and scaling functions have been already shown in Equations (C-5) and (C-6). Finally, HiD, LoD, HiR, and LoR filters for ψ and ϕ are obtained by the same scheme used in Equations (C-7) and (C-8), but the implementation is done in a slightly different manner. Figure C4 presents the Decomposition and Reconstruction steps using the 2D-FWT

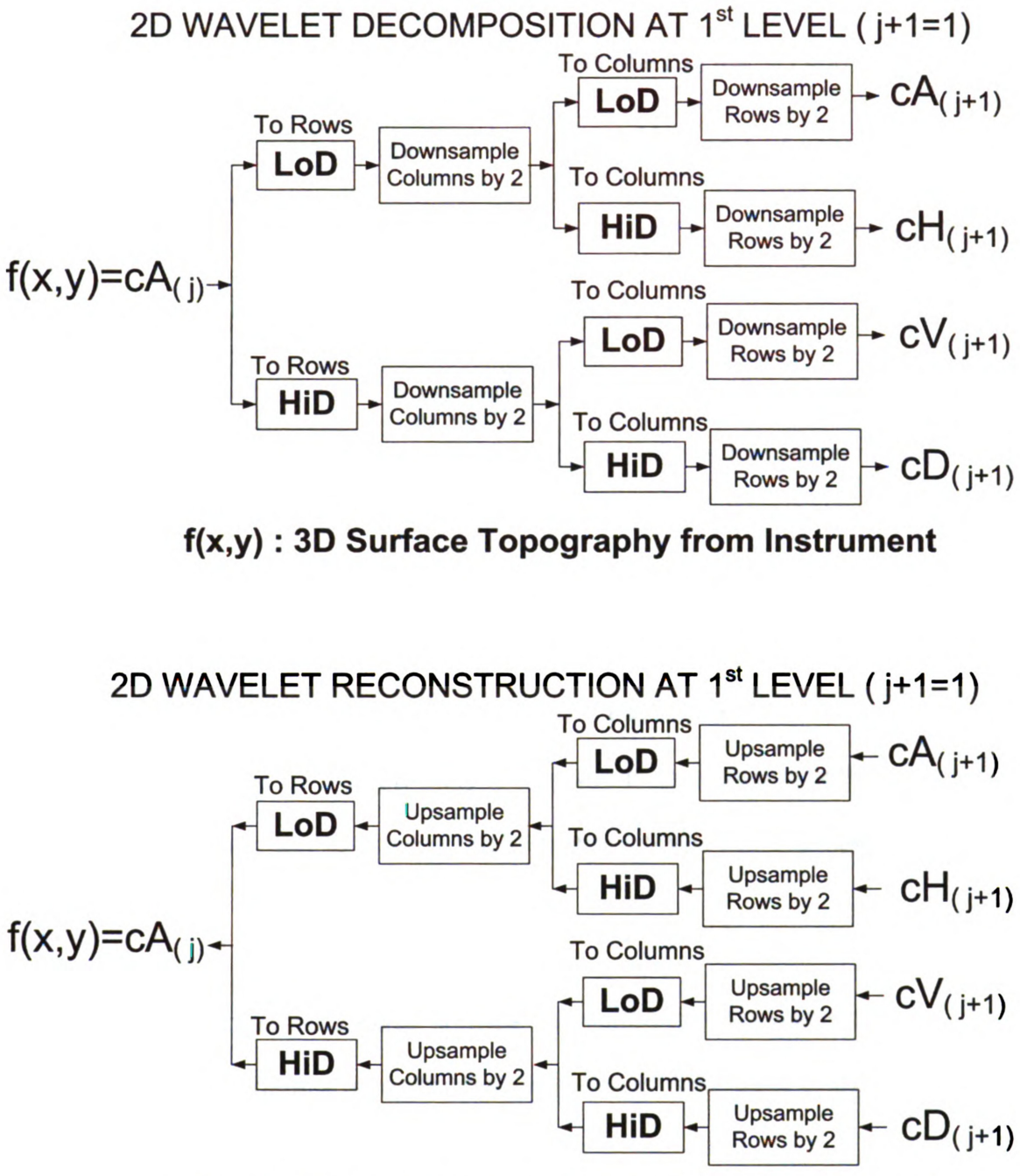

Figure C4 Decomposition and reconstruction steps using MRA at the 1st level

MRA in the 2D-FWT case is achieved by applying Mallat's algorithm recursively to a given data set, e.g. apply the 2D-FWT to the 3D surface topography data $f(x,y)$ to obtain cA_1, cH_1, cV_1, and cD_1, then re-apply Mallat's algorithm to the approximations coefficients of the previous level (cA_1) to obtain new coefficients cA_2, cH_2, cV_2, and cD_2 and so on. By doing this, increasingly larger details and smoother versions of the surface can be recovered from the details and approximation coefficients by reconstructing them back to the original level (Zeroth level). Using multi-resolution analysis the decision on how many levels of decomposition are needed in a specific case depends on the resolution of the original data and how much is known about the surface being analyzed. Similar to the 1D-FWT, the approximations and details can be reconstructed back separately to the zeroth level, added arithmetically and/or render separately to provide useful combinations. For example:

$$f(x,y) = A_0 = A_1 + H_1 + V_1 + D_1 \quad \text{...(C-11)}$$

can be interpreted as the original surface decoupled into the wavelet approximation and details reconstructed from the 1st level back to the zeroth level, i.e. :

$$f(x,y) = A_0 = APPROXIMATION_1 + DETAILS_1 \quad \text{...(C-12)}$$

Other combinations of reconstructions may be found useful. For instance, if the 2nd level of the wavelet MRA is found to be more helpful, then Equation (C-11) can be recast into

$$f(x,y) = A_0 = A_2 + H_2 + V_2 + D_2 + H_1 + V_1 + D_1 \quad \text{...(C-13)}$$

Therefore, in general, a useful way of decoupling details could be:

$$f(x,y) = A_0 = A_{opt} + \sum_{j+1=1}^{j+1=opt} \left(H_{(j+1)} + V_{(j+1)} + D_{(j+1)} \right) \quad \text{...(C-14)}$$

Where "*opt*" is the optimal wavelet MRA level for the surface approximation chosen after visual inspection.

APPENDIX D Thermophysical properties for various work materials

Table D-1 Heat Capacities, standard entropy of formation, and standard enthalpy of formation for various work materials (after Kubaschewski, 1993)

Substance	$(S_f)^o$ (J/K.mol)	$(H_f)^o$ (kJ/mol)	T (K)	H_T (kJ/mol)	$C_p = A + BT + CT^{-2} + DT^2$ (J/K.mol)			
					A	$B\times10^3$	$C\times10^{-5}$	$D\times10^6$
Ti	30.7	0.0	298		24.94	6.57	-1.63	1.34
Ti	-	-	1155	4.2	30.48	-8.87	-	6.44
Ti	-	-	1943	16.7	41.84	-	-	-
Fe	27.3	0.0	298	-	28.18	-7.32	-2.90	25.04
Fe	-	-	800	-	-263.45	255.81	619.23	-
Fe	-	-	1000	-	-641	696.34	-	-
Fe	-	-	1042	-	1946.25	-1787.50	-	-
Fe	-	-	1060	-	-561.95	334.13	2912.11	-
Fe	-	-	1184	0.9	23.99	8.36	-	-
Fe	-	-	1665	0.8	24.64	9.90	-	-
W	32.6	0.0	298		23.68	4.06	-0.47	-0.33
Fe_3C	104.6	-25.1	298	-	82.01	83.68	-	-
Fe_3C	-	-	480	0.8	107.32	12.55	-	-
WC	34.7	40.6	298	-	43.39	8.62	-9.33	-1.03
TiC	24.7	184.5	298	-	48.43	3.16	-1.36	1.23

BIBLIOGRAPHY

ABAQUS Inc, (2006), ABAQUS User's Manual, RI.

Akasawa, T. and Hishiguti, H. (1980) 'Crater Wear Mechanism of WC-Co Tools at High Cutting Speeds', Wear, Vol. 65, pp.141-150.

Anamalay, R.V.; Kirk, T.B.; and Panzera, D. (1995). "Numerical descriptors for the analysis of wear surfaces using laser scanning confocal microscopy." Wear (v181-183), pp771-776.

Astakhov, V.P. (2004) 'The assessment of cutting tool wear', International Journal of Machine Tools and Manufacture, Vol. 44, pp.637–647.

Astakhov, V.P. (2006) Tribology of Metal Cutting, Elsevier, San Diego, California, U.S.A.

Attia, M.H. and Kops, L. (2004). "A new approach to cutting temperature prediction considering the thermal constriction phenomenon in multi-layer coated tools." Annals of the CIRP (v53), pp47-52.

Becker, J.-M.; Grousson, S.; and Jourlin, M. (2001). "Surface state analysis by means of confocal microscopy." Laboratoire Image, Signal et Acoustique, Ecole Superieure de Chimie Physique-France, p2.

Bhushan, B. (2002) Introduction to Tribology, New York: John Wiley & Sons.

Boothroyd, G. and Knight, W.A (1989) Fundamentals of Machining and Machine Tools, Second edition, Marcel Dekker Inc., New York.

Bruzzone, A.A.G., J.S. Montanaro, A. Ferrando, P.M. Lonardo, (2004) 'Wavelet Analysis for Surface Characterization: An Experimental Assessment', CIRP Annals , Vol.53, pp479-482.

Burwell, J.T. (1955) 'Survey of possible wear mechanisms', Wear-Usure-Verschleiss, Vol. 1 No. 1, pp.119-141.

Byrd, J.D. and Ferguson, B.L. (1978) 'A study of the influence of hard inclusions on carbide tool wear utilizing a powder metal technique', Proceedings of the VIth NAMRC, pp.310-1315.

Chakraborty, A.; Ray, K.K.; and Bhaduri, S.B. (2000). "Comparative wear behavior of ceramic and carbide tools during high speed machining of steel." Materials and Mfg. Processes Vol.15, pp269-300.

Childs, T.H.C., Maekawa, K., Obikawa, T., and Yamane, Y. (2000) Metal Machining – Theory and applications, Arnold Publishers, London.

Cho, S.-S. and Komvopoulos, K. (1997). "Wear mechanisms of multilayer coated cemented carbide cutting tools." Trans. of ASME, Journal of Tribology (v119), pp8-16.

Cho, S.-S. and Komvopoulos, K. (1998). "Cutting force variation due to wear of multi-layer ceramic coated tools." Trans. of ASME, Journal of Tribology (v120), pp75-81.

Chubb, J.P. and Billingham, J. (1980). "Coated tools – a study of wear mechanisms in high speed machining." Wear (v61), pp283-293.

Chubb, J.P.; Billingham, J.; Hall, D.D.; and Walls, J.M. (1980). "Comparison of wear behaviour of single- and multilayer coated carbide cutting tools." Metals Technology (v7), pp293-299.

Cook, N.H. and Nayak, P.N. (1969) Development of Improved Cutting Tool Materials, Technical report of AFML-TR-69-185, U.S. Air Force Materials Laboratory.

Corle, T. and Kino, G. (1996). Confocal Scanning Optical Microscopy and Related Imaging Systems. San Diego: Academic Press.

Dawson, T.G. and Kurfess, T.R. (2005). "Quantification of tool wear using white light interferometry and three-dimensional computational metrology." Int'l Journal of Machine Tools and Manufacture , Vol. 45, pp591-596.

Dearnley, P.A. and Trent, E.M. (1982). "Wear mechanisms of coated carbide tools." Metals Technology (v9), pp60-75.

Devillez, A., S. Lesko, W. Mozer, (2004) 'Cutting tool crater wear measurement with white light interferometry', Wear Vol.256, pp56–65.

Dixon, G.; Wright, R.; Roger, N.; and Lee, M. (1985). "Processes involved in the wear of cemented carbide tools." Wear (v104), pp157-171.

Ezugwu, E.O.; Olajire, K.A.; and Jawaid, A. (2001). "Wear performance of multilayer coated carbide tools." Machining Science and Technology (v5), pp115-119.

Farhat, Z.N. (2003). "Wear mechanism of CBN cutting tool during high-speed machining of mold steel." Materials Science and Eng. Vol.A361, pp100-110.

Francoso de Avila, A. Mendes Abrao, G. C. Duraes de Godoy, (2006), "The performance of TiN coated carbide tools when turning AISI 8620 steel", Journal of Materials Processing Technology 179, pp. 161–164.

Fu, S., B. Muralikrishnan, J. Raja, Engineering Surface Analysis with Different Wavelet Bases, Transactions of the ASME, 125 (2003) 844852.

Gee, M.G. and McCormick, N.J. (1992). "The application of confocal scanning microscopy to the examination of ceramic wear surfaces."Journal of Physics D: Applied Physics Vol.25, ppA230-A235.

Gekonde, H.O. and Subramanian, S.V. (2002) 'Tribology of tool-chip interface and tool wear mechanisms', Surface and Coatings Technology, Vol. 149, pp.151-160.

Gonzales, R.C., Woods, R.E., Eddins, S.L. (2004) Digital Image processing using MATLAB, Prentice Hall, 782 pages.

Grzesik, W. and Nieslony, P. (2003). "Thermophysical-property-based selection of tool protective coatings for dry machining of steels." Journal of Mfg. Science and Engineering (v125), pp689-695.

Grzesik, W. and P. Nieslony (2004). "Prediction of Friction and Heat Flow in Machining Incorporating Thermophysical Properties of the Coating-Chip Interface," Wear, Vol. 256, pp.108-117.

Grzesik, W.; Zalisz, Z.; and Nieslony, P. (2002). "Friction and wear testing of multilayer coatings on carbide substrates for dry machining applications." Surface and Coatings Technology (v155), pp37-45.

Haglund, A.J., H.A. Kishawy and R.J. Roger (2005). "On Friction Modeling in Orthogonal Machining: an Arbitrary Lagrangian-Eulerian Finite Element Model," Transactions of NAMRC, Vol. 33, pp. 589-596.

Halvarsson, M., V. Langer, S. Vuorinen (1999). "X-ray Powder Diffraction Data for κ-Al_2O_3," Powder Diffraction, Vol. 14, No. 1, pp. 61-63.

Hartung, P.D. (1981) Tool Wear in Titanium Machining, PhD thesis, MIT, Cambridge, Massachusetts.

Hartung, P.D. and Kramer, B.M. (1982) 'Tool Wear in Titanium Machining', Annals of the CIRP, Vol. 31, No.1, pp.75-80.

Holleck, H. (1986). "Material selection for hard coatings." Journal of Vacuum Science Technology (v4), pp2661-2669.

Hua, J. and Shivpuri, R. (2005) 'A Cobalt Diffusion Based Model for Predicting Crater Wear of Carbide Tools in Machining Titanium Alloys', Journal of Engineering Materials and Technology, Vol. 127, No. 1, pp.136-144.

Hubbard, B. B., The world according to wavelets, E.K. Peters, 2nd Edition (1998).

Johnson, G.R. and W.H. Cook (1983). "A Constitutive Model and Data for Metals Subjected to Large Strains, High Strain rates and High Temperatures." Proceedings of 7th International Symposium on Ballistics, The Hague, Netherlands, pp. 12-21.

Jordan, H.-J.; Wegner, M.; and Tiziani, H. (1998). "Highly accurate non-contact characterization of engineering surfaces using confocal microscopy." Measurement Science Technology, Vol.9, pp1142-1151.

Josso, B., D.R. Burton, M. J. Lalor, (2002) Frequency normalized wavelet transform for surface roughness analysis and characterization, Wear Vol.252, 491-500.

Karthik, A., S. Chandra, B. Ramamoorthy, and S. Das, (1997) '3D Tool wear measurement and visualization using stereo imaging', International Journal of Machine Tools and Manufacturing Vol. 37, No. 11, pp1573-1581.

Kim, W. and Kwon P. (2002) 'Phase Transformation and Its Effect on Flank Wear in Machining Steels', ASME Journal of Manufacturing Science and Engineering, Vol. 124, pp.659-666

Kim, W. and Kwon, P. (2001). "Understanding the mechanisms of crater wear." Transactions of NAMRI/SME (v29), pp383-390.

Kim, W.S. (2000) A New Methodology for Predicting Tool Wear, Ph.D. thesis, Michigan State University, East Lansing, Michigan.

Kramer, B.M. (1979) An Analytical Approach to Tool Wear, PhD Dissertation, MIT, Cambridge, USA.

Kramer, B.M. (1987) 'On Tool Materials for High Speed Machining', ASME Transactions – Journal of Engineering for Industry, Vol. 109, No.2, pp.87-91.

Kramer, B.M. (1993) ' Tribological Aspects of Metal Cutting', ASME Journal of Engineering for Industry, Vol. 115, pp.372-376.

Kramer, B.M. and Kwon, P. (1985) 'Computational Design of Coating Materials', Journal of Vacuum Science and Technology, Vol. A3, No.6, pp.2349-2444.

Kramer, B.M. and Suh, N.P. (1980) 'Tool Wear By Solution: A Quantitative Understanding', ASME Transactions – Journal of Engineering for Industry, Vol. 102, No. 4, pp.303-309.

Kubaschewski, O., Alcock, C.B., and Spencer, P.J. (1993) Materials Thermochemistry, 6th edition, Pergamon press, Oxford.

Kubaschewski, O., Evans, E.L., Alcock, C.B. (1967) Metallurgical Thermochemistry, 4th Edition, Pergamon Press, Oxford.

Kwon, P. (2000). "Predictive models for flank wear on coated inserts."Journal of Tribology (v122), pp. 340-347.

Kwon, P. and Kountanya, R. (1999) 'Experimental Observation on Machining Spheroidized Plain Carbon Steels', Tribology Transactions, Vol. 42, No. 2, pp. 265-272.

Larsson, A. (2000). "Microstructure and Wear of CVD Coatings used in Metal Cutting Applications." Doctoral thesis, Chalmers University of Technology, Goterbog, Sweden.

Larsson, A., M. Halvarsson, S. Ruppi (1999). "Microstructural changes in CVD κ-Al_2O_3 Coated Cutting Tools during Turning Operations." Surface and Coatings Technology, Vol. 111, pp. 191-198.

Madhavan, V. and A.H. Adibi-Sedeh (2005). "Understanding of Finite Element Analysis Results under Framework of Oxley's Machining Model," Machining Science and Technology, Vol. 9, pp345-368.

Maksumov, A., R. Vidu, A. Palazoglu, P. Stroeve, (2004) Enhanced feature analysis using wavelets for scanning probe microscopy images of surfaces, J. of Colloid and Interface Science, Vol. 272, pp365-377.

Mallat, S. (1989), "A theory for multiresolution signal decomposition: the wavelet representation," IEEE Pattern Analysis and Machine Intelligence, Vol. 11, no. 7, pp. 674-693.

Mathia, T.; Zahouani, H.; Rousseau, J.; and Le Bosse, J.C. (1995). "Functional significance of different techniques for surface morphology measurements." Int. Journal of Machine Tools and Manufacture Vol.35, pp195-202.

MATLAB 7.0 Help files (2007), Matlab R2007a (Version 7.4.0.287) - The Mathworks, Inc.

Miyoshi, K. (2002). "Surface analysis and tools." NASA/TM -2002-211815. Cleveland: Glenn Research Center.

Mohan, V.S. and A.K. Balaji (2002). "On Modeling the Tool-Chip Contact in Machining of Plain Carbon Steels with Multi-layer Coated Cutting Tools." Proc. 5th CIRP International Workshop on Modeling of Machining Operations, West Lafayette, IN, USA, May 20-21, pp. 109-121.

Molinari, A. and Nouari, M. (2002) 'Modeling of tool wear by diffusion in metal cutting', Wear, Vol. 252, pp.135-149.

Naerheim, Y. and Trent, E.M. (1977) 'Diffusion Wear of Cemented Carbides Tools when Cutting Steel at High Speeds', Metals Technology, Vol. 4, pp.548-556.

Opitz, H. (1963) 'Tool Wear and Tool Life', International Production Engineering Research Conference – Proceedings, Pittsburgh, Pennsylvania, 9-12 September, pp.107-113.

Ozel, T. and E. Zeren (2005). "Finite Element Modelling of Stresses Induced By High Speed Machining of With Round Edge Cutting Tools," Proceedings of IMECE'05, Orlando, Florida, pp.1-9

Paldey, S. and Deevi, S.C. (2003) "Single layer and multilayer wear resistant coatings of (Ti,Al)N: a review." Materials Science and Eng. Vol.A342, pp58-79.

Rabinowicz, E. (1977) 'Abrasive Wear Resistance as a Materials Test', Lubrication Engineering, Vol. 33, pp.378-381.

Rabinowicz, E. (1995) Friction and Wear of Materials, Second edition, John Wiley & Sons, Inc., New York.

Rabinowicz, E., Dunn, L.A., Russell, P.G. (1961) 'A Study of Abrasive Wear under Three-Body Conditions', Wear, Vol. 4, pp. 345-355.

Ramalingam, S. and Wright, P.K. (1981) 'Abrasive Wear in Machining: Experiments With Materials of Controlled Microstructure', ASME Transactions - Journal of Engineering Materials and Technology, Vol. 103, No.2, pp.151-156.

Ruppi, S. (2005). "Deposition, microstructure and properties of texture controlled CVD α -Al_2O_3 coatings," International Journal of Refractory Metals & Hard Materials, Vol. 23, pp. 306-316.

Seah, K.W.H.; Rahman, M.; and Lee, C.H. (1995). "Comparing the effectiveness of coatings on carbide and cermet cutting tools inserts."Journal of Materials Science Technology (v11), pp269-275.

Semler, E.J.; Tija, J.S.; and Moghe, P.V. (1997). "Analysis of surface microtopography of biodegradable polymer matrices using confocal reflection microscopy." Biotechnology Progress Vol.13, pp630-634.

Shaw, M. (2005) Metal Cutting Principles, Second edition, Oxford University Press Inc., New York.

Sheppard, C.J.R. and Shotton, D.M. (1997). Confocal Laser Scanning Microscopy. BIOS Scientific Publishers.

Soderlund, E., I. Reineck, D.J. Rowcliffe (1994). "Ultralow load indentation hardness and modulus of κ- and α -Al_2O_3 coatings," Journal of Materials Research, Vol. 9, No. 7, pp. 1683-1692.

Srinivasan, K.; Venkatesh,V.C.; and Raju, A.S. (1977). "Wear mechanisms in coated carbide tools." Tribology Int'l (v10), pp313-318.

Stephenson, D. A. and Agapiou, J.S. (2006) Metal Cutting Theory and Practice, Second edition, CRC Press- Taylor & Francis group, Boca Raton.

Stuber, M., Leiste, H., Ulrich, S. and Skokan, A, (1999), "Development of Tailored Coating Concepts for CVD and PVD Deposition of Multifunctional Coatings – A Review," Z. Metallkd., Vol. 90, pp. 774-779.

Su, Y.-F., M.A. Torzilli, J.D. Meyer, C.J. Rawn, M.J. Lance, S. Ruppi, W. Y. Lee (2002). "Effects of an Electroplated Platinum Interlayer on the Morphology and Phases of Chemically-Vapor-Deposited Alumina on Single-Crystal, Nickel-Based Superalloy." Journal of the American Society of Ceramics, Vol. 85, No. 8 pp. 2089-2096.

Takeyama, H. and Murata, R. (1963) 'Basic Investigation of Tool Wear', ASME Transactions - Journal of Engineering for Industry, Vol.85, No.1, pp.33-38.

Trent, E.M. (1963). "Cutting steel and iron with cemented carbide tools-Parts 1, 2, and 3." Journal of the Iron and Steel Institute (v201), pp847-855, 923-932, 1001-1015.

Udupa, G.; Singaperumal, M.; Sirohi, R.S.; and Kothiyal, M.P. (2000). "Characterization of surface topography by confocal microscopy I and II." Measurement Science Technology (v11), pp305-329.

Vleugels, J. and Van Der Biest (1999) 'Chemical wear mechanisms of innovative ceramic cutting tools in the machining of steel', Wear, Vol.225-229, pp.285-294.

Vuorinen, S., L. Karlsson (1992). "Phase transformation in chemically vapour-deposited κ- alumina." Thin Solid Films, Vol. 214, pp. 132-143.

Wang, W.H., Y.S. Wong, G.S. Hong, (2006) '3D measurement of crater wear by phase shifting method', Wear Vol. 261, pp164–171

Whitehouse, D.J. (1997). "Surface metrology - review article." Measurement Science Technology (v8), pp955-972.

Wilhelm, S.; Grobler, B.; Gluch, M.; and Heinz, H. (2003). Confocal Laser Scanning Microscopy – Principles. Carl Zeiss Advanced Imaging Microscopy.

Wong, T. and Kwon, P. (2006) 'Dissolution profile of tool material into chip lattice', ASME Journal of Manufacturing Science and Engineering, Vol.128, pp.928-937.

Wong, T., Kim, W., and Kwon, P. (2004) 'Experimental support for a model-based prediction of tool wear', Wear, Vol. 257, pp.790-798.

Wright, P.K. and Bagchi, A. (1981) 'Wear Mechanisms that Dominate Tool-Life in Machining' Journal of Applied Metal Working, Vol. 1, No. 4, pp.15-23.

Yen, Y.-C., A. Jain, P. Chigurupati, W.-T. Wu and T. Altan (2004). "Computer Simulation of Orthogonal Cutting Using a Tool with Multiple Coatings," Machining Science and Technology, Vol. 8, pp. 305-326.

Yoon, M. C., D. H. Chin, (2005) Cutting force monitoring in the endmilling operation for chatter detection, Journal of Eng. Manuf., Vol. 12, pp455-466.

Yuan, C., Z. Peng, X. Yan, (2005) Surface Characterization Using Wavelet Theory and Confocal Laser Scanning Microscopy, Journal of Tribology - Trans. of the ASME, 127 394-404.

Zeng, W., X. Jiang and P. Scott, (2005) Metrological characteristics of dual-tree complex wavelet transform for surface analysis, Measurement Science and Technology, Vol.16, pp1410-1417